NONLINEAR OPTICAL STUDIES OF GYPSUM DISSOLUTION MECHANISMS, SURFACTANT ADSORPTION ON GYPSUM SURFACE AND ANALYSIS OF ENVIRONMENTALLY RELATED IONS

by

Galip Yiyen

A dissertation submitted in partial fulfillment
of the requirements for the degree

of

Doctor of Philosophy

in

Chemistry

MONTANA STATE UNIVERSITY
Bozeman, Montana

July 2023

DEDICATION

To my sister, mother and father…

ACKNOWLEDGEMENTS

First of all, I would like to thank Dr. Rob Walker. There are countless moments that have made me feel lucky for working with Dr. Rob Walker in the past 5 years. I would like to thank him for trying to approach every challenge with a positive attitude and also for the constructive feedback that he -always!- provided in our meetings and conversations.

I would like to thank my committee members Dr. Erik Grumstrup, Dr. Nick Stadie, Dr. Mike Mock and Dr. Stephanie Ewing for their feedback and support!

I would like to thank Walker Research Group members; especially Dr. Katie Link for teaching me how to use SFG setup; Kodie Duck for putting hard work on collecting enormous amount of wet lab data and presenting them and Dr. Liddi Meredith for making the groundwater accessible for this project and her input in our conversations.

I would like to thank Dr. Doreen Brown for always being there and doing her best to help me whenever I need and making this journey definitely a better experience!

TABLE OF CONTENTS

TABLE OF CONTENTS CONTINUED

TABLE OF CONTENTS CONTINUED

LIST OF TABLES

Table Page

LIST OF FIGURES

Figure Page

LIST OF FIGURES CONTINUED

Figure Page

ABSTRACT

Southeastern Montana hosts one of the largest open-air coal mine sites in the world. Federal regulations after finalization of the open-air coal mining activities require reclamation, which creates buried spoils that may serve as aquifers at former mining sites. Once hosting an inland sea, the region's saline sedimentary rocks and soils contribute to the groundwater salinity, though at lower levels prior to mining. However, the creation of spoils through mining pulverizes soils, sediment, and rocks formerly overlying coal deposits, mixing them and increasing their surface area. In infiltrating waters from snow melt and heavy rain, minerals dissolve more readily due to this enhanced surface area in spoils, increasing the salinity in groundwater.

A primary water quality concern in regional groundwater is high sulfate concentrations. Sulfate in water originates from weathering and dissolution of soluble secondary salts, such as calcium sulfate (dihydrate, hemihydrate and anhydrite), sodium sulfate and magnesium sulfate. Gypsum ($CaSO_4 \cdot 2H_2O$) is thought to be a primary source of dissolved sulfate in the ground and surface waters in Southeastern Montana and 'gypsum dissolution' is at the focus of this dissertation.

Vibrational sum frequency generation spectroscopy was used to understand the molecular level interactions at the gypsum surface upon interaction with bulk water. Additionally, surfactant adsorption on gypsum surface and its impacts of gypsum dissolution were investigated. Besides optical spectroscopy studies, an efficient and quick water analysis technique was adapted to determine the sulfate concentrations in environmental samples.

Two different types of orientations of structural water molecules at the gypsum surface were observed. Results also showed that these water molecules are tightly bound to the surface. Surfactant adsorption was found to be only limited to the surfactants with sulfate headgroups and resulted in suppressed gypsum dissolution. A titration technique is found to be effective and accurate for sulfate analysis of environmental water samples.

CHAPTER ONE

INTRODUCTION

Motivation

Access to safe drinking water is a problem that impacts millions of lives around the world[1, 2]. According to UNICEF reports, contaminated water and poor sanitation are among the leading causes of child mortality[3]. Contaminants in drinking water range from microbes introduced by poor sanitation practices to organic species introduced by agriculture and industry to both naturally and anthropogenic inorganic ions. Recent studies show a strong relationship between groundwater salinity and neonatal deaths in the regions where groundwater is used directly for drinking water[4].

High salinity in soil and water has adverse effects on living organisms, and high salinity in soil contributes to the water salinity, increasing the water's osmotic potential. Due to its higher osmotic potential, soil water draws water from microorganisms, causing cell death, as well as from roots[5, 6]. This negative impact on overall ecosystem health was investigated by Welles et al. who examined the impact of salinity changes on enhanced biological phosphorus removal (EBPR) process[7]. Two competing microorganisms in the EBPR process, phosphate-accumulating organisms (PAO) and glycogen-accumulating organisms (GAO) using carbon sources such as acetate, to remove phosphorus, were subjected to high salinity (6% W/V as NaCl) and their sensitivities were investigated. Results show that acetate uptake rate of PAO decreased by 71%, while it decreased by 41% for GAO in high salinity solutions, indicating reduced efficiency of phosphorus removal in saline water.

Ground water salinity can come from many sources, and the main constituents of ground water salinity include many common cations and anions such as Na^+, K^+, Ca^{2+}, Mg^{2+}, Cl^-, NO_3^-, CO_3^{2-} and others[8, 9]. Depending on their concentrations, these ions have different impacts on living organisms[10, 11]. Nitrate contamination raises concerns due the recent studies linking high nitrate concentrations (>10 ppm) in drinking water and its possible adverse health effects, such as methemoglobinemia. Ingested nitrate is reduced to nitrite in the body. As nitrite binds to hemoglobin to produce methemoglobin, oxygen carrying capacity in blood is reduced due to lower amounts of hemoglobin. The end result is methemoglobinemia, a sometimes-fatal condition in infants[12]. Finally, high concentrations of sodium, chloride and bicarbonate are toxic to many plants[13], and there is a strong –and infamous – correlation between sodium chloride uptake and hypertension[10].

In the Intermountain West, high salinity in ground and surface water is a significant ecosystem and community health concern. Communities in the region mostly rely on well water for drinking water, along with septic systems, rather than treated public water systems. Due to the specific geology of the region, once part of an inland sea, and the region's aridity[14], soils commonly contain soluble minerals such as gypsum and calcite[15, 16]. Snow runoff and intense rain events dissolve these minerals – gypsum especially – leading to total dissolved salt (TDS) concentrations in the range of ~1100 to ~5000 mg/L, as high as 5200 mg/L in the region[17]. These numbers are notable given that EPA has set a secondary standard of 500 mg/L (TDS) for drinking water[18].

At its most fundamental level, ground water salinity arises from minerals dissolving into water and precipitating as regulated by thermodynamics. Dissolution is nothing more than

chemistry occurring at a solid/liquid interface. Mineral dissolution is mostly studied by measuring dissolution rates under different conditions. In one study, dissolution rates of three carbonate minerals, calcite ($CaCO_3$), dolomite ($CaMg(CO_3)_2$) and magnesite ($MgCO_3$), were investigated in solutions with different pH, CO_2 partial pressures and different NaCl concentrations[19]. Dissolution rates of all these minerals were found to increase with decreasing pH, while the CO_2 partial pressure did not have significant impact when corrected for pH change. Change in NaCl concentrations also did not yield meaningful change in the dissolution rates of these minerals. On the other hand, gypsum's dissolution rate was increased significantly in environments containing NaCl[20]. The thermodynamic limit for gypsum dissolution is reported as 2.0 g/L in pure water[20], though, in the environment gypsum is under the continuous interaction with saline and flowing water. Research described in this dissertation examines chemistry occurring at the gypsum-water interface with a focus on water structure and adsorbed surfactant behavior.

Gypsum ($CaSO_4 \cdot 2H_2O$) is an important mineral in the geology of the Powder River Basin (PRB) and one of the minerals governing the groundwater salinity in the northern PRB region. Water analysis prior to the mining years show moderate concentrations of sulfate. Average SO_4^{2-} concentrations found in the shallow wells (depths less than 200 ft) and deep wells (depths greater than 200 ft) were reported as 1100 mg/L and 390 mg/L, respectively[21]. The PRB is a structural basin that straddles Montana and Wyoming and is home to the largest coal reserves in the US (Figure 1.1). In fact, the PRB contains approximately 6% of the world's coal supply. Coal from the Powder River Basin accounted for approximately 40% to the total amount mined in the US between 2010 and 2018; and 28% of the mined coal is used to produce electricity domestically in

2018[22]. Apart from questions about the environmental drawbacks of using coal as a source for power production, coal mining itself dramatically impacts local ecology and results in large-scale, long-lasting landscape disruption and compromised water quality[23].

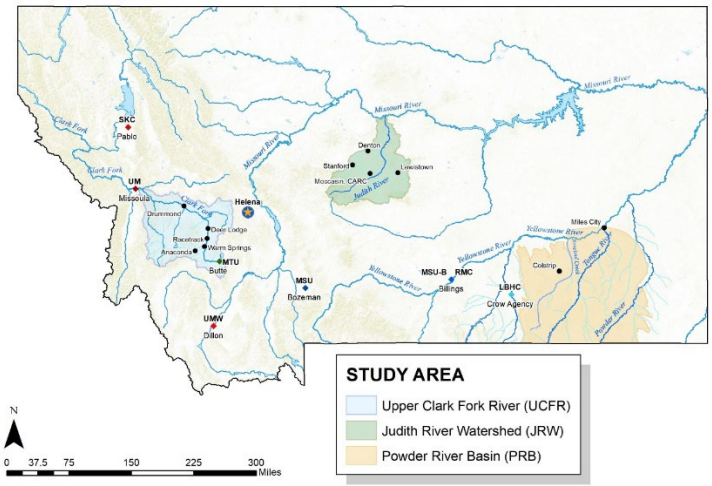

Figure 1.1. Map of Montana with the main water bodies highlighted.

One consequence of open-air coal mining is degradation of ground and surface water quality. Open-air coal mining typically requires that the first 10-30 meters of earth be removed in order to expose the underlying coal. The removed material is called overburden and after it is removed, this same material is called spoils. After the coal has been mined, the spoils are used to refill the mining excavation as part of the reclamation process. Unlike the overburden, however, the spoils now are comprised of material having much greater exposed surface area and are more susceptible to processes occurring at the material surface. One of those processes is dissolution. The relatively high gypsum content in the spoils can lead to high levels of sulfate in groundwater coming from land reclaimed from open coal mining activities[24-27].

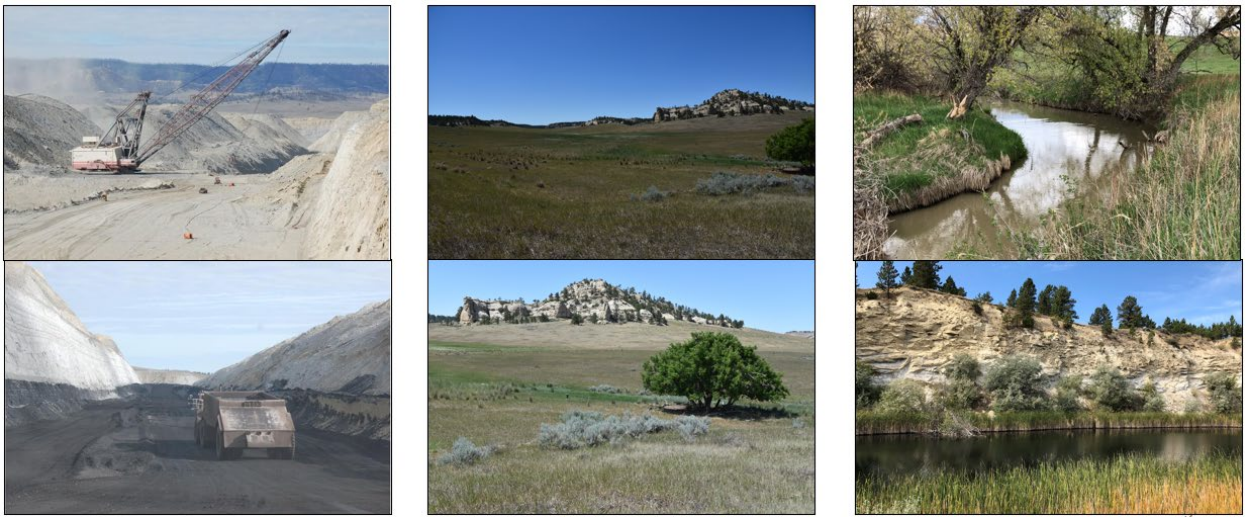

Figure 1.2. Pictures from an open-air coal mine in Colstrip, MT (left); reclaimed area of the Big Sky Mine (middle); upper Rosebud Creek near Colstrip (top right); and a residual pond formed at the headwall of a reclaimed mining area (bottom right), providing a cross sectional view of overburden materials at this location (pictures courtesy of Prof. Rob Walker).

Sulfate levels for human consumption above 500 mg/L (or 500 ppm) can cause laxative effects in people[28]. Additionally, sulfate concentrations exceeding 2000 mg/L are discouraged for livestock, as levels of 2500 to 3000 mg/L in stock water cause health effects such as infertility, weight loss and neurological disorders in animals[28]. High sulfate concentrations also resulted in adverse effects on aquatic life[29]. In brackish and freshwater systems, sulfate reduction by microorganisms results in accumulation of sulfide, which is a strong phytotoxin, affecting plant fitness and ecosystem function[29]. According to analysis of samples from different regions of the PRB measured between October 2016 and May 2022, sulfate concentrations were reported as 450 mg/L on the low end and as high as 3000 and 5000 mg/L in the reclaimed areas[17].

While the consequences of excessive gypsum dissolution for human and ecosystem health are clear, the molecular mechanisms responsible for dissolution are not. In a review by Klimchouk, varying gypsum solubilities in different salt solutions are presented[20]. Even though the solubilities significantly increase in salt solutions, ($Mg(NO_3)_2$), $MgCl_2$, NH_4Cl, $NaNO_3$ and

NaCl), compared to pure water, trends presenting the solubility changes do not provide any molecular level understanding of the impacts of these salts on gypsum dissolution. The impacts of pressure and temperature on gypsum dissolution rates were studied by Hong et al.[30]. The study reported higher gypsum dissolution ratios in sea water than in pure water at 100 degree C and 27 MPa. However, at 30 degree C and 0.3 MPa, the dissolution rate in pure water was significantly higher than in sea water. Hong et al. also reported that gypsum's dissolution rate in pure water diminished almost linearly from 30 degree C and 0.3 MPa to 150 degree C and 43 MPa[30]. In another study, Knittle et al. reported significant changes in the vibrational spectra (IR and Raman) of gypsum with changing pressure. Frequency shifts for the major peaks (sulfate and water stretching signals) become noticeable around 5000 MPa[31]. Even though the applied pressures on gypsum in Hong's and Knittle's studies are not easily comparable, differences observed between the two studies imply that the gypsum dissolution is strongly affected by molecular level interactions. Therefore, research described in this dissertation is premised on the assumption that changes in gypsum surface chemistry will affect gypsum dissolution. Specifically, studies in this dissertation were motivated by three general hypotheses:

H1. Organic surfactants will adsorb to gypsum surfaces and organize in a way that reflects surfactant headgroup interactions with the substrate. Testing this hypothesis has direct consequences for gypsum surface chemistry in the presence of organic acids and other biomolecules in environmental settings.

H2. Organic surfactant adsorption will change gypsum dissolution properties. While this hypothesis may seem self-evident, results from these studies will impact how environmental scientists model the origin and transport of groundwater salinity.

H3. Gypsum's structural water molecules at the gypsum surface are much more strongly coupled to gypsum than to an adjacent aqueous phase. This hypothesis, if true, means that the water molecules intrinsic to gypsum *are not* likely to participate in gypsum's surface chemistry and that dissolution will hinge upon aqueous phase water interactions with the surface calcium and sulfate ions.

In the process of conducting this research we developed a simple method for measuring dissolved sulfate concentrations in samples collected from ground and surface water field sites and showed this method – conductometric titration – could be generalized to detect other ions of interest such as chloride. Studies described in Chapters 2-5 employ a suite of different measurement techniques that measure the vibrational structure of molecules on the gypsum surface and the surface's elemental composition. These surface techniques are complemented by more traditional spectroscopic analytical methods such as FTIR absorbance and vibrational Raman scattering. The following sections describe these techniques, summarizing their operating principles and the types of data that are measured. This chapter concludes with brief summaries of the subsequent chapters where findings from these studies are discussed in detail.

Experimental Methods

Vibrational Sum Frequency Generation

The VSFG setup used in this study employs an ultrafast amplifier producing 800 nm beam (Coherent Libra HE). Output from the Libra is split into two beams by using an 80/20 beam splitter. 80% of the intensity is directed towards a Coherent OPerA Solo and the IR frequency light it produces comes from difference frequency generation (DFG) in a BBO crystal. The remaining output from the Libra (20%) is directed towards a home built 4f pulse shaper. In

the pulse shaper, the 800 nm pulse is first reflected from a 1400 g/mm grating and the separated spectral components are passed through a cylindrical lens. Then, the spatially stretched beam passes through a slit that spectrally narrows the pulse. The 'chopped' pulse is retroreflected back through the slit, lens and off of the grating. The diffraction grating combines all of the components back into a single gaussian beam. The output beam from the pulse shaper is spectrally narrower (15-25 cm^{-1} for the shaped beam vs. ~125 cm^{-1} for the original beam), but temporally longer (~2 ps for the shaped beam vs. 100 fs for the original beam).

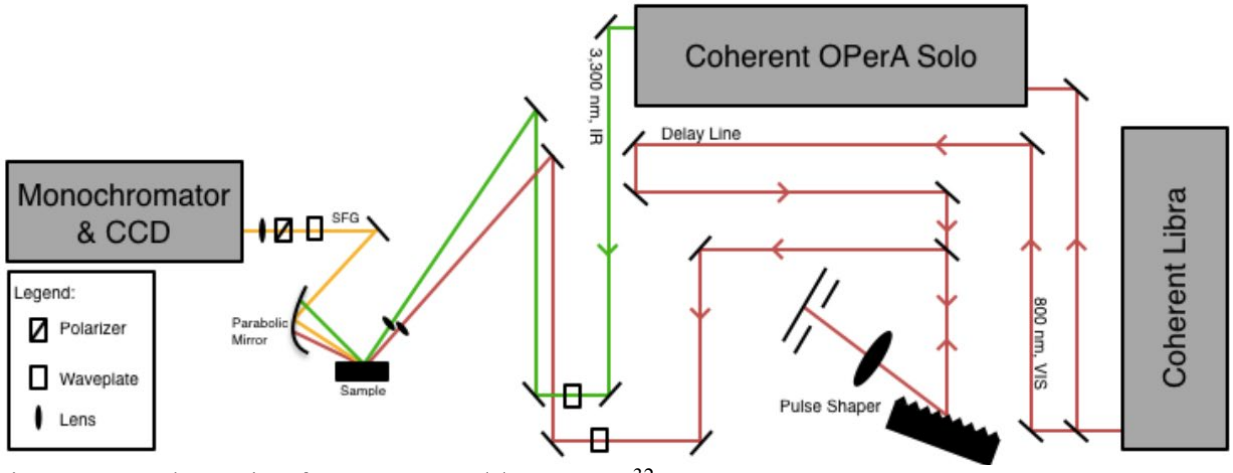

Figure 1.3. Schematic of VSFG assembly at MSU[32]

Before the visible and IR pulses are overlapped on the sample, their polarizations are controlled with λ/2 waveplates. After the polarizations are selected, the spectrally narrow visible and spectrally broad IR beams are temporally and spatially overlapped on the sample surface to produce VSF response. The polarization of the produced VSF beam is then selected with the help of a polarizer and a λ/2 waveplate. A monochromator (Andor Technology, Shamrock 750 mm, 1200 lines/mm grating) and a CCD (Andor Technology, Newton 971P) are used to monitor the VSF beams. Typical spectral resolution from this experimental assembly is 15 to 25 cm^{-1}

FWHM, and resolution depends most sensitively on the slit width in the 4f pulse shaper system. Additionally, temporal overlap impacts resolution. Specific to the gypsum studies, the highest quality VSF spectra require that an unperturbed wavefront (gaussian-looking beam cross section) be carefully directed into the monochromator.

VSFG Theory

To consider the origin of any nonlinear optical signal, one should recognize that as light travels through a medium, it induces an electric dipole (μ) by polarizing the valence electrons on a molecule. The strength of this electric dipole is proportional to the strength of the electric field of the light beam (E), the static dipole of the valence electrons on the molecule (μ_o) and the polarizability of these electrons (α):

$$\mu = \mu_o + \alpha E \qquad \text{Eq 1.1}$$

The induced polarization induced by the oscillating electric field (E) in a condensed phase is described as:

$$P = \varepsilon_o \chi^{(1)} E \qquad \text{Eq. 1.2}$$

where ε_o is the vacuum permittivity, $\chi^{(1)}$ is the average of α and also known as the linear first order electric susceptibility. Equation 1.2 assumes that the light-matter interactions are occurring in the linear response regime.

If the strength of the oscillating electric field is sufficiently strong, additional terms in the original polarizability equation also become significant:

$$\mu = \mu_o + \alpha E + \beta E^2 + \gamma E^3 + \ldots \qquad \text{Eq. 1.3}$$

$$P = \varepsilon_o \chi^{(1)} E + \varepsilon_o \chi^{(2)} E^2 + \varepsilon_o \chi^{(3)} E^3 + \ldots \qquad \text{Eq. 1.4}$$

$$P = P^{(1)} + P^{(2)} + P^{(3)} + \ldots \qquad \text{Eq. 1.5}$$

where β and γ are second and third order molecular hyperpolarizabilities: $P^{(2)}$ and $P^{(3)}$ are second and third order non-linear polarizabilities; $\chi^{(2)}$ and $\chi^{(3)}$ are second and third order non-linear electrical susceptibilities, respectively. An important point to note is that while α , β, and γ are molecular properties, the $\chi^{(1)}$, $\chi^{(2)}$, and $\chi^{(3)}$ tensors describe the *macroscopic* properties of the system being studied. $P^{(2)}$ gives rise to second harmonic generation (SHG) and sum frequency (SFG) responses from the material. $\chi^{(2)}$ is a third rank susceptibility tensor and all of its 27 elements completely characterize the second order nonlinear susceptibility of a material. Each element of the $\chi^{(2)}$ in a centrosymmetric medium in the opposite directions must be the same:

$$\chi^{(2)}_{ijk} = \chi^{(2)}_{-i-j-k} \qquad \text{Eq. 1.6}$$

However, because $\chi^{(2)}$ is a third rank tensor, each element must be antisymmetric with respect to inversion:

$$\chi^{(2)}_{ijk} = -\chi^{(2)}_{-i-j-k} \qquad \text{Eq 1.7}$$

Equations 1.6 and 1.7 can only be satisfied if every element in the $\chi^{(2)}$ tensor is zero. Therefore, $P^{(2)}$ in the centrosymmetric media, thus SFG response, must be zero. This symmetry is broken at the interfaces. On the planar surface $x \equiv -x$, $y \equiv -y$ but $z \neq -z$. While the properties along the x and y are indistinguishable on the surface, they change along z axis.

Describing an incident electric field as a sinusoidally varying function, the second order polarizability can be described as:

$$E = E_1\cos(\omega t) \qquad \text{Eq. 1.8}$$

$$P^{(2)} = \varepsilon_o\chi^{(2)}(E_1\cos(\omega t))^2 \qquad \text{Eq. 1.9}$$

In the limit that two incident fields are present (in the visible and IR regions of the spectrum) the surface electric field can be represented as the sum of two incident oscillating electric fields:

$$E = E_1\cos(\omega_{vis}t) + E_2\cos(\omega_{IR}t) \quad \text{Eq. 1.10}$$

Rearranging $P^{(2)}$ considering the sum of the two electric fields, instead of one applied electric field:

$$P^{(2)} = \varepsilon_o\chi^{(2)}(E_1\cos(\omega_{vis}t) + E_2\cos(\omega_{IR}t))^2 \quad \text{Eq. 1.11}$$

$$P^{(2)} = \varepsilon_o\chi^{(2)}[(E_1^2+ E_2^2) + (E_1^2\cos2\omega_{vis}t) + (E_2^2\cos2\omega_{IR}t) + (\tfrac{1}{2}E_1E_2\cos(\omega_{vis}-\omega_{IR})t) + (\tfrac{1}{2}E_1E_2\cos(\omega_{vis}+\omega_{IR})t)] \quad \text{Eq. 1.12}$$

In Equation (1.12), the first term in the square brackets describes the DC field generated by two incident beams; the second and third terms describe the SHG for both visible and IR beams; the fourth term describes the difference frequency generation (DFG) and the last term describes SFG.

In addition to giving SFG its surface specificity, the $\chi^{(2)}$ tensor is also sensitive to the vibrations of specific functional groups. Each element of the $\chi^{(2)}$ tensor can be separated into resonant and non-resonant contributions:

$$\chi^{(2)} = \chi^{(2)}_{NR} + \chi^{(2)}_{R} \quad \text{Eq. 1.13}$$

The non-resonant term in Equation 1.13 is typically quite small, but when ω_{IR} approaches the frequency of an allowed vibrational transition, the resonant contribution can get quite large. The resonant term of the $\chi^{(2)}$ tensor is equal to the product of a vibration's Raman and IR transition moments, $A_{R,q}$:

$$\chi^{(2)}_{R} = \sum_q \frac{A_{R,q}}{(\omega_{IR}-\omega_{x,q}+i\Gamma_q)} \quad \text{Eq. 1.14}$$

where ω_{IR}, $\omega_{x,q}$ and Γ_q are the frequency of incoming IR beam, the molecular vibrational frequency and homogenous half-width of the mode, respectively. From Eq. 1.14, one readily sees that as ω_{IR} approaches a vibrational $\omega_{x,q,}$ the denominator of Eq. 1.14 gets small and the $\chi^{(2)}{}_R$ response is enhanced.

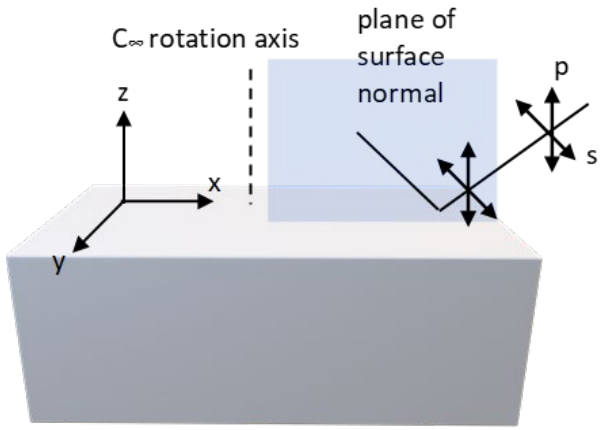

Figure 1.4. Representation of a sample surface, plane of the surface normal and interaction of light beams at different polarizations with the surface[33]

One last aspect of SFG spectroscopy deserves mention. An SFG experiment involves three fields, ω_{sum}, ω_{vis}, and ω_{IR}. As noted at the start of this section, l/2λ optics are used to control the polarizations of the two incident fields and the generated field at ω_{sum}. Choosing different polarizations selects different elements of the $\chi^{(2)}$ tensor. As mentioned in the explanation of equations 1.6 and 1.7, properties of an isotropic surface along the x and y are indistinguishable. Thus, change in the sign of x and y would not change the sign of $\chi^{(2)}{}_{ijk}$. Taken the two equations (1.6 and 1.7) into account, the majority of the 27 elements of $\chi^{(2)}$ become zero. The only non-zero elements are $\chi^{(2)}{}_{zii,}$ $\chi^{(2)}{}_{izi}$, $\chi^{(2)}{}_{iiz}$, $\chi^{(2)}{}_{zzz}$, where i = x or y. In an SFG system, these components of $\chi^{(2)}$ can be sampled with different polarization combinations: PSS, SPS, SSP and PPP, where the first letter always represents the polarization of sampled VSF beam, the second letter

represents the polarization of incoming visible beam and the third letter represents the polarization of incoming IR beam.

Vibrational motions in molecules (or groups in molecules, such as -CH_x and -OH) may create changes in the functional group's dipole moment and/or polarizability allowing them to be detected with direct IR absorption and Raman scattering, respectively. Given that the polarization of ω_{IR} samples the direction of the IR transition moment, $P_{sum}S_{vis}S_{IR}$ and $S_{sum}P_{vis}S_{IR}$ polarization combinations create and sample the vibrations in the surface plane, $S_{sum}S_{vis}P_{IR}$ samples the vibrations directed primarily along the surface normal. The $P_{sum}P_{vis}P_{IR}$ polarization combination contains contributions from all of the nonzero $\chi^{(2)}$ elements. Therefore, sampling and comparing the intensities of components of vibrations enables the relative orientations of surface molecules to be determined.

Measurement and Data Process (CH_x region)

For studies of surfactant adsorption and orientation to gypsum surfaces, the OPA is set to produce IR light centered at 2900 cm^{-1}. The IR and visible beams are temporally and spatially overlapped on the sample. Spectral acquisition time is set depending on the signal intensity and typically ranges from 1 minute to 10 minutes. All experiments begin with an initial SFG spectrum collected from a gold surface using a PPP polarization condition to normalize the intensities of molecular signals. While gold does not have any vibrational resonances, its non-resonant $\chi^{(2)}$ response is very large and makes for a good diagnostic for aligning system optics. After measuring the spectrum from Au, a second SFG spectrum is collected under SSP conditions from the surface of liquid DMSO. The two methyl groups of DMSO also create a strong SFG response (although not as strong as Au). The reason for acquiring the SFG spectrum

from the DMSO/vapor interface is that the 2918 cm^{-1} feature in the SFG spectrum can be used to calibrate the vibrational energies in the systems of interest[34].

Measurement and Data Process (OH region)

The IR beam produced by the OPA used in these studies is not capable of covering a range that spans 3000 cm^{-1} to 3600 cm^{-1} in a single experiment. Therefore, spectra examining water in the -OH stretching range were collected stepwise. Spectra covering the range from 3000 cm^{-1} to 3600 cm^{-1} were collected in three steps by centering the produced IR beam frequency to 3050 cm^{-1}, 3190 cm^{-1} and 3350 cm^{-1}. Then, the collected spectra were linearly summed and analyzed against summed background spectra and normalized with summed gold spectra in order to have a single composite spectrum covering the entire -OH region of interest.

Transmission IR Spectroscopy Studies

A commercially available FTIR (Bruker VERTEX 70) is used to get molecular information from the gypsum samples in different forms, as well as for analysis of precipitate collected from SDS solutions containing gypsum pieces. Measurement details for specific analyses are included in the Introduction sections of Chapter 2 and Chapter 4.

Raman Studies

A Raman microscope (HORIBA LabRAM HR Evolution) is used to measure vibrational spectra of water molecules in powder and crystalline forms of gypsum. Raman measurements were able to provide well resolved symmetric and antisymmetric stretching signals from water molecules, that were useful for interpretation of VSFG spectra collected from gypsum surface.

Elemental Surface Analysis

Distributions of elements brought by surfactant adsorption on gypsum surface was investigated by energy-dispersive X-ray (EDX) imaging (Physical Electronics PHI 710). EDX imaging can map the elemental distribution by characterizing the surfaces with ~1 micron depth sensitivity. Therefore, even though it can be used as a complementary technique to characterize the materials, its surface sensitivity does not allow one to characterize the surface at the level of molecular layers. Experimental details are given in the Introduction section of Chapter 2.

Thesis Outline

The overall theme of this research is investigating molecular interaction mechanisms at the gypsum surface and determining how changes in gypsum surface composition affect gypsum dissolution. Included in this work is the development of new, efficient ways to measure the amount of sulfate in water. Content in Chapters 2-5 have either appeared in published or submitted manuscripts *or* is being included in manuscripts in preparation. Consequently, some content in the introductory sections of each chapter will be redundant.

Chapter 2. Surfactant Adsorption to Gypsum Surfaces and The Effects on Solubility in Aqueous Solutions

Chapter 2 describes the investigations addressing two questions: (1) Do certain type of surfactants adsorb on gypsum surface? and (2) Does the possible adsorption affect gypsum dissolution? To address this question, we used VSFG, EDX and conductometric titration methods. Sodium dodecyl sulfate (SDS) and dodecyltrimethylammonium chloride (DTAC) are chosen as surfactants, since they are widely studied as anionic and cationic surfactants, especially in VSFG studies. While VSFG and EDX techniques were used to investigate the

molecule adsorption, conductometric titration was used to determine the amount of gypsum dissolved when the pieces stayed in SDS and DTAC solutions. VSFG spectra showed that SDS molecules adsorb and form a film layer on gypsum surface, while DTAC only agglomerates on the rough patches of the surface and the molecules do not show net polar ordering. Amount of sulfate dissolved from gypsum pieces in SDS solutions were significantly (~40%) less than the amounts found in DTAC solutions and Millipore water. Taken these results together, it is reported that surfactant adsorption diminishes the gypsum/water interaction at the surface and suppresses gypsum dissolution. This work was published in Langmuir[35].

Chapter 3. Accurately Determining Groundwater Sulfate Concentrations from Reclaimed Landscapes with Conductometric Titrations

Chapter 3 discusses the adaptation of a water analysis technique to environmental water samples and presents the accuracy of the results benchmarking against the conventional, EPA approved methods. Water samples were collected from different spots in southeastern and western Montana and they were titrated with different concentrations of $BaCl_2$ solutions to determine the SO_4^{2-} concentrations. Another set of analysis were conducted in Montana Bureau of Mines and Geology (MBMG) using an EPA approved sulfate analysis method (Method 300.0). Results agreed to within ±3.6%. The versatility of this technique is tested with chloride analysis in environmental water samples and the titration results were benchmarked against ion chromatography data reported from Environmental Analytical Lab of Montana State University (EAL-MSU). Results agreed to within ±6.4%. Lastly, linear regression analysis between sulfate concentrations and conductivities showed significant correlation (average $r^2 = 0.93$), and for the water samples in which sulfate is the dominating ion, conductivity is shown to have a potential to

successfully estimate the sulfate concentrations. This work has been submitted to *Environmental Science and Technology - Water* and is currently under review.

Chapter 4. Nonlinear Optical Studies of Water at Gypsum-Air and Gypsum-Aqueous Interfaces

Chapter 4 investigates the water structure at the molecular level on gypsum surface. VSFG spectra collected from gypsum/air and gypsum/water interfaces provided unique information regarding the orientations of water molecules. According to the vibrational spectra from the water molecules at the surface, assignments of vibrational frequencies arising from bulk water molecules and simulation results found in the literature; it is reported that there are two types of water molecules on gypsum yielding different vibrational signals. Vibrations on one water molecule per unit cell are decoupled and give rise to a signal at 3020 cm^{-1}. On the other hand, symmetric stretching signal on the other water molecule is observed around 3415 cm^{-1}. By controlling the polarization combinations of input and output beams, we were able to determine the orientations of these water molecules at the surface. VSFG spectra were collected from gypsum/air, gypsum/water and gypsum/air interfaces consecutively. Intensity changes in the reported signals indicate that bulk water left a minimal impact on the structure of crystal water at the surface. Reported orientations of the water molecules at the surface in ambient conditions can play an important role in deeper understanding of mechanisms of gypsum dissolution at the molecular level.

Chapter 5. Investigating Spontaneous Adsorption of Sodium Dodecyl Sulfate on Gypsum Surface by using Nonlinear Optical Spectroscopy

Chapter 5 investigates the time dependent change of spontaneous SDS adsorption on gypsum surface. VSFG spectra showed that the orientations of SDS molecules changed upon

evaporation of water from the surface. Intensity change of the signals produced from SDS indicate that molecules were adsorbed from the sulfate headgroup and favoring the carbon chain standing almost perpendicular to the surface plane. Though, after 15 minutes, the chains' angle with the surface plane decreased and they were oriented further parallel with the surface plane. The tendency of SDS molecules to 'lie down' over time agrees with the results presented in Chapter 2.

Chapter 6. Conclusions and Future Directions

Chapter 6 summarizes findings presented in this dissertation and proposes future lines of inquiry that will further illuminate chemistry that occurs on gypsum and other environmentally relevant mineral surfaces.

CHAPTER TWO

SURFACTANT ADSORPTION TO GYPSUM SURFACES AND THE EFFECTS ON SOLUBILITY IN AQUEOUS SOLUTIONS

Contributions of Authors and Co-Authors

Manuscript in Chapter 2

Author: Galip Yiyen

Contributions: Collected and analyzed experimental data. Assisted in writing and editing manuscript.

Co-Author: Kodie V. Duck

Contributions: Collected titration data

Co-Author: Robert A. Walker

Contributions: Assisted with data analysis, writing the manuscript and editing the manuscript.

Manuscript Information

Galip Yiyen, Kodie A. Duck, Robert A. Walker

Langmuir

Status of the Manuscript:
____ Prepared for submission to a peer-reviewed journal
____ Officially Submitted to a peer-reviewed journal
____ Accepted by a peer-reviewed journal
__x__ Published by a peer-reviewed journal

Published by American Chemical Society
Volume 38, Issue 9, 2804-2810
DOI: doi.org/10.1021/acs.langmuir.1c02890

CHAPTER TWO

SURFACTANT ADSORPTION TO GYPSUM SURFACES AND THE EFFECTS ON SOLUBILITY IN AQUEOUS SOLUTIONS

Introduction

Surfactant adsorption to mineral surfaces is a proven strategy used to control conformationally-directed crystal growth and mineral dissolution.[36] Prevailing wisdom posits that surfactants adsorb preferentially to different crystalline faces, slowing growth along specific directions and leading to anisotropic growth/dissolution. As a synthetic strategy, varying surfactant identity and concentration can change particle aspect ratios and shape.[37, 38] Neutral surfactants such as polyvinylpyrrolidone (PVP) are used to control particle size in seeded solutions, while charged surfactants including sodium dodecyl sulfate (SDS) and dodecyltrimethylammonium bromide (DTAB) are often added to particle-containing solutions to modify oxide surface properties for applications such as enhanced oil recovery[39] and pollutant remediation.[40, 41]

Surfactant adsorption to minerals also underpins the practice of froth flotation and mineral recovery.[42] In this process, hydrophilic but sparingly soluble minerals are rendered hydrophobic by first pulverizing the ore (to create particles with diameters ≤ 100 μm), suspending the particles in a slurry and then treating the slurry with a surfactant that binds selectively to the material of choice, forcing those particles to float to the surface.[43, 44] The froth is collected and the desired mineral is cleaned and isolated. The success of froth flotation hinges on choosing surfactants that bind preferentially to specific mineral surfaces at the exclusion of

others. While this process has been employed commercially for well over a century, the development of suitable surfactants and surfactant mixtures has proceeded largely through empirical testing.[45, 46]

To describe froth flotation, models have been developed to describe how mineral particle properties should depend on variables such as surfactant surface coverage and particle size,[46] but few studies have considered the structure and organization of the adsorbed surfactants themselves.[47-54] Such information is critical for understanding the stability of mineral-aqueous interfaces as well as mineral wetting and hydration. Given the increasing importance of surfactant-mineral interactions in both technological and environmental applications, efforts to identify – and even design from computational predictions[55] – surfactants that bind mineral surfaces efficiently are expected to intensify. In this context, testing predictions and validating proposed models with independent, complementary methods will be indispensable for informing and refining mineral recovery and environmental remediation strategies. Studies described below use surface sensitive vibrational spectroscopy, coupled with *ex situ* EDX imaging and bulk solution conductometric titrations to examine SDS and dodecyl-trimethylammonium chloride (DTAC) adsorption to gypsum ($CaSO_4 \cdot 2H_2O$) surfaces and the impact that surfactant adsorption has on gypsum solubility in aqueous solution.

Gypsum is an earth abundant mineral commonly found in sedimentary rock deposits. Commercially, gypsum has many uses including as a building material, as an additive that regulates cement behavior, and as a fertilizer/soil conditioner. Despite its many benefits however, gypsum is also a source of sulfate in ground and surface water, and gypsum dissolution has been tied to rising sulfate levels in rivers and wetlands, especially in areas containing

construction and demolition debris[56] as well as naturally occurring Karst mineral deposits.[57, 58] In this context, sulfate is a common inorganic fouling agent that poses problems for reverse osmosis systems.[59] The EPA has set a secondary maximum contaminant level of 250 mg/L SO_4^{2-} for potable drinking water. At higher sulfate concentrations, contaminated water is no longer suitable for agricultural applications, and concentrations above 3000 mg/L can lead to neurological damage in livestock.[60]

As a mineral commonly found in limestone, sandstone, and other sedimentary rock formations. gypsum has ample opportunity to contribute to ground water and surface water salinity.[61] Recent studies have reported that adding sodium sulfate to the injected solutions used in oil recovery applications slows the rate of gypsum dissolution.[62, 63] Here, the efficacy of additives in preventing gypsum dissolution is assessed by measuring surfactant concentrations in the system effluent and then calculating how much surfactant has been retained.[64] Mechanisms responsible for surfactant-induced retention, however, remain speculative. Results described below show that SDS interacts strongly with gypsum, forming ordered films with surfactant chains aligned with their long axes parallel to the surface. In contrast, equivalent amounts of a cationic surfactant, DTAC, aggregate in a disordered fashion in patches on the gypsum surface leaving large areas of the mineral fully exposed. These behaviors affect gypsum dissolution properties. Gypsum in DTAC-containing solutions (4 mM) dissolves to the same extent as in pure, Millipore water (pH = 5.8), but SDS-containing solutions (4 mM) suppress gypsum dissolution by ~40%. Taken together, these findings present a clear and compelling picture of how two common surfactants associate with an environmentally and economically important mineral surface. These findings motivate additional experimental work and computational

simulations to identify chemically specific forces that control molecular adsorption and organization in hydrogeological systems.

Materials and Methods

Sample and Solution Preparation

Gypsum samples were purchased from Kidz Rocks, Inc. The outer layers of crystal were cleaved with a razor in order to access clean (010) surfaces. The gypsum pieces used for VSFG and FTIR measurements were approximately 1 cm x 1 cm and 3 mm thick; samples used for EDX measurements were smaller, approximately 0.5 cm x 0.5 cm and less than 1 mm thick. To assess the ability of surfactants to organize on a gypsum surface, approximately 2.5 x 10^{-7} moles of SDS and DTAC in aqueous solutions (~150 □L) were applied to the (010) gypsum surfaces and these surfaces were then dried under clean air for 2 hours before performing VSFG and EDX measurements.

Sodium dodecyl sulfate (SDS, ACS reagent, ≥99.0%) and dodecyltrimethylammonium chloride (DTAC, ≥99.0%) were purchased from Sigma-Aldrich. All chemicals were used without further purification. Structures of these molecules are shown in Figure 2.1.

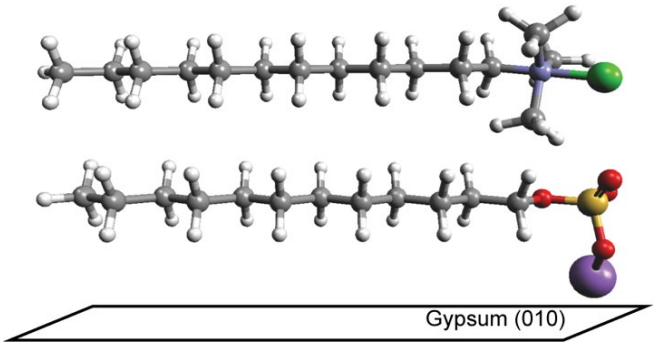

Figure 2.1. Ball and stick structures for both SDS (below) and DTAC (above) molecules. Both surfactants are in all-trans conformations. Structures include each surfactant counterion (Na^+ (purple) for SDS and Cl^- (green) for DTAC). Note that while the SDS solute is shown in a geometry consistent with findings from VSFG measurements (*vide infra*), DTAC adsorbed to the gypsum surface shows no evidence of surface induced ordering.

Unbuffered Millipore water (resistivity 18.2 MΩ) was used to prepare the 4 mM SDS and 4 mM DTAC solutions. Solution pH was unbuffered and measured 5.8 - 6.0. Modest changes in surfactant concentration (2 mM and 6 mM) led to no discernible changes in the observed results. Given a reported point of zero charge (PZC) in aqueous solutions between pH = 2 – 3,[65] we expect that the gypsum surface in these solutions will carry a net negative charge.

Conductometric Titrations

Conductometric titrations are a means for determining the amount of analyte dissolved in solution by observing the change in conductivity of solution that is titrated. In this study, the amount of sulfate arising from gypsum chip dissolution was determined in a variety of aqueous solutions. The important principle in conductometric titration is to choose a titrant having high solubility by itself but having a very low solubility product with the dissolved analyte of interest. We chose $BaCl_2$ as a titrant so that in SO_4^{2-} containing solutions, $BaSO_4$ would form as a precipitate ($K_{SP} = 1.1x10^{-10}$).[66, 67] As long as a precipitate continues to form, the solution conductivity decreases. Once all of the analyte has precipitated, further addition of the titrant

results in an increase in solution conductivity. The minimum in solution conductivity represents the titration's endpoint.[68] Tests with laboratory-prepared standards, showed that this technique is $\geq$ 95% accurate with typical variation of $\leq$ 2.5% about the mean.

EDX Mapping

EDX images were acquired using a PHI 710 Auger NanoProbe. Gypsum pieces were mounted on a tilted (30 degree) sample holder. To minimize surface charging, gypsum samples were irradiated with low energy ions (~70 eV) from an Ar^+ sputtering gun. The ion beam energy used for analyses was 5 keV.

FTIR Analysis

Gypsum pieces (1 cm x 1 cm) were immersed in 4 mM SDS and DTAC solutions for up to 5 days. The DTAC solution remained clear, but the SDS solution became cloudy within 1 day. The precipitate observed in gypsum/SDS solutions was dried under clean air on a ZnSe window so that IR absorption experiments could be performed.

All FTIR measurements were performed with a Bruker VERTEX 70. Spectra were collected between 400-7000 cm^{-1} and were composed of an average of 32 scans with 1 cm^{-1} resolution.

Vibrational Sum Frequency Generation.

Vibrational sum frequency generation (VSFG) spectroscopy is a second order, nonlinear optical technique used to measure vibrational spectra of molecules at interfaces. In order for vibrational transitions to be VSF allowed, they must be both IR and Raman active and in an anisotropic environment. Molecules in bulk materials having inversion symmetry or in solution will not give rise to a VSF response. Similarly, adsorbates that are randomly distributed and/or

disordered at a surface will also be VSF silent. Additional information about VSFG as a technique can be found in several instructive reviews.[69-71]

VSFG data presented in this work were acquired using an assembly previously described.[72-74] Briefly, 800 nm output from an amplified Ti:sapphire laser (3.4W, 1 kHz, 85 fs) (Coherent Libra-HE). was split so that 80% of the intensity was used to pump a Coherent OPerA Solo that was tuned to produce IR light centered in the -CH stretching region (3400 nm, ~200 cm^{-1} bandwidth). The remaining 800 nm light was spectrally narrowed with a home-built pulse shaper to have a ~15 cm^{-1} FWHM. Visible and IR beams were focused on the air-solid interface for 60 seconds for each measurement and VSF signal was collected with a 1340 × 100 pixel CCD (PIXIS100B, Princeton Instruments). Typical visible and IR powers were 50 mW and 20 mW, respectively. Band intensities were normalized to the corresponding nonresonant response from a gold surface.[75]

Results and Discussion

Conductometric Titration

Gypsum pieces with varying masses were placed in aqueous and surfactant containing solutions and allowed to sit for 5 days. The pieces were then removed from solution and aliquots from these solutions were titrated with $BaCl_2$. Sulfate concentrations in different solutions were found by determining the end points of conductometric titration curves. For each sample, the amount of sulfate in solution was normalized by the mass of the parent gypsum piece prior to immersion. Even prior to the titration analysis, clear differences between the solutions were apparent. While gypsum/DTAC and gypsum/Millipore solutions remained clear after 5 days, the gypsum/SDS solution was extremely cloudy and particles in the precipitate were visible to the

naked eye. Following this observation, a solution with $CaCl_2$ and SDS was prepared and similar precipitation behavior was observed immediately. Previous work has reported $Ca(DS)_2$ precipitation as a result of an interaction between Ca^{2+} and SDS anions in solution.[76, 77] Baviere et al, reported that in a solution with dodecyl sulfate concentration at 4 mM, $Ca(DS)_2$ precipitation was observed with Ca^{2+} concentrations varying from 0.02 mM to at 7 mM.[78] Representative results from conductometric titrations performed with the Millipore, DTAC and SDS solutions are shown in Figure 2.2. In these plots, dashed lines represent titration end points after analyzing the data with nonlinear regressions. Results from repeated measurements were normalized to the original gypsum masses and are reported in Table 2.1 (expressed in terms of % material dissolved). Data show less free sulfate in the SDS-containing solution compared to DTAC (4 mM) and Millipore solutions. These findings show that SDS suppresses dissolution by ~40% relative to pure water and solutions containing the cationic DTAC. By converting the dissolved material into molar quantities, we estimate the sulfate concentrations in the solutions range from 260 mg/L (SDS) to 530 mg/L (DTAC and Millipore).

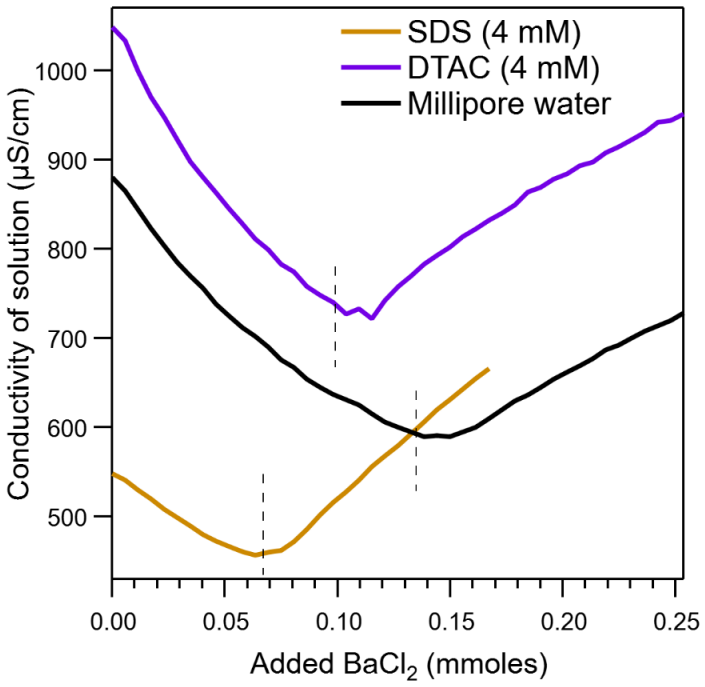

Figure 2.2. Sample titration curves from each titration set

Table 2.1. Percentage of amount of sulfate found in different solutions after normalized to mass of gypsum pieces before dissolution

Type and number of samples	**Amount of sulfate normalized to mass of gypsum before dissolution**	**Standard Deviation**
SDS (4 mM) n=5	5.34%	1.3%
DTAC (4 mM) n=3	8.37%	2.4%
Millipore water n=6	9.00%	0.5%

We note that the amount of free sulfate determined from the conductometric titrations with SDS solutions is an upper limit. Ba^{2+} not only forms a precipitate with SO_4^{2-} but also with

the sulfate headgroup on SDS. To confirm this effect a 3.5 mM SDS solution (e.g. no free dissolved sulfate) was titrated with $BaCl_2$ as a control measurement. As expected, a stoichiometric analysis of the data showed that each barium cation complexed with two dodecyl sulfate groups and precipitated. In other words, if Ba^{2+} precipitates primarily with free sulfate but also with any remaining SDS that remains uncomplexed with dissolved Ca^{2+}, then the endpoint in the conductometric titrations will represent the amount of Ba^{2+} required to complex with SO_4^{2-} *and* SDS meaning that the calculated amount of free sulfate will be greater than the actual amount in solution. As a result, we conclude that gypsum solubility in the SDS solution is significantly less than in solutions of pure Millipore water and solutions containing the cationic surfactant, DTAC.

VSFG

Gypsum pieces with 1 cm x 1 cm dimensions were placed on a sample stage and VSFG spectra were collected from freshly cleaved samples and samples that had been exposed to both SDS and DTAC solutions that had been allowed to dry. Figure 2.3 shows VSFG spectra acquired in the CH stretching region under different polarization conditions from a freshly cleaved gypsum (010) surface and one that was treated with ~150 µL of a 4 mM DTAC solution. No signal was observed from either sample, regardless of experimental polarization conditions. However, treating a gypsum surface with an equivalent volume of 4 mM SDS led to a visibly observable precipitate layer on the surface and relatively strong VSFG signals (Figure 2.4).

Several different scenarios can lead to an absence of VSFG signal from a surface. First, if no species with appropriate functional group vibrations are present, no response is expected. This situation describes the gypsum surface treated with Millipore water where no -CH containing

species are present. Second, if species having vibrational structure in the region of interest *are* present but disorganized, the functional groups will experience no net anisotropy and the corresponding second order susceptibility ($\chi^{(2)}$) will be zero. Finally, if adsorbates *are* ordered but organized in a way that is symmetric with respect to inversion, oscillating functional group hyperpolarizabilities will be out of phase leading to cancelation and, again, no detectable VSFG response. The absence of any signal from the DTAC treated gypsum surface leads us to believe that the surfactant remaining after the applied solvent had evaporated are disordered across the surface.

VSFG spectra from gypsum surface treated with SDS show distinct, complementary features under SSP, SPS and PPP polarizations conditions (Figure 2.4). In total, four distinct vibrational bands appear in the spectra, corresponding to a methylene symmetric stretch (d^+, 2850 cm^{-1}), a methyl symmetric stretch (r^+, 2883 cm^{-1}), a methylene anti-symmetric stretch (d^-, 2920 cm^{-1}), and a methyl antisymmetric stretch (r^-, 2960 cm^{-1}). The d^- feature is broad and likely contains contributions from methyl bending overtones that become symmetry allowed through Fermi resonance interactions.[79, 80]

While these features are common to VSFG spectra of alkyl chain-containing species,[81, 82] relative band intensities as a function of sum, visible and IR polarizations are unusual in the SDS on gypsum spectra shown in Figure 2.4. The dominant d^- intensity in the SSP spectrum implies that surfactant chains are lying parallel to the surface with the local methylene C_2 axes also parallel to the surface. This picture is supported by the SPS spectrum and relevant vibrational band intensities. Specifically, if alkyl chains were lying down with each methylene group in contact with the surface, then symmetry conditions lead one to expect a measurable d^+ response

(assuming that the adsorbed surfactants have a net polar ordering *and* are not in all-*trans* conformations). Similarly, one can also anticipate such an arrangement to lead to a strong r^+ signal. Inspection of the spectra in Figure 2.4 shows these predictions to be borne out. Similar observations have been reported recently by Bryantsev and coworkers who used predictions from computational studies to design and then study strongly binding bis-phosphinate ligands adsorbed to rare-earth containing bastnäsite samples.[55]

Figure 2.4 also shows an FTIR absorbance spectrum of the precipitate collected and dried from gypsum/SDS solution. In general, vibrational features appearing in the VSFG spectra match well with features in the FTIR absorbance spectrum. We note that the FTIR spectrum does contain additional features at 2940 and 2980 cm^{-1} although these may be obscured in the VSFG data by the poorer (~20 cm^{-1}) resolution. We also observe that the r^+ feature in the SPS and PPP VSFG spectra is blue shifted (2884 cm^{-1}) relative to the equivalent band assigned in the FTIR spectrum (2872 cm^{-1}). Computational studies predict that strong interactions between methyl groups and halide anions can lead to CH stretching vibrations shifting to higher frequencies.[83] Given the daily calibration performed with the VSFG assembly, we believe the r^+ shift observed in Figure 2.4 is real and may reflect the methyl group interacting directly with sulfate anions on the gypsum surface. We emphasize, however, that this hypothesis is speculative and in need of testing.

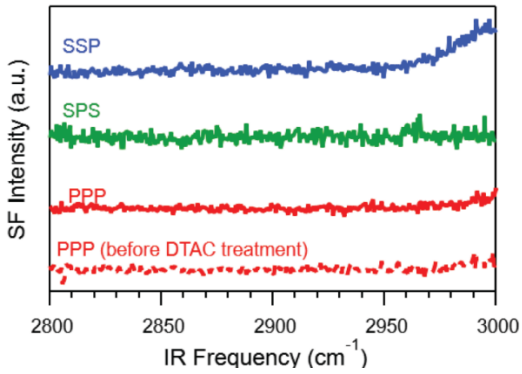

Figure 2.3. VSFG spectra from gypsum surface before and after treatment with 4 mM DTAC. Spectra were offset vertically for clarity.

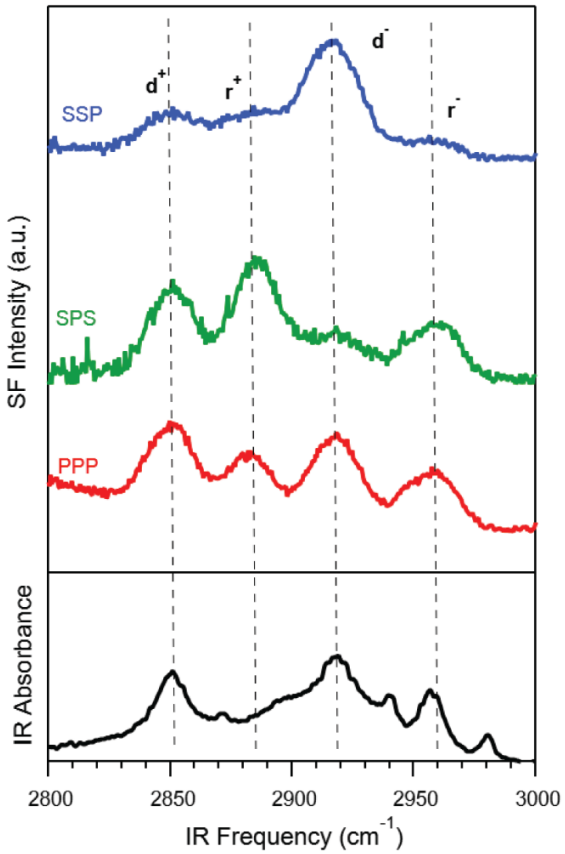

Figure 2.4. VSFG spectra from gypsum surface before and after treatment with 4 mM SDS; and FTIR absorbance spectrum of the precipitate isolated from gypsum/SDS solution. VSFG spectra were offset vertically for clarity. Dashed vertical lines are included as visual guides.

Summarizing the VSFG results and interpretation, we conclude that DTAC does not interact strongly with the gypsum surface and the cationic surfactant left behind after solvent evaporation forms disordered aggregates with no net polar ordering. In contrast, an equivalent amount of SDS *does* adsorb to gypsum, effectively 'wetting the surface' and creating surface structures that have long-range order and a correspondingly strong second order nonlinear optical response. Furthermore, the SDS alkyl chains appear to have a well defined structure relative to the surface, with the chains lying flat and the local C_2 symmetry axes of methylene groups parallel to the surface. We infer that the interactions between the chains and the surface as well as between the chains themselves minimize the amount of intramolecular motion given the relatively strong intensities of both d^+ and r^+ in the SPS spectrum.[84] Based on results from conductometric titrations, we also infer that this strong gypsum-SDS interaction disrupts water structure at the surface and impedes gypsum dissolution. In a global sense, these results support an adsorption mechanism where species specific binding ($-OSO_3^-$ of the SDS to the Ca^{2+} on the gypsum surface) is strong enough to overcome the overall negative charge associated with this material surface at an experimental pH of 6.

EDX

To learn more about surfactant structure and organization at the gypsum/air interface, we acquired EDX images from gypsum that had been treated with either SDS or DTAC. Figure 2.5 shows EDX images of element distributions across the surfaces of gypsum pieces treated with solutions containing 4 mM SDS (left) and DTAC (right).

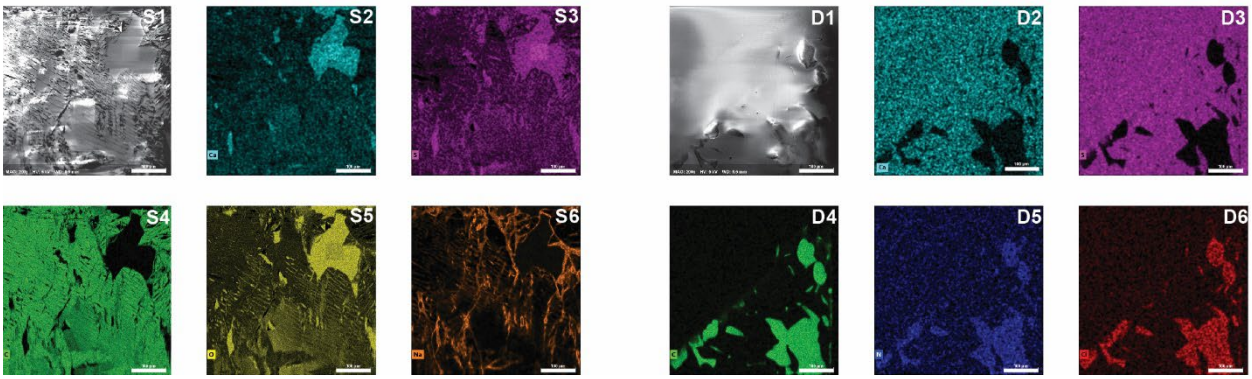

Figure 2.5. EDX images captured from surfaces of two gypsum pieces after SDS treatment (S1 to S6) and DTAC treatment (D1 to D6). The scale bar represents 100 µm. Panels S2 and D2 show Ca; panels S3 and D3 show S; panels S4 and D4 show C; panel S5 shows oxygen; panel D5 shows N; panel S6 shows Na and panel D6 shows Cl

Following exposure to the surfactant containing solutions, the aqueous solvent was allowed to evaporate for 2 hours under a stream of clean air. For the SDS-treated surface, elemental mapping shows a relatively uniform carbon distribution across the surface (S4). Furthermore, we observe calcium only at the site/defect where carbon is absent (S2). The other unique diagnostic from the SDS treated surface is the distribution of Na that also appears across the surface in filamentous-like pattern (S6). Closer inspection of Figures S4 (carbon) and S5 (sulfur) show 8-12 µm length striations in the elemental distributions implying a degree of organization within the adsorbed surfactants, consistent with conclusions drawn from the VSFG results reported above. In contrast, the unique indicators of DTAC on the gypsum surface – carbon, nitrogen and chlorine – are all spatially correlated with each other and their distributions are localized to a small areas within the 0.5 mm x 0.5 mm field of view. We note the same elemental exclusion effects observed for the SDS treated sample, namely that in combination with the raw SEM image (D1), the DTAC elemental distributions show that the cationic surfactant assembled at the topographically rough patch of the gypsum surface, and the surfactant did not have a strong

enough affinity to spread across the substrate. Again, this result is consistent with VSFG spectra that implied no net DTAC polar ordering across the gypsum surface.

Conclusions

In an effort to understand experimental conditions that affect gypsum dissolution into aqueous solution, conductometric titrations demonstrated that solutions containing the anionic surfactant SDS at sub-micellar concentrations measurably suppressed gypsum dissolution while a corresponding cationic surfactant, DTAC had no measurable impact. Subsequent surface specific vibrational experiments showed that gypsum surfaces exposed to SDS solutions where the solvent was then allowed to evaporate were covered with an ordered surfactant film where the alkyl chains adopted a conformation with their long axes approximately parallel to the surface plane. In contrast, gypsum exposure to a DTAC containing solution showed no such polar ordering amongst the surfactants. Complementary EDX images confirmed conclusions drawn from the vibrational data by revealing a uniform carbon coating across the gypsum surface that had been treated with SDS. The DTAC treated surface showed all of the carbon collected in localized patches, leaving large expanses of the gypsum surface uncoated.

One suggestive consequence emerging from the findings reported in this work is that the well-ordered, long-range organization created by SDS surfactants adsorbing to the aqueous/gypsum interface is that the now-hydrophobic gypsum surfaces may disrupt water structure and limit gypsum solubility. Such molecular level insight would provide meaningful data for models being developed to predict the environmental impact of organic matter adsorbed to mineral surfaces.

CHAPTER THREE

ACCURATELY DETERMINING GROUNDWATER SULFATE CONCENTRATIONS FROM RECLAIMED LANDSCAPES WITH CONDUCTOMETRIC TITRATIONS

Contributions of Authors and Co-Authors

Manuscript in Chapter 3

Author: Galip Yiyen

Contributions: Collected samples and experimental data. Analyzed experimental data. Assisted with writing and editing manuscript.

Co-Author: Kodie V. Duck

Contributions: Collected experimental data

Co-Author: Elizabeth Meredith

Contributions: Collected samples and assisted with editing the manuscript

Co-Author: Robert A. Walker

Contributions: Assisted with data analysis, writing the manuscript and editing the manuscript.

Manuscript Information

Galip Yiyen, Kodie A. Duck, Elizabeth Meredith, Robert A. Walker

Status of the Manuscript:

___ Prepared for submission to a peer-reviewed journal

_x_ Officially Submitted to a peer-reviewed journal

___ Accepted by a peer-reviewed journal

___ Published by a peer-reviewed journal

CHAPTER THREE

ACCURATELY DETERMINING GROUNDWATER SULFATE CONCENTRATIONS FROM RECLAIMED LANDSCAPES WITH CONDUCTOMETRIC TITRATIONS

Introduction

Ground and surface water salinity is a growing threat to ecosystem and human health[4, 9, 85-89]. As the threat grows, individuals and communities increasingly require fast, accurate methods for assessing not only how much salt is in the water but also salt speciation. Depending on the analyte of interests, analytical labs remote from the sampling site(s) will use different EPA-approved techniques such as atomic emission spectroscopy, mass spectrometry, ion chromatography and colorimetry to identify and quantify water contaminants[90-93]. While these processes lead to accurate, validated data, the measurements themselves require careful handling and transport of field samples and often require additional processing before results are acquired. The time between collecting a sample in the field and having results in hand can be weeks, and the cost of these analyses are often prohibitive to end users who must determine if water is safe for use.

One contaminant of concern in the central and mountain west of the United States is sulfate[94]. Even though there is not a Federally enforceable regulation, sulfate has a secondary maximum contaminant level of 250 mg/L in drinking water provided by EPA[18]. High sulfate concentrations are known to adversely affect people if concentrations rise above 500 mg/L[28]. In addition, sulfate concentration above 2500 mg/L result in weight loss and health problems in cattle, and cattle begin to suffer neurological disorders when sulfate concentrations rise above

3000 mg/L[28]. Finally, sulfate salts in soil create an imbalance of adsorbed ions in sensitive crops by limiting calcium uptake while promoting potassium and sodium uptake[95].

Sulfate concentrations exceeding the human and/or cattle health standard levels are common in Powder River Basin (PRB) in Montana and Wyoming. This region is home to some of the largest open air coal mines in the world[22]. The large-scale disruption to the local landscape resulting from these mining activities alters groundwater composition. In the PRB, these disruptions create greater access to soluble gypsum ($CaSO_4 \cdot 2H_2O$) in evaporites leading to unacceptable high sulfate concentrations[96-98]. Degraded water quality impacts local agriculture and ranching in the PRB, meaning that farmers and ranchers must regularly assess water from wells and streams to ensure it is suitable for irrigation and for livestock. Given seasonal variability in ground and surface water flow and long-term changes in water tables and groundwater composition, regular evaluation of water quality and contaminant speciation is necessary to ensure human, animal and ecosystem health.

Studies described in this work develop and apply conductometric titration methods to quantify the amount of sulfate in groundwater samples collected from a reclaimed open-air coal mine site in southeast Montana. The mine itself operated from 1969 – 2003, and land-surface reclamation began at that time. In 2022, the first of several phase IV bonds was released when the reclamation process was completed and the land surface returned to private ownership. Sulfate concentrations are measured in samples taken from 12 sites (8 groundwater, 4 surface water) on three separate occasions at and surrounding reclaimed land overlaying the original spoils pile of a former open-air coal mining site. Conductometric titration measurements performed with these samples demonstrate this method's utility as a rapid and accurate tool for

evaluating sulfate concentrations. Conductometric titration data are compared to concentrations determined from independent ion chromatography measurements performed using split samples. Agreement between the two measurements is quite good with an average difference of ±3.6% for a given sample. To test the generality of conductometric titration as a tool for assessing ion concentrations in environmental systems, we also use this technique to measure chloride concentrations in several rivers and streams in south central and southwest Montana. These results are also validated by comparing with data from independent ion chromatography analyses and reinforce the notion that this simple, inexpensive technique can be a useful tool for rapid, accurate water quality assessment.

Materials and Methods

Proof of Principle (SO_4^{2-} analysis)

Conductometric titration has been used previously to analyze different analyte concentrations[99, 100]. While the analyte and titrant will vary depending on the intended application, the technique's principle is the same: for the given (charged) analyte of interest, a suitable complexation agent is titrated into the solution and the conductivity is measured. As the analyte and agent precipitate, the solution's conductivity diminishes until the analyte has been removed from solution. Addition of titrant past the endpoint results in the solution's conductivity rising. From the minimum in the conductivity vs. titrant added data, one can readily calculate how much of the analyte was in the original solution.

Even though conductometric titration is more commonly used for analyses of acids or bases as an alternative to pH titrations, its potential for sulfate analysis was investigated and proven successful by Garcia and Schultz in an undergraduate laboratory experiment[101], as well as

for laboratory-controlled, gypsum dissolution experiments[35]. This technique, however, has not been previously adapted to examine chemically complex aqueous solutions having high ionic strengths and, to our knowledge, data from conductometric titration experiments have not been benchmarked against more conventional, analytical techniques traditionally used to assess groundwater quality.

For experiments performed in this study, ground and surface water samples believed to have high sulfate concentrations are titrated with 8.6 mM $BaCl_2$. $BaSO_4$ has very low aqueous phase solubility (2.4 mg/L at 20 °C, $K_{sp}=1.1\times10^{-10}$)[102, 103]. During this precipitation process, sulfate contribution to overall conductivity is replaced by conductivity contribution with two equivalent dissolved chloride ions. The equivalent conductivities (Λ) for ½ SO_4^{2-} and Cl^- are 80 cm^2-S/mol and 76.3 cm^2-S/mol, respectively[104]. $BaSO_4$ precipitation results in decrease in overall conductivity due to precipitation of SO_4^{2-} ions and dilution upon titration. For each removed SO_4^{2-} ion, two equivalents of Cl^- is added to sample, mostly compensating for the conductivity deficit created by sulfate removal (-160.0 cm^2-$Smol^{-1}$ + 152.6 cm^2-$Smol^{-1}$). Therefore, the observed conductivity decrease is mainly the result of dilution. A more detailed, mechanistic examination of the physical origins of individual conductivities, deviation in molar ionic conductivities for different species in different concentrations and the accompanying Kohlrausch formalism is beyond the scope of this study. After all of sulfate has precipitated from solution, stepwise addition of $BaCl_2$ increases solution conductivity (Figure 3.1). By recording conductivity vs. volume of titrant added, one can readily observe when the slope of these data change from negative to positive. With this ‘endpoint’, one can then quickly calculate the amount of sulfate in the original solution (Figure 3.1).

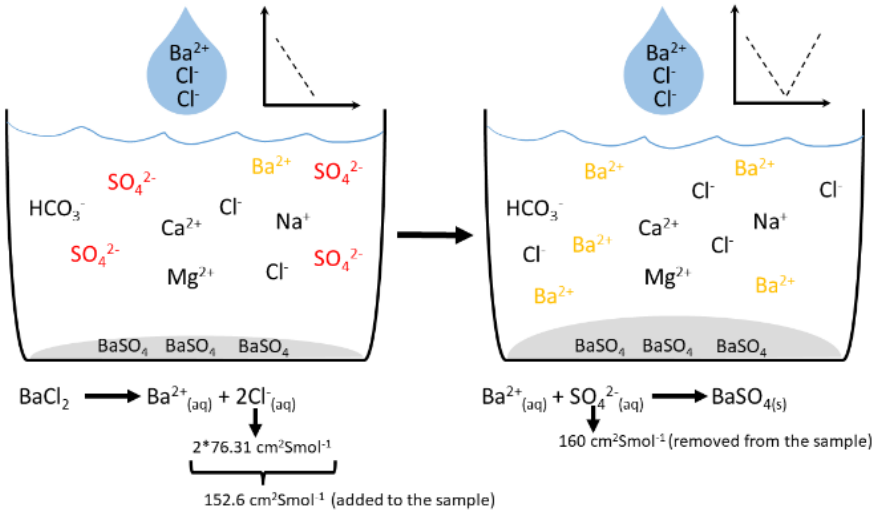

Figure 3.1. Scheme representing principle of conductometric titration for sulfate analysis

This technique's sensitivity limit was tested by titrating $MgSO_4$ solutions prepared in Millipore water (18.2 MΩ·cm resistivity). Our trials showed that down to 100 ppm sulfate could be quantified with an accuracy of 7.6%.

Extending Method Generality (Cl^- Analysis)

To test the ability of conductometric titration to quantify other inorganic ions in environmental aquatic systems, we also performed experiments to measure aqueous phase chloride concentrations. In this context, the chloride ion is commonly used as a natural tracer in ground and surface water systems[105, 106]. Silver (Ag^+) was chosen as the complexation agent given AgCl's low solubility (1.6 mg/L at 20 °C)[102]. Conductivity contributions from Cl^- ions in the sample is replaced by conductivity of NO_3^- ions (Λ-=71.42 cm^2-$Smol^{-1}$ for NO_3^-), leading to a conductivity decrease[104]. After all of the chloride has precipitated, further addition of $AgNO_3$ increases overall conductivity of solution and amount of chloride can be calculated by using the end point in titration curve.

Materials

Groundwater samples were collected from wells located in two watersheds on opposite sides of Rosebud Creek in southeast Montana. Surface water samples were acquired from Rosebud Creek itself, several miles upstream from Colstrip, MT (Figure 3.2). Samples were filtered through membranes with 0.45 μm pore size and stored in closed containers until analyzed. Conductometric titrations for December 2020 and May 2021 samples were done with PASCO Wireless Conductivity Sensor (model PS-3210), while titrations for August 2021 samples and chloride analysis were done with Mettler-Toledo FiveGo conductivity meter (model F3). Ion chromatography measurements for sulfate were performed using EPA method 300.0 at the Montana Bureau of Mines and Geology Analytical Laboratory in Butte, Montana[107]. Solutions containing the complexation agent were prepared with Milli-Q ultrapure water having 18.2 MΩ·cm resistivity. $BaCl_2$ (anhydrous, Fisher Chemical™) solutions used as a titrant for SO_4^{2-} precipitation were prepared with concentrations of 1800 mg/L.

Chloride analyses were conducted for surface water samples collected from Bozeman Creek and three different locations on Upper Clark Fork River (UCFR). Chloride titration results are benchmarked against ion chromatography (IC) analysis in The Environmental Analytical Lab at Montana State University (EAL-MSU). IC measurements for chloride analysis used an AS18 column in Dionex ICS-2100 (Thermo Fisher Scientific, Inc.). Concentrations of $AgNO_3$ (99.5%, Fisher Chemical™) used for chloride analyses varied between 430 mg/L and 720 mg/L.

Results and Discussion

Environmental Samples (Sulfate analysis)

Researchers across Montana are engaged in a widespread effort to understand the impact of economic activity on water quality in local streams and rivers[108-111]. One result of this work has been extensive cataloging of contaminants in several different watersheds[17]. Water samples tested for sulfate were taken from 8 different wells and 4 different surface water sites along Rosebud Creek in SE Montana. As noted in the introduction, this region is known for having high sulfate levels due to its geology. Open air coal mining results in even higher sulfate concentrations after land reclamation[112]. Locations of the sampling sites are shown in Figure 3.2 and precise geographic data and elevations are reported in Supporting Information. Wells were installed in August 2020 and samples tested in this work were collected in December 2020, May 2021 and August 2021. Water temperatures were measured onsite, while pH and conductivities were measured not only onsite but also in the lab. Samples from each site were split for independent testing and analysis. These data are publicly available[17] and concentrations of selected ions from the December 2020 measurements are reported in Table 3.1.

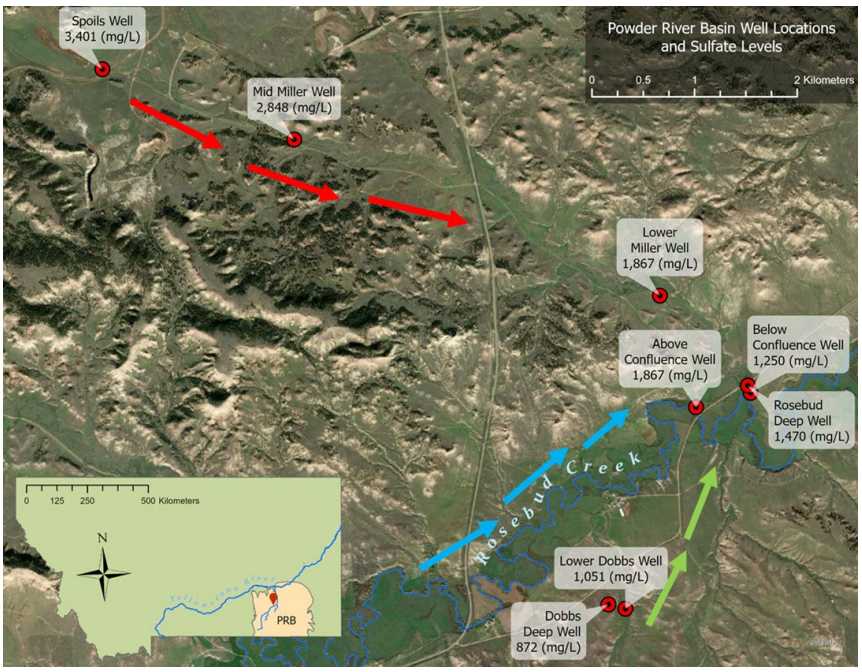

Figure 3.2. PRB map showing the locations where samples were collected and sulfate levels in December 2020. The red arrows show groundwater flow from the reclaimed coal mine (Miller Coulee). The blue arrows show the surface water flow direction of Rosebud Creek. The green arrows show the groundwater flow from the undisturbed drainage (Dobbs Coulee).

Table 3.1. Concentrations of selected environmentally related ions (mg/L), pH and conductivities (µS/cm) from samples collected in December 2020 in selected sites[17].

	SO_4^{2-}	Cl^-	HCO_3^-	Ca^{2+}	Mg^{2+}	Na^+	pH	Conductivity
Spoils Well	3274	29.5	580.6	420.6	588.0	240.3	7.06	4606.8
Below Confluence Well	1316	12.4	507.2	106.6	134.5	399.1	7.56	2884.8
RBC @blw confluence	592.5	9.5	594.3	102.4	135.7	119.9	8.27	1808.0
Dobbs Deep Well	942.6	25.3	1186	153.6	225.6	250.0	7.14	2879.1

If sample conductivities were too high to be titrated with the stock $BaCl_2$ solution, samples were diluted with Millipore water (18.2 MΩ·cm resistivity). To check the accuracy of titration data, results were compared against independent measurements of total sulfur content using IC measurements by EPA method 300.0. Over 36 different measurements, agreement between titration and IC data was quite good with an averaged discrepancy of ±3.6% and a maximum disagreement of 11.3%. Titration and IC data are summarized in Table 3.2. We note here that the time required to perform a titration (including preparing the $BaCl_2$ solution, setting up the titration assembly and analysis) is approximately 2 hours and the 'material cost' of an experiment is < $5 considering the conductivity meter and glassware as one-time-only capital equipment investments. Both metrics are attractive given the time and cost of sending field samples for analysis at an independent laboratory.

Table 3.2. Sulfate concentrations in ground (**bold**) and surface water *(italics*) from sites collected from and near Rosebud Creek (RBC) and a comparison of results obtained from both conductometric titration and IC. Numbers in parentheses in the first column indicate well depths[17]. Locations of these sampling sites can be found in Figure 3.2.

Sample Location	Titration SO_4^{2-} (mg/L)			IC - EPA Method 300.0 data SO_4^{2-} (mg/L)[17]			Percent Difference		
	Dec-20	*May-21*	*Aug-21*	*Dec-20*	*May-21*	*Aug-21*	*Dec-20*	*May-21*	*Aug-21*
Spoils Well (36 ft)	3274	3450	3223.2	3401	3567	3299	-3.7	-3.3	-2.3
Below Confluence Well (32 ft)	1316	1257	1252	1250	1169	1134	5.3	7.5	10.4
RBC @ blw conf	592.5	515.0	1142	553.2	470.4	1134	7.1	9.5	0.7
Dobbs Deep Well (104.5 ft)	942.6	898.6	866.5	872.1	818	852.2	8.1	9.9	1.7
RBC @39	570.6	456.1	1057	552	452.5	1034	3.4	0.8	2.2
RBC @ McRae	561.2	467.0	786.1	563.7	477.4	783.6	-0.4	-2.2	0.3
Mid Miller Well (17.7 ft)	2829	2446	2625	2848	2527	2545	-0.7	-3.2	3.1
Rosebud Deep (93 ft)	1428	1390	1441	1470	1366	1444	-2.8	1.8	-0.2
Lower Miller Well (37.3 ft)	1804	1774	1819	1867	1829	1846	-3.4	-3.0	-1.4
Lower Dobbs Well (Dobbs Shallow) (45 ft)	1038	947.5	916.7	1051	992.7	1034	-1.3	-4.5	-11.3
RBC @ Cow	640.3	521.1	1301	621.4	523	1294	3.0	-0.4	0.5
Above Confluence Well (14.6 ft)	1678	2121	2261.6	1867	2119	2256	-10.1	0.1	0.2

Environmental Samples (Chloride Analysis)

Chloride analyses were performed using field samples taken from the Upper Clark Fork River and a local stream in Bozeman, MT. Independent testing of Cl^- concentrations was performed by the Montana State University Environmental Analytical Laboratory also using ion chromatography.

Like the samples tested for sulfate, agreement between the titration and chromatography chloride measurements is quite good. In the case where we observe a large percentage difference between concentrations reported by the two methods, the absolute difference is 0.3 ppm for an absolute concentration of ~2 ppm. For the UCFR samples having higher Cl^- concentrations, agreement between the two methods was < 6%. Disagreement between measurements at low concentrations likely represents a limit to conductometric titration's ability to test for ion concentration. This limit will vary from species to species and depends on the complexation scheme used to precipitate the ion of interest out of solution.

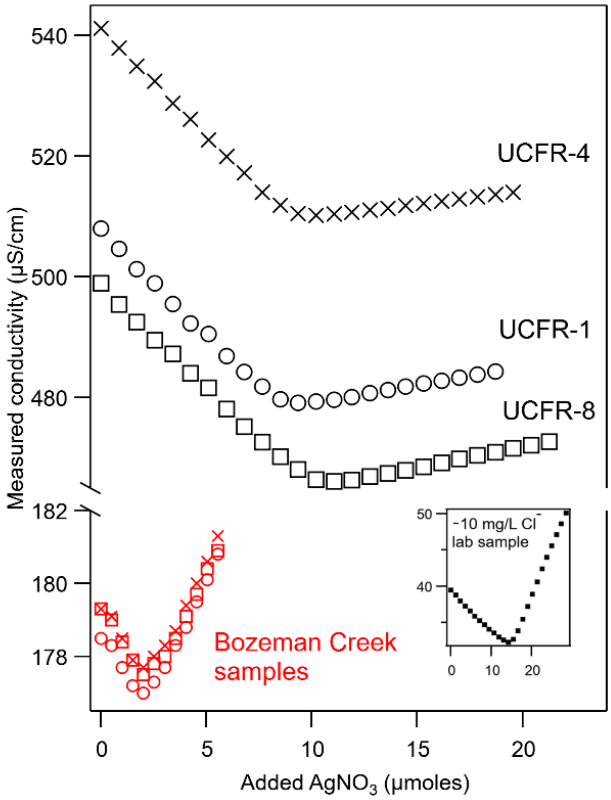

Figure 3.3. Chloride titration curves from a sample prepared with NaCl and Millipore water (bottom right), environmental samples collected from Bozeman Creek (3 trials) and from three different locations on UCFR.

Table 3.3. Chloride concentrations determined by conductometric titrations and ion chromatography

	Cl^- concentration - conductometric titration (mg/L)	Cl^- concentration - Dionex ICS-2100 (mg/L)	Percent difference
Bozeman Creek (n=3)	2.25 ± 0.1	1.92 ± 0.29	17.2%
UCFR-1	10.21	10.04 ± 0.23	1.7%
UCFR-4	10.81	10.26 ± 0.24	5.4%
UCFR-8	11.99	11.84 ± 0.23	1.3%

Correlation Between Conductivities and Sulfate Concentrations

The close agreement between sulfate concentrations in the groundwater and Rosebud Creek samples determined by conductometric titration and ion chromatography raises the question if an even simpler measurement can be used to determine ion concentrations in ground and surface water where the hydrogeology is well defined and historically cataloged. Figure 3.4a plots sulfate concentrations vs. sample conductivity using the sulfate concentrations measured by conductometric titration. Also shown in the smaller plots are the concentration data of five other ions vs. conductivity. Data used for these figures are publicly available at the Ground Water Information Center (GWIC)[17]. Ions were chosen based on their relative abundance. For individual data sets, the correlation between SO_4^{2-} concentrations and conductivity is high ($R^2 \geq 0.91$). Combining all of the sulfate concentrations across multiple data sets (Figure 3.4b) shows slightly reduced correlation ($R^2 = 0.86$) but still high enough to estimate sulfate concentrations based on conductivity measurements with reasonable confidence.

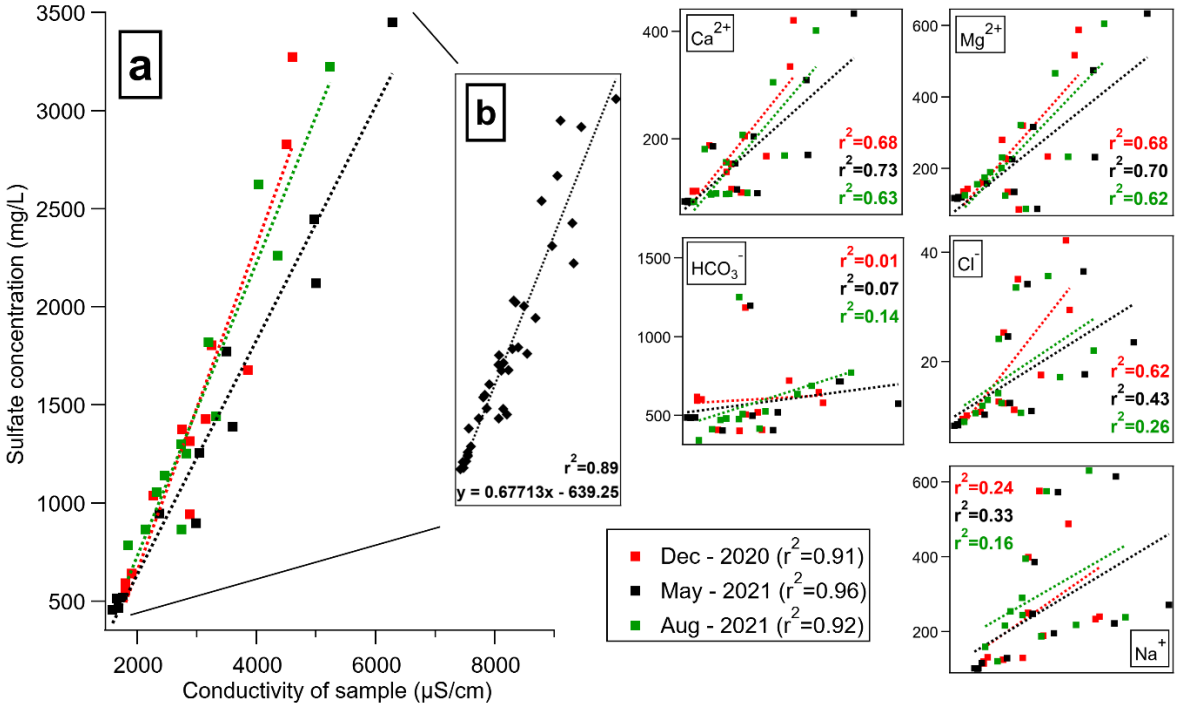

Figure 3.4. (a) Conductivity and individual ion concentration correlations for three different sampling periods and (b) correlation between conductivity and sulfate concentrations (three sampling periods combined). Concentrations on the y-axes are in mg/L. Conductivity ranges on x-axes in the small graphs on the right two columns are as follows: 1600-7500 µS/cm (Ca^{2+}); 1600-6800 µS/cm (Mg^{2+}); 1600-6300 µS/cm (HCO_3^-); 1600-7200 µS/cm (Cl^-); 1100-6300 µS/cm (Na^+)

Not surprisingly, correlations between divalent cations Ca^{2+} and Mg^{2+} and bulk conductivities are observed – R^2 = 0.68 and 0.67, respectively – but not as strongly as for SO_4^{2-}. Correlation with monovalent anions and cations is very low. From these data, we propose that in the regions having high sulfate concentrations and where data have been cataloged previously, a simple water conductivity measurement can be used to estimate sulfate concentrations. We tested this hypothesis using conductivity data from a new set of samples collected in May 2022. Using the correlation shown in Figure 3.4-b, simple conductivity data predicted sulfate concentrations to within ±13%. A correlation between predicted and measured sulfate concentrations are shown

in Figure 3.5. Conductivity and concentration data from the May 2022 samples are reported in supporting information.

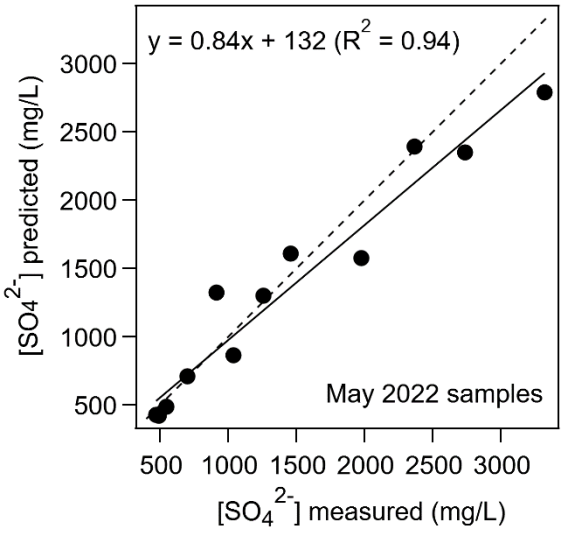

Figure 3.5. Correlation between predicted sulfate concentrations (y axis) and measured sulfate concentrations (x axis) using the correlation derived from sulfate-conductivity data shown in Figure 3.4b. The solid line shows the best linear fit to the data. The expression is included on the graph. The dashed line with a slope of 1.0 is included to illustrate ideal agreement.

Agreement between predicted and measured sulfate concentrations is quite good (R^2 = 0.94) with deviations $\leq \pm 15\%$ in most cases. While the accuracy of sulfate concentrations predicted from conductivity would not be sufficient for careful analytical analysis, we stress that results should be more than accurate enough for local users of surface or groundwater to evaluate if sulfate concentrations are low enough for the water to be used for an intended application. Further work will be necessary before determining whether or not such close correlations hold for aqueous phase ions of interest in other environmental water samples.

Conclusion

The studies described above show conductometric titration to be capable of rapidly and accurately measuring sulfate concentrations in ground and surface water samples having high sulfate concentrations. Good agreement was observed between the titration-deduced sulfate concentrations and independent, quantitative IC measurements by an EPA approved method. The technique proved adaptable for also measuring ~10 ppm chloride concentrations in different surface water samples. The chloride data agreed with independent IC analysis. Given the relative ease, speed, and accuracy of conductometric titration measurements, this technique stands out as an attractive means of assessing sulfate concentrations quickly when end users must make real-time decisions with regards to water usage. Results presented in this study also indicate that low cost and publicly more accessible 'conductivity based' water analysis techniques can be developed in the future.

CHAPTER FOUR

NONLINEAR OPTICAL STUDIES OF WATER AT GYPSUM/AIR AND GYPSUM/AQUEOUS INTERFACES

Contributions of Authors and Co-Authors

Manuscript in Chapter 4

Author: Galip Yiyen

Contributions: Collected and analyzed experimental data. Assisted with writing and editing the manuscript

Co-Author: Robert A. Walker

Contributions: Assisted with data analysis, writing the manuscript and editing the manuscript.

Manuscript Information

Galip Yiyen, Robert A. Walker

Status of the Manuscript:

_x_ Prepared for submission to a peer-reviewed journal

____ Officially Submitted to a peer-reviewed journal

____ Accepted by a peer-reviewed journal

____ Published by a peer-reviewed journal

CHAPTER FOUR

NONLINEAR OPTICAL STUDIES OF WATER AT GYPSUM/AIR AND GYPSUM/AQUEOUS INTERFACES

Introduction

Mineral dissolution is a deceptively complex chemical process that depends on solvation dynamics, lattice energies, impurities, morphology, and transport with all of these contributions complicated by the chemical asymmetry intrinsic to any solid-liquid interface[113-119]. Mineral dissolution, however, is a critical part of rare earth element extraction technologies as well as the primary contribution to groundwater solute composition, including salinity. Kinetic studies show that dissolution does not always follow a steady state reaction rate,[115, 118, 120, 121] and irregularities in dissolution kinetics have become the focus of models attempting to characterize the process from a molecular level perspective[122].

Dove and Czank reported isostructural sulfate minerals dissolved at rates inversely proportional to the ionic radius of the cation in the mineral[123]. These authors proposed that smaller ions on the mineral surface experienced greater stabilization by the adjacent solvent due to greater charge density leading to a faster dissolution rate. Stack et al. suggested that, despite conventional wisdom, dissolution and crystal growth should not be treated simply with a reversible mechanism and that dissolution mechanisms should be considered in the context of rare or non-stochastic events[124]. Related work modeled the evolution of complexes between barium and sulfate during detachment events of barium ions and suggested that the hydration sphere at the interface plays an important role in dissolution processes[125]. These molecular

dynamics studies showed that detachment of a barium ion (from a kink site) occurs through four different transition states, where the orientations of sulfate ions are clearly shown to be affected during the detachment. Regardless of the models used and the techniques employed, describing dissolution (and the opposite process, crystallization) hinges upon understanding the chemistry occurring at the mineral-aqueous interface. Models are suggestive, but predictions must then be validated by experimental observation. To begin addressing mineral surface structure in the presence of water, studies reported in this work clarify the structure and organization of water at (010) gypsum ($CaSO_4 \cdot 2H_2O$)-water and gypsum-air interfaces.

Gypsum dissolution is a particularly important reaction because of this mineral's abundance in the earth's crust[23] and its use as a building material, a fertilizing agent, and a food additive[126, 127]. Gypsum has even been proposed as a water source for microorganisms in exceptionally arid environments.[128] Gypsum dissolution kinetics have enormous practical relevance given this material's importance as a building material[129, 130]. In this context, pressure and temperature are considered the most important variables affecting gypsum stability when exposed to water, and gypsum debris as construction waste has significant impact in hydrogen sulfide gas production in urban areas, which is highly toxic[131, 132].

Gypsum dissolution as a function of aqueous phase pH and ionic strength has been studied in a controlled laboratory setting to gain more understanding of its adverse effects of gypsum dissolution on environmental water quality[20, 133]. For example, gypsum dissolution is responsible for high ground and surface water salinity in landscapes dominated by evaporite karst structures such as those commonly found in the Rocky Mountain West. These adverse effects are even more pronounced in the areas where the local overburden has been disrupted

from open air coal mining activity[21]. While many gypsum dissolution studies have focused on bulk gypsum dissolution rates, surprisingly little is known about water behavior at the gypsum-aqueous and gypsum-air interfaces.

Molecular level insight about water at gypsum and its derivative surfaces has come, in part, from X-ray and AFM studies. While studying bassanite ($CaSO_4 \cdot 0.5\ H_2O$) nanowhiskers having high aspect ratios, Hou et. al.[134] reported that Mg^{2+} ions selectively adsorb on the negatively charged, sulfate dominated facets. The authors concluded from spatially resolved XPS data that Mg^{2+} adsorbates promoted growth of the 1-dimensional structures having aspect ratios approaching 400. Another study used DFT and *ab initio* molecular dynamics (AIMD) to examine Cd^{2+} adsorption on natural gypsum surfaces characterize how structural defects in the gypsum affected this process. The authors reported that Ca^{2+} vacancies promote Cd^{2+} adsorption, while SO_4^{2-} vacancies inhibit the adsorption[135].

Using data from AFM studies from both gypsum-air and gypsum-solution interfaces, Finot *et al.* noted that different gypsum surfaces demonstrated different affinities for water[136, 137]. These authors separated the forces between two gypsum surfaces into van der Waals, electrostatic, and capillary contributions. Data suggested that the (010) gypsum surface's electrostatic properties were dominated by structural water molecules that – even in solution – created a net surface dipole and corresponding repulsion between two adjacent surfaces[137]. Capillary attraction between two gypsum surfaces separated by air (at 35% relative humidity (RH)) was attributed to extended sample flatness and this attraction was believed to outweigh attractive van der Waals forces. These findings suggested that formation of hydrogen bonding

between water integrated into the crystal surface structure and water molecules physisorbed to the (010) surface happens readily at RH $\geq$ 30%.

According to results from a more recent 3D-AFM study, this surface bound 'crystalline water' should be considered a structural element of the gypsum itself and the AFM experiments were sensitive to the first hydration layer on top of the gypsum surface[138]. Complementary simulations showed only one crystalline water molecule per unit cell while the adjacent two hydration layers were each comprised of two water molecules per unit cell. Furthermore, experiments suggested that this surface bound crystalline water remains intact even when the gypsum surface is in contact with water. These results have important implications for chemistry occurring at the gypsum-aqueous interface with regards to bulk-surface exchange rates, solvation dynamics and general reactivity at this ubiquitous mineral/aqueous interface[139].

While AFM is a powerful tool for studying overall water properties and behavior at gypsum surfaces, this technique can only identify whether water is present and, if so, where. Simulations can suggest relative orientations and the force curves resulting from AFM studies can be used to infer specific molecular/material interactions, but conclusions are necessarily indirect. Vibrational sum frequency generation (VSFG) is a surface specific, second order nonlinear optical technique capable of measuring vibrational spectra of adsorbed surface species. From these data comes information that reports directly on functional group orientation and intermolecular interactions.

The only report of VSFG being used to study of gypsum surface chemistry was reported recently by Santos, *et al.*.[140] Experiments were carried out in a room temperature nitrogen environment with controlled water exposure. Gypsum's intrinsic in-plane surface anisotropy

resulted in a strong VSFG intensity dependence on the crystal's rotational orientation relative to the laser propagation direction. Experimental VSFG results in this study were accompanied by findings from AIMD simulations that reported each structural water molecule orients differently at a freshly cleaved (010) surface under nitrogen atmosphere. Santos' study suggested that approximately 25% of the OH groups should be considered 'dangling' or without a hydrogen bonding partner while 75% of the crystalline water -OH groups are H-bonded under 0% RH. Interestingly, the authors used the results from AIMD simulations to assign features in their spectra to uncoupled -OH oscillators rather than the traditional symmetric and antisymmetric stretch normal modes. Increasing the RH to 50% (in N_2) created a full monolayer of water molecules and a corresponding loss of overall spectral intensity.

Discoveries made by Santos, *et al.* created a very detailed description of the fundamental interactions occurring between individual water molecules and a pristine gypsum surface structure. In environmental settings, however, gypsum is constantly cycled between bulk water (or high humidity) and more arid conditions. Questions about how this cycling affects water structure and gypsum surface structure must be considered when addressing gypsum surface chemistry, including dissolution and recrystallization mechanisms. In the studies described below, VSFG is used to probe water structure at the gypsum interface before, during, and after immersion in liquid water. Our results support AFM findings described above that suggest surface-bound crystalline water remains a part of the gypsum surface structure, even when in contact with a bulk aqueous phase. Similar to claims made by Santos. *et al.* our results also imply that the -OH bonds in one population of surface bound water are decoupled from each other with one -OH bond directed in the plane of the gypsum surface and interacting strongly with surface

sulfate groups. A second type of gypsum-bound surface water samples a more symmetric environment and preserves its normal mode structure. Physisorbed water is also observable albeit with much weaker intensity, implying rapid exchange with the ambient atmosphere and/or a higher degree of disorder.

Methods

Sample Preparation for VSFG Measurements

Gypsum samples are purchased from Kidz Rocks, Inc. Outer layers are cleaved with a sharp razor before VSFG measurements to access clean surfaces. Large gypsum layers were broken into smaller pieces with dimensions approximately 1 cm x 3 cm x 0.05 cm and placed in a sample cell allowing surface investigation when a solid piece is in contact with the liquid of interest (Figure 4.1). The sample assembly is made of Teflon and was rinsed repeatedly with Millipore water (18.2 MΩ·cm resistivity) and methanol before being immersed into 50/50 nitric acid/sulfuric acid solution. After remaining in the acid bath for an hour, the cell was again rinsed with Millipore water before introducing any liquid for measurement.

Spectra were collected from gypsum/air interface at first, then the sample was introduced to the sample chamber by using borosilicate glass pipette and spectra from gypsum/water (or gypsum/D_2O) were collected. Finally, water (or D_2O) was removed from the chamber and VSFG signals were collected from gypsum/air interface again (Figure 4.1).

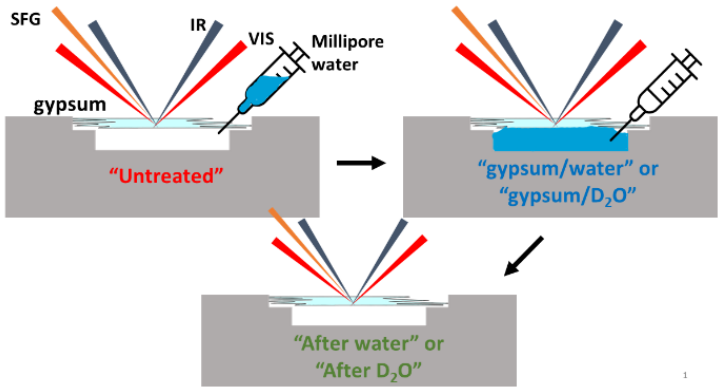

Figure 4.1. Schematic of sequence of VSFG measurements taken from different interfaces

Vibrational Sum Frequency Generation Spectroscopy

Vibrational sum frequency generation (VSFG) spectroscopy is a second order non-linear spectroscopy technique that provides information about molecular vibrational structure at surfaces. In order to be observed in a VSFG spectrum, a vibrational mode must be both Raman and IR active and must show net polar ordering induced by local anisotropy. These conditions are met at the surface, where asymmetry is intrinsic along the surface normal as well as in bulk materials lacking inversion symmetry. Disordered molecules at the surfaces, molecules in bulk solution and in bulk materials where no net polar ordering is present will be VSFG silent.

VSF signals are not only sensitive to the vibrational frequency of the functional group, but also to the directions of IR transition dipole moments created by the vibrational motion. Input polarizations of IR and VIS are controlled via λ/2 waveplates and a specific VSF polarization is selected using a third λ/2 waveplate and a polarizer. Data presented below show spectra acquired in two polarization combinations: $S_{SF}S_{IR}P_{vis}$ and $S_{SF}P_{IR}S_{vis}$. The $S_{SF}S_{IR}P_{vis}$ combination samples a single element of the $\chi^{(2)}$ tensor, $\chi^{(2)}_{xxz}$, and is sensitive to those vibrations with transition moments aligned predominantly along the surface normal or out of plane. Similarly the

$S_{SF}P_{IR}S_{vis}$ combination samples only $\chi^{(2)}_{xzx}$, and is probes those vibrations aligned in the plane of the surface. The $P_{SF}P_{vis}P_{IR}$ combination and probes all non-zero elements of the $\chi^{(2)}$ tensor with their relative amplitudes modulated by IR, visible, and SF angles of incidence. Detailed information about VSFG theory can be found in numerous reviews[71, 141-143].

The assembly used for measurements presented in this study has been described[35, 73, 74, 144]. Briefly, an output beam (3.2 W, 1 KHz, 85 fs) from an amplified Ti:sapphire laser (Coherent Libra HE) is split into two by an 80/20 beam splitter. 80% of the intensity is used to pump Coherent OPerA Solo to produce IR beams at 3 different parts in the -OH stretching frequency region. Beams were centered around ~3280 nm, ~3130 nm and ~2990 nm. Remaining 20% of the 800 nm output is spectrally narrowed with a pulse shaper to have spectral resolution around 15 cm^{-1}. Produced VSF signal is focused into a monochromator and collected with a 1340 x 100 pixel CCD.

VSFG signals presented in this study come from vibrations of water molecules at the bottom surface – referencing the sample position shown in Figure 4.1 – of the gypsum piece. To minimize the loss of IR intensity upon absorption by structural water molecules, thin (~250-300 μm) gypsum pieces were used. Before gypsum measurements, reference measurements were taken from the surface of a gold wafer to determine the spot where IR and visible beams spatially overlap. Then, a gypsum piece with a comparable thickness was placed to same sample chamber, and after careful alignment, relatively weak SFG signals were detected. The height of the sample stage was then adjusted so that the beam overlap spot was optimized on the bottom surface of the gypsum sample. Signal intensities were continuously monitored by correcting the optics along the path followed by the SF response. This final monitoring of signal intensity further ensured

that collected SF signals were dominated by the bottom surface molecules, rather than the top surface. After the optimum signal was achieved at the beginning of the measurements, neither the alignment, nor the sample position was changed throughout rest of the measurements.

FTIR Analysis

Gypsum pellets were prepared using 5 mg of commercial gypsum powder (NilocG, 97%) or 5 to 7 mg of the gypsum crystal pulverized with a mortar and pestle. In each case the gypsum samples were mixed with ~100 mg NaCl (Sigma-Aldrich, ACS Reagent, ≥ 99.0%) as a diluent. Samples were pressed using a 13 mm pellet die and applying approximately 5000 tons of pressure. Samples were taken immediately to a Bruker VERTEX-70 FTIR spectrometer. Background measurements were taken using 100 mg NaCl pellets pressed in the absence of any gypsum. Spectra were collected between 400 and 7000 cm^{-1} and represented an average of 32 individual scans having 1 cm^{-1} resolution. Additional FTIR measurements were made with a thin gypsum slab cleaved from the original crystal stock. These samples were typically between 10-20 μm thick with uncertainty limited by caliper accuracy.

Raman Analysis

Raman spectra from a single crystal gypsum piece and gypsum powder were collected by HORIBA LabRAM HR Evolution Raman microscope. A 532 nm laser was used for analysis and the laser output was set to ~225 mW for these single crystal measurements. Spectra represented the average of 6 accumulations each with an acquisition time of 20 seconds. For the powder measurements, the laser output was set to 450 mW and the spectrum resulted from 3 x 10 second accumulations. Raman intensity in single crystal spectrum needed to be multiplied with a factor of 60 for direct comparison with powder spectrum.

Results and Discussion

FTIR and Raman of Powder and Single Crystal Samples

FTIR and Raman data from the gypsum powder (pressed into a pellet) and a thin slab of single crystal gypsum are shown in Figure 4.2. In both the IR and Raman spectra, features from the powder and single crystal samples show intensity from overlapping bands between 3100 cm^{-1} and 3700 cm^{-1} but similarities between the two sample types end there.

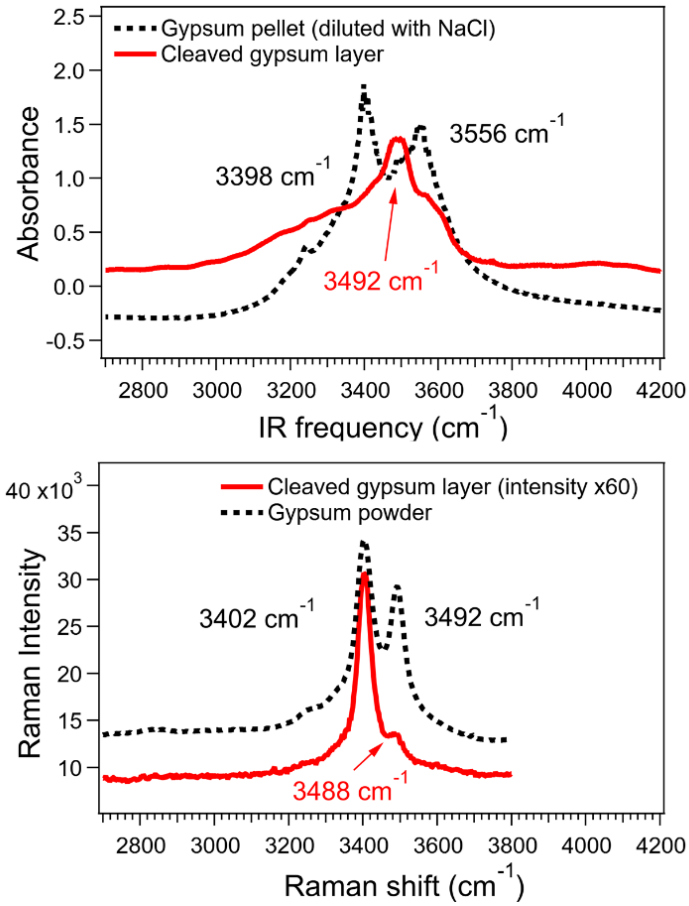

Figure 4.2. FTIR absorption spectra taken from a gypsum pellet pressed by powder and NaCl mixture and a thin layer of cleaved gypsum from the same slab used for VSFG measurements (top); and Raman spectra collected from gypsum powder and from a thin layer of cleaved gypsum (bottom)

The IR spectrum from the gypsum pellet shows a small feature at 3220 cm^{-1} and then two larger distinct features centered at 3398 cm^{-1} and 3556 cm^{-1}. The single crystal IR spectrum, in contrast shows broad, featureless intensity except for a single well-defined peak centered at 3492 cm^{-1}. Based on literature reports, the small feature at 3220 cm^{-1} from the pressed pellet is assigned to a Fermi resonance coupling between an H_2O bending overtone and the H_2O symmetric stretch.[145, 146] The two larger features at 3398 cm^{-1} and 3556 cm^{-1} are assigned to the symmetric and antisymmetric stretches of water within the lattice, respectively.[31] The feature at 3492 cm^{-1} observed in the slab sample is assigned to an antisymmetric stretch of a different water population in the bulk material.[147, 148] Noticeable differences between the peak shapes in FTIR spectra from the pellet and single crystal gypsum are quite similar with the observations reported in Knittle et al.'s study. The impact of pressure changes on vibrational frequencies were investigated in their study and findings indicated the disappearance of factor-group splitting at high pressures, resulting in combination of symmetric and antisymmetric stretching peaks[31]. In Figure 4.2, a striking difference between the two absorption spectra are the relative intensity patterns and different bands that appear.

Differences between the pressed pellet and slab are also evident in the Raman data. Raman spectra collected from both types of gypsum samples show a strong peak at 3402 cm^{-1} assigned to the water symmetric stretch. A second feature in the pressed pellet spectrum appears at 3492 cm^{-1} and is again assigned to the water antisymmetric stretch.[31, 147, 148] In contrast, the Raman spectrum acquired from the slab shows the one dominant feature at 3402 cm^{-1} but the higher frequency feature observed in the pellet appears only as a weak high frequency shoulder (at 3488 cm^{-1}) in the slab sample.

The features in all four spectra shown in Figure 4.2 can be assigned based on previous reports. [145, 146,31, 147, 148] Differences between spectra from the pressed pellets and the slab samples, however, warrant mention. We note that the pressed powder samples will necessarily have a larger fraction of surface waters contributing than the slab sample based on simple area-to-volume considerations. Also, for a vibrational transition to be sum frequency active, it must be both IR and Raman symmetry allowed. This consideration suggests that that a strong SFG response might be expected near 3400 cm^{-1}. If the pellet sample reflects stronger contributions from structural gypsum water molecules at the gypsum surface, we would not expect strong SFG responses at 3492 cm^{-1} because while this feature is strong in the Raman pellet spectrum, it is absent in the IR pellet spectrum, and is evident only in the IR slab sample spectrum where bulk gypsum water is expected to contribute. Similarly, the strong 3556 cm^{-1} feature observed in the IR pellet spectrum is absent in the Raman pellet spectrum. Taken together, while the vibrational features observe in Figure 4.2 can be assigned based on previous reports, the data together predict that VSFG spectra should show only a single strong feature (near 3400 cm^{-1}).

VSFG Spectra from Gypsum/Air and Gypsum/Water Interfaces.

Gypsum samples measuring approximately 1 cm x 3 cm x 0.05 cm were placed onto the sample holder. VSFG spectra were collected from the freshly cleaved gypsum surface (labeled as 'Untreated'), as well as from the gypsum surface in contact with Millipore water or D_2O (labeled as 'gypsum/aqueous' or 'gypsum/D_2O', respectively). Lastly, spectra were collected from the surface after the water or D_2O had been removed from the chamber and allowed to air-dry for 30 minutes (labeled as 'after water' or 'after D_2O'). Spectra from each of these conditions (before/during/after water) were acquired under $S_{sum}S_{vis}P_{IR}$ and $S_{sum}P_{vis}S_{IR}$ polarization

conditions sampling out-of-plane and in-plane vibrations, respectively. All VSFG spectra are shown in Figure 4.3.

Two easily distinguishable VSF bands were observed: one at 3020 cm^{-1} that is dominant in the SPS polarization combination sampling in-plane vibrations and one ~ 3415 cm^{-1} that is dominant in the SSP spectra signifying vibrational resonance with a transition dipole directed along the surface normal. The 3020 cm^{-1} feature did not shift following exposure to and removal of liquid D_2O or H_2O. The 3415 cm^{-1} peak, however, showed a small but reproducible shift from 3415 cm^{-1} to 3411 cm^{-1} following exposure to H_2O. The spectra shown in Figure 4.3 are plotted on a normalized scale but we note here that SPS spectra were typically 2-3 times stronger in absolute magnitude than the SSP spectra.

SSP spectra also show weaker vibrational bands between ~3100 and 3300 cm^{-1}. We believe these vibrational bands arise from physisorbed water. The basis for this assignment is discussed below.

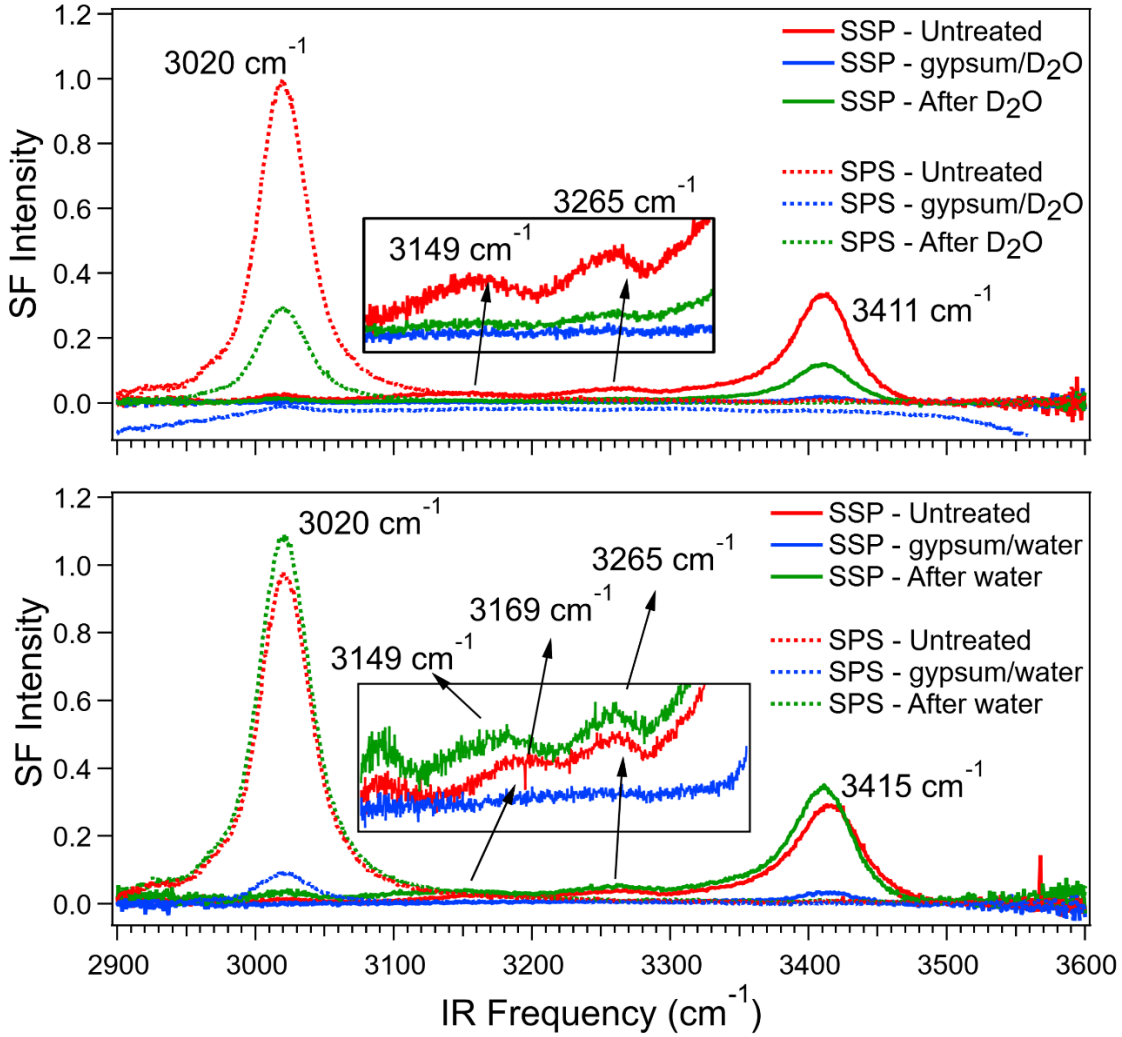

Figure 4.3. VSFG spectra collected from gypsum/air interface before any interaction with D_2O (top) or water (bottom); from gypsum/D_2O or gypsum/water and from gypsum/air after the D_2O or water was removed from sample chamber.

Based on IR and Raman data from gypsum samples cited above, the 3415 cm^{-1} is assigned to a symmetric stretch of H_2O having its C_2 axis directed along the surface normal. This vibration is both IR and Raman active based on spectra shown in Figure 4.2. Water molecules responsible for this feature will have well defined structure and organization as evidenced by the relatively narrow linewidth (~35 cm^{-1} FWHM). For comparison, VSF spectra of water at liquid interfaces typically consist of two features – one of which is centered near 3400 cm^{-1} but with a

linewidth approaching 100 cm^{-1} [149]. Two points about the 3415 cm^{-1} are worth noting. First, surface water molecules aligned with their symmetry axes along the surface normal would create a net surface dipole that would explain the repulsive forces observed between two gypsum surfaces reported by AFM measurements[137]. Second, this assignment presumes that the water molecules responsible for the 3415 cm^{-1} band retain a normal mode structure, meaning that the two -OH bonds comprising these water molecules remain sufficiently coupled. While the symmetric stretching can clearly be seen in these spectra, the accompanying antisymmetric stretching signal is not observed. The absence of the antisymmetric stretch might be explained by either static in-plane isotropy of these water molecules or by rapid rotation of these water molecules about their C_2 axes. Rapid rotation would dephase any in-plane polarization leading to a vanishing VSF response, but the out-of-plane nonlinear polarization would be retained resulting in a strong symmetric stretch and no observable intensity in the antisymmetric stretch.

The feature centered at 3020 cm^{-1} is not so easily assigned. Such a low energy -OH vibrational frequencies have been observed in water cluster studies[150, 151] and from -OH functional groups in larger molecules[152-156]. Buck and Huisken reported a vibrational frequency of 3065 cm^{-1} for water molecules involved in a donor-acceptor-acceptor (or DAA) configuration with the 3065 cm^{-1} vibration belonging to the O–H bond that is donating a hydrogen bond to its neighbor. Supercooled water at ambient pressure was reported to give rise to a Raman active vibrational resonance at signal at 3041 cm^{-1} that Qiang also assigned as the -OH stretch of DAA-water[151]. Furthermore, several IR studies of water in diaspore minerals have reported -OH stretching near 2950 cm^{-1} [157], consistent with a decoupled O–H bond in water that is strongly hydrogen bonded to a neighbor.

Considering these previously studies, we assign 3020 cm^{-1} band to a decoupled, in-plane O–H bond that is strongly interacting with sulfate groups on the gypsum surface. Below, we propose that the population of water molecules contributing to this feature corresponds to the crystalline water that remains intact on the gypsum surface even during exposure to water. This picture predicts that the second O–H bond of these water molecules should be directed along the surface normal without any hydrogen bonding opportunities. Such a vibration would be expected to have a vibrational frequency close to 3700 cm^{-1} based on previous reports. Unfortunately for the VSFG assembly used in these studies, the highest attainable frequency is approximately 3600 cm^{-1}. We note that this assignment and interpretation of the 3020 cm^{-1} feature is consistent with the original VSFG report by Santos *et al*.[140]

Finally, we note that SSP spectra show two wide and relatively weak signals observed at ~3160 cm^{-1} and 3265 cm^{-1}. Weak signals can be due to low surface coverage, anisotropic distribution, and/or rapid motion that dephases coherent polarization induced by ω_{IR}. Given the relatively low frequencies of these observed VSF signals, the features had been assigned to 'ice-like' or strongly coordinated water based on VSF studies of water/vapor interfaces reported previously[143].

Both Santos and Finot reported increased water adsorption upon RH change from 25% to 50%[137, 140] with AFM results showing a steady increase in the amount of water between the gypsum surface and the AFM tip. Additionally, Santos et al. proposed that at 50% RH, adsorbed water had created a full monolayer on the gypsum surface.[140] VSFG measurements presented in this study were conducted under 25 ± 10% RH conditions. Both AFM and VSFG results indicated a dynamic adsorption/desorption equilibrium of water molecules on the gypsum

surface. This situation would lead to a physisorbed water structure that when time averaged would appear more disorganized and show only weak VSF signal.

Hydrogen Bonding Structure

To interpret the data shown in Figure 4.3, we considered the different H-bonding environments that exist at the (010) gypsum surface using results from previous simulation studies. Dispersion corrected DFT calculations modeled Cd^{2+} adsorption on gypsum surfaces containing specific types of vacancies (Ca^{2+}, SO_4^{2-} and H_2O) in a unit structure[135]. These calculations predicted that Ca^{2+} vacancies promote Cd^{2+} adsorption, while sulfate vacancies play an inhibiting role. Crystal water vacancies had very little effect on Cd^{2+} adsorption. The mechanism responsible for the sulfate vacancy's inhibiting effect was found to be a sulfate vacancy-induced change in the position of water's hydrogen atoms. Results showed that sulfate vacancies led to an upward relaxation of water molecule hydrogens at the surface hindering Cd^{2+} adsorption through both steric and electrostatic effects. These results reported by Baolin et al. are helpful to determine the hydrogen bonding environment the -OH bond (3020 cm-1) engages into. Baolin's study shows that, at least one population of structural water molecules at the surface engages into H-bonding with sulfate oxygens, rather than the other water molecules.

Moreover, in the calculations performed by Santos, *et al.*, three out of four different -OH signals were engaged in directional hydrogen bonding, and of these three, two were reported as hydrogen bonds formed with sulfate oxygens, rather than neighboring water oxygens. These calculated vibrational frequencies were reported at frequencies lower than what was observed by Santos, *et al.* experimentally. With the results from these simulations and considering the predicted strong impact of sulfate on water molecule alignment[135], we propose that the 3020 cm^{-1}

feature in Figure 4.3 arises from individual (or decoupled) O—H bonds in water molecules donating strong hydrogen bonds to adjacent sulfates. In contrast, based on previous IR and Raman measurements, the peak observed at 3411 cm^{-1} (or 3415 cm^{-1}) is assigned to the symmetric stretching vibration originating from water donating both of its hydrogens to two different neighboring water molecules. This assignment is also supported by simulated structures. Representations of these structures are shown schematically in Figure 4.4

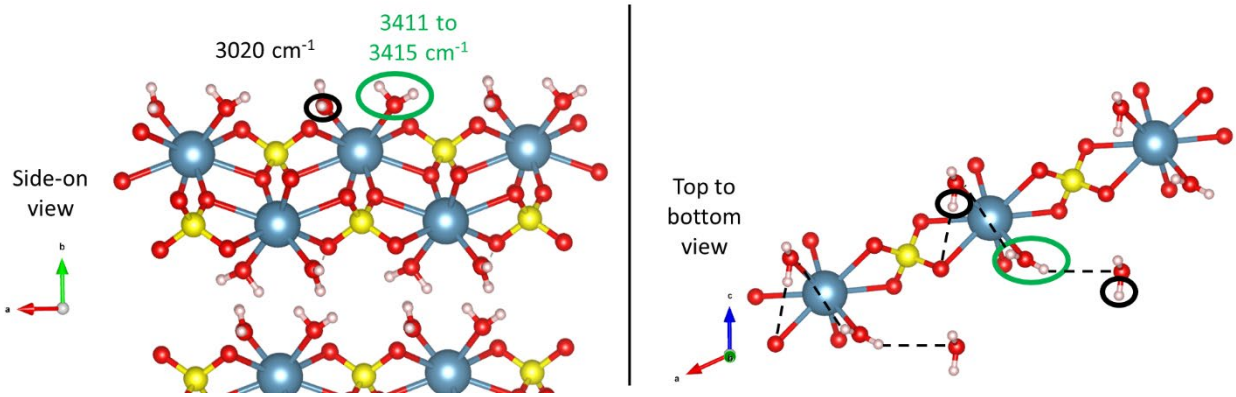

Figure 4.4. Proposed structure of water molecules drawn on the gypsum crystal structure. The two structural water species believed to be responsible for the 3020 cm-1 and 3415 cm-1 vibrational bands are circled in black and green, respectively. The bulk crystal structure was retrieved from 'Crystallography Open Database'[158] and was reported by Comodi et. al[159].

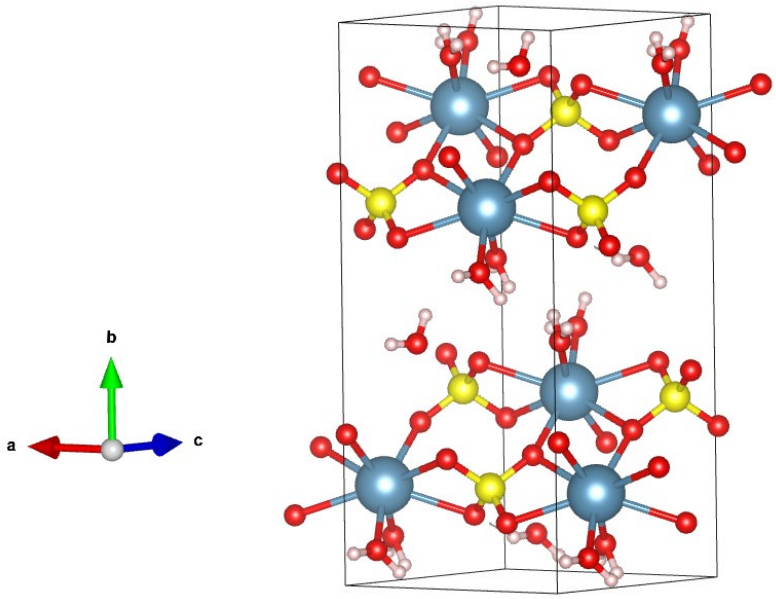

Figure 4.5. Crystal structure of gypsum reported by Comodi et al.[159] with the addition of proposed water structures in this study.

The structural water that comprises part of the gypsum surface shows two distinct populations. One has a water -OH bond directed towards a sulfate oxygen atom (circled in black in Figure 4.4) and the other type of water has both -OH bonds generally directed away from the surface (circled in green). These structures are consistent with the assignments described above where the decoupled -OH stretch at 3020 cm^{-1} lies predominantly in the surface plane and is sampled in an $S_{sum}P_{vis}S_{IR}$ geometry while the water having its -OH bonds pointed away from the surface is expected to have normal-mode vibrational structure and the symmetric stretch would be observed most readily in $S_{sum}S_{vis}P_{IR}$ spectra.

Analysis of structural changes on gypsum surface

In this section, we discuss how surface water structure changes after gypsum is brought into contact with D_2O vs. H_2O. Figure 4.3 (top) shows VSFG spectra collected from a gypsum surface before, during and after contact with D_2O. The 'after-contact' spectrum was recorded

20 minutes after the D_2O was removed and the gypsum surface was allowed to air-dry. The effects of exposure to D_2O are apparent in the relative peak intensity changes. Both the 3020 cm^{-1} and 3415 cm^{-1} features drop in intensity by ~75% after exposure to D_2O. Although weak to begin with, vibrational bands assigned to physisorbed water at 3149 cm^{-1} and 3265 cm^{-1} also lose intensity by a larger fraction. We note that when D_2O is present, the VSFG spectra from the solid/liquid interface show no intensity in the -OH stretching region. This last result is additional evidence that observed features are due to water molecules at the surface rather than structural molecules from within the gypsum slab interior.

Considering the humidity in our lab (~25%) and previous studies in the literature reporting a 20-25% RH as a threshold of water vapor adsorption on gypsum, our findings and interpretation on surface structure are consistent with findings reported earlier. Additionally, Supporting Information from Santos, *et al.* reports that D_2O adsorption under a nitrogen atmosphere *decreased* structural water VSF signal intensities. Intensity decreases induced by D_2O adsorption cannot easily be quantified from the Santos, *et al.* study due to relatively low signal to noise (S/N) in the 3000-3600 cm^{-1} region, but signal intensity at 3680 cm^{-1} assigned to the free –OH decreased by approximately 90%. Furthermore, intensity of this signal recovered back to ~25% of its initial intensity after the surface was exposed to laboratory air. The Santos *et al*. report did not note how long the gypsum surface was exposed to air after being removed from the climate controlled N_2/D_2O chamber nor did the authors note RH in the room, but the reported peak intensity losses and recoveries – during and after D_2O exposure – agree qualitatively with the observations presented in Figure 4.3.

In contrast to the results during and following exposure to D_2O, the gypsum/H_2O interface *does* show vibrational structure at the same two frequencies – 3020 cm^{-1} and ~3415 cm^{-1} under their typical polarization conditions– albeit very weakly. Intensity loss in these vibrational signals are attributed to decrease in net polar ordering at the surface; though, overall decrease in SF intensity due to the similar refractive indices of gypsum and water at 3.33 μm of 1.52 [160] and 1.33 [161], respectively, predicts that ~95% of the VSF signal will be transmitted into the water. Following removal of the H_2O and 30 minutes of exposure to the ambient atmosphere, these vibrational bands recover their full intensity. In fact, the relative intensities of these features appear to *increase* slightly by ~10%. Similar behavior is observed for the phsyisorbed water at ~3160 cm^{-1} and 3265 cm^{-1}. A second observation is that following exposure to water the 3415 cm^{-1} shows a small but measurable shift to 3411 cm^{-1}. Such a shift would be expected if more water at the surface led to stronger local hydrogen bonding.

Taken together, these findings support the notion that structural water at the gypsum surface is largely 'locked' into the surface structure and does not easily exchange with the bulk liquid. Such a picture is consistent with conclusions from the AFM studies of Finot and Songen[138]. Vibrational spectra also agree with predictions from calculated crystal surface structures.

Conclusions

In this work, we have investigated the structure of crystal (or structural) water on gypsum (010) surface by using VSFG spectroscopy. FTIR measurements were also used to gain insight for peak assignments. Results showed that two water molecules in a unit cell yield different vibrational signals. -OH vibration in one water molecule decouples and creates a low frequency

(3020 cm-1) VSF signal in plane, -possibly- leaving a dangling -OH along the surface normal. Other water molecule creates a VSF signal around 3411 to 3415 cm-1 along the surface normal, which is assigned to symmetric stretching of H_2O. Additionally, two broad and relatively weaker peaks around 3160 cm-1 and 3265 cm-1 peaks are assigned to vibrations of adsorbed water molecules from air in ambient conditions.

VSFG spectra collected from gypsum/water and gypsum/D_2O interface point out to some degree of decrease in ordering of molecular structure, though, it is more pronounced at the gypsum/D_2O interface. Complete and incomplete structural recoveries upon removing water and D_2O, respectively, was also presented via VSFG measurements. The quick and complete recovery is an indicative of tightly bound crystal water molecules on gypsum surface.

CHAPTER FIVE

INVESTIGATING SPONTANEOUS ADSORPTION OF SODIUM DODECYL SULFATE ON GYPSUM SURFACE BY USING NONLINEAR OPTICAL SPECTROSCOPY

Contributions of Authors and Co-Authors

Manuscript in Chapter 5

Author: Galip Yiyen

Contributions: Collected and analyzed experimental data. Assisted with writing and editing the manuscript

Co-Author: Robert A. Walker

Contributions: Assisted with data analysis, writing the manuscript and editing the manuscript.

Manuscript Information

Galip Yiyen, Robert A. Walker

Status of the Manuscript:

_x_ Prepared for submission to a peer-reviewed journal

____ Officially Submitted to a peer-reviewed journal

____ Accepted by a peer-reviewed journal

____ Published by a peer-reviewed journal

CHAPTER FIVE

INVESTIGATING SPONTANEOUS ADSORPTION OF SODIUM DODECYL SULFATE ON GYPSUM SURFACE BY USING NONLINEAR OPTICAL SPECTROSCOPY

Introduction

Chapter 2 investigated surfactant organization on gypsum surface treated with the anionic surfactant SDS and cationic surfactant DTAC. Vibrational sum frequency generation (VSFG) and EDX measurements confirmed that SDS surfactants covered the gypsum surface forming a conformal layer having long range order. Data showed that SDS molecules adopted an orientation with their alkyl chains lying parallel to the surface. In contrast, no net ordering was observed in the DTAC molecules deposited on gypsum surfaces. VSF measurements showed no evidence of surface induced organization and EDX images suggested that the DTAC molecules aggregated into small, disordered islands.

While the findings described in Chapter 2 suggest mechanisms of how surfactants interact with this mineral surface, the question of whether SDS surfactants in aqueous solution would adsorb to the gypsum surface spontaneously remained unanswered. The studies described in this chapter tackle this question by examining vibrational structure at the gypsum/aqueous interface where the aqueous solution contains 4 mM SDS. While VSF spectra showed no sign of adsorption while the gypsum was in contact with the solution, vibrational features began to appear and temporally evolve *after* the solution was removed and the gypsum surface allowed to dry. Given the geometry of the experiment, these findings imply that SDS *does* adsorb spontaneously to the gypsum/aqueous interface and the SDS reorganizes on the gypsum surface

as it starts to dry. These findings carry implications for the chemistry occurring at soil/water interfaces as the soil cycles repeatedly between being fully hydrated and completely dry.

The sample preparation used in these studies was identical to the one that was used to study water structure at the gypsum/aqueous interfaces described in Chapter 4: a thin gypsum slab was placed on top of a Teflon sample chamber that was then filled with water or – in this case – a solution containing SDS. The system was allowed to equilibrate and then the solution was removed. Surface specific VSF measurements were made at each stage of this process to assess vibrational structure in the -CH_x stretching region (~2800 – 3050 cm^{-1}). Results were surprising and while additional work must be done before the reported phenomena are fully understood, the findings are significant enough to warrant their own chapter in this dissertation. In the remainder of this chapter, Section 5.2 presents the VSFG spectra collected from aqueous SDS/gypsum interface and assigns polarization dependent features observed. Section 5.3 presents the time-dependent VSFG spectra from gypsum surface collected at different times *after* the SDS solution was removed from sample chamber and the surface allowed to dry. Preliminary interpretation of these data and tentative conclusions are presented in Section 5.4.

Gypsum/SDS Aqueous VSFG Studies

SDS adsorption upon evaporation of water on gypsum surface was studied and found that the carbon chains are oriented parallel to the surface plane, with $C2_v$ axes of CH_2 groups also parallel to the surface, at the end of 2 hours period. In the current studies, our goal is to determine if SDS will adsorb to this interface spontaneously from aqueous solution and, if so, determine how the adsorbed surfactants organize. Figure 5.2 shows VSFG spectra collected from the gypsum surface before being exposed to the SDS containing solution; from the

gypsum/aqueous interface 20 minutes after the surface has come into contact with the solution; and from gypsum surface 25 minutes after the solution was removed.

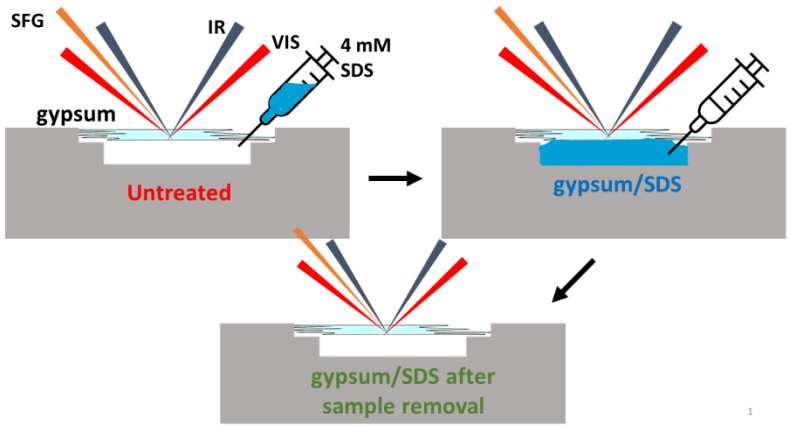

Figure 5.1. Preparation of untreated and SDS treated gypsum surfaces for VSFG measurements

Not surprisingly, no VSF signal in the -CH_x stretching region was observed from the gypsum surface prior to coming into contact with the aqueous solution. Furthermore, no VSF signal was observed from the gypsum/aqueous interface after 20 minutes of exposure. Given the relatively high 4 mM SDS concentration and previous literature reports, this time was judged to be long enough for the system to reach equilibrium[162]. The absence of any VSF signal could reflect three possible explanations:

a) *Adsorbed but disorganized SDS molecules:* If SDS monomers adsorbed to the gypsum/aqueous interface but showed no surface organization, the interface would, in effect, appear isotropic and contributions from the functional group hyperpolarizabilities to the overall $\chi^{(2)}$ tensor would cancel leading to no VSF signal.

b) *Adsorbed and organized SDS molecules; but significant transmitted -hence, the lost- SF signal intensity into the aqueous phase due to the closeness of refractive indices*: Given

the refractive indices of the two materials – gypsum (1.525) and water (1.331) – and the experimental geometry ($\Theta_{IR} = 40^{\circ}$; $\Theta_{vis} = 50^{\circ}$, both relative to the surface normal), a simple calculation shows that more than 90% of the VSF response might be lost to transmission. While -OH stretching vibrations *are* observed from the gypsum water interface (Chapter 4), those signals are attenuated significantly from those acquired from the gypsum/vapor interface. If SDS number density at this interface is sufficiently low, one might expect to not observe any signal.

c) *SDS does not adsorb spontaneously to the gypsum/aqueous interface*. The absence of any VSF signal might also indicate that SDS simply remains in solution rather than adsorbing to the gypsum/aqueous interface. While this situation would explain the lack of a VSF spectrum in the -CH_x stretching region from the gypsum/aqueous interface, results shown below suggest that this explanation is not applicable to these systems.

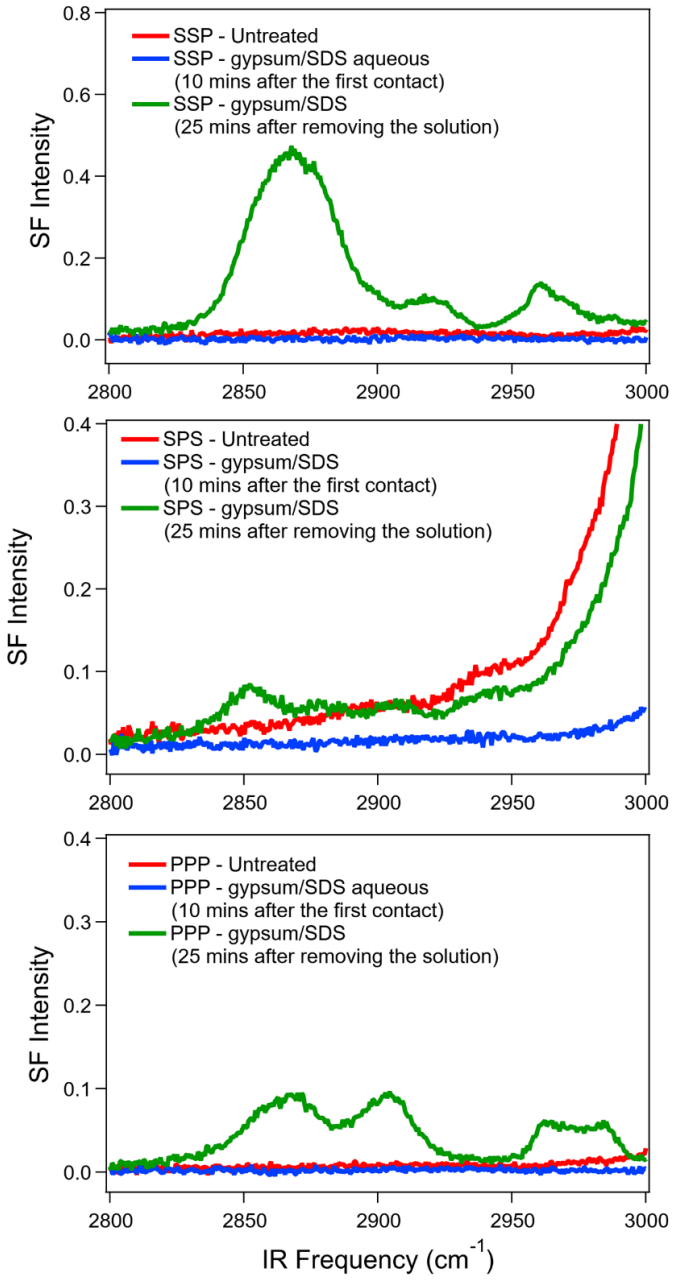

Figure 5.2. Polarization-dependent VSFG spectra collected from gypsum surfaces before (red), during (blue) and after (green) contact with the 4 mM SDS solutions. The 'during' spectra were acquired 20 minutes after initial formation of the solid/liquid interface and the 'after' spectra were acquired 25 minutes after the solution had been removed and the surface allowed to dry. The polarization combinations are $S_{sum}S_{vis}P_{IR}$ sampling out-of-plane vibrations (top); $S_{sum}P_{vis}S_{IR}$ sampling in-plane vibrations (middle); and $P_{sum}P_{vis}P_{IR}$ sampling all VSF allowed vibrations (bottom).

While the 'after' spectra in Figure 5.2 imply that SDS *did* adsorb to the gypsum/aqueous interface – discrediting 'Option c' above, questions remain about whether 'Option a' or 'Option b' more accurately reflects the structure of SDS at the solid/liquid interface. We note here that the features in the SSP and SPS spectra can be assigned to CH_2 symmetric stretching (2852 cm^{-1}), CH_3 symmetric stretching (2872 cm^{-1}), CH_2 antisymmetric stretching (2920 cm^{-1}) and a possible combination of CH_3 symmetric stretching Fermi resonance and CH_3 antisymmetric stretching (2950-2980 cm^{-1}). These data imply that SDS monomers adsorbed to the surface adopt an orientation that is largely upright along the surface normal albeit with *gauche* defects in the alkyl chains given the poorly resolved d^+ and r^+ features (CH_2 and CH_3 symmetric stretching, respectively) nominally at 2852 cm^{-1} and 2872 cm^{-1}.

Time-dependent Evolution of SDS Structure at the Gypsum/Air Interface

VSF spectra acquired from the gypsum/aqueous interface showed no vibrational features in the -CH_x stretching region. (Figure 5.2) This spectral region remained featureless 2 minutes after the solution had been removed from the sample chamber. However, a spectrum acquired 5 minutes after the sample removal showed a broad and weak signal centering at 2860 cm^{-1} under SSP polarization conditions (Figure 5.3). This result indicates the existence of ordered -CH_x vibrations on the surface. The specific frequency makes assigning the feature difficult. As noted above, alkyl chain -CH_2 and -CH_3 symmetric stretch transitions typically occur at 2852 cm^{-1} and 2872 cm^{-1} [74]. While these frequencies might vary by ±5 cm^{-1}, a single apparent feature at 2860 cm^{-1} might be best approximated as an envelope containing contributions from both of these normal mode vibrations. The most important conclusion to draw from this spectrum, however, is that the appearance of a feature in the -CH region *after* the solution has been removed is that

SDS does adsorb to the gypsum/aqueous interface and that the adsorbed SDS monomers likely remain disordered so long as sufficient water remains at the interface. As the water evaporates, the adsorbed SDS monomers begin to reorganize in a manner that creates net polar ordering.

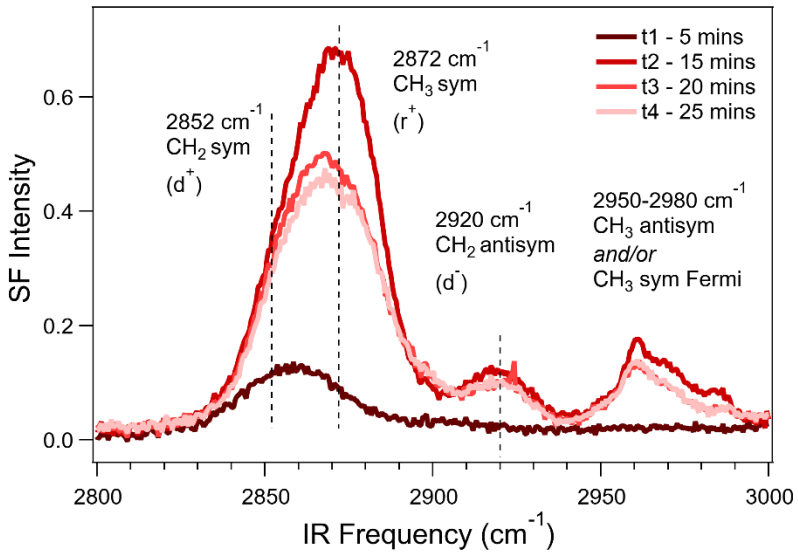

Figure 5.3. VSFG spectra collected from gypsum surface after the SDS solution was removed from the sample chamber. Shades of red represent the spectra collected 5, 15, 20 and 25 minutes after the sample removal.

As more time elapses, evidence of this reorganization becomes increasingly evident. In addition to the 5-minute spectrum shown in Figure 5.3, the figure also includes SSP spectra taken 15 minutes, 20 minutes and 25 minutes after the solution has been removed. Several observations stand out. First, spectra taken at later times show additional features at frequencies above 2900 cm^{-1}. These features are nominally assigned to the -CH_2 antisymmetric stretch (2920 cm^{-1}) and the -CH_3 antisymmetric stretch (2960 cm^{-1}). Second, the unresolved d^+/r^+ band first grows and then diminishes in intensity providing further evidence of continued surfactant reorganization at the surface. Finally, this unresolved d^+/r^+ band shifts to higher frequency and

shows more asymmetry implying conformational as well as orientational changes. These observations are discussed in more detail below.

Deducing Orientation Information of Molecules

Focusing on the broad, unresolved d^+/r^+ band in Figure 5.3, we fit this feature with two Gaussian profiles centered at 2852 cm^{-1} for the $-CH_2$ symmetric stretch and 2872 cm^{-1} for the $-CH_3$ symmetric stretch. The analysis also constrained the linewidth of these two profiles to 33 cm^{-1} FWHM for the $-CH_2$ symmetric stretch and 33 cm^{-1} FWHM for the $-CH_3$ symmetric stretch. Fitted Gaussian profiles are shown in Figure 5.4 and the results of fitting this band to the r^+ and d^+ transitions are reported in Table 5.1.

The r^+/d^+ intensity ratio in VSFG spectra has long been used as an indicator of acyl chain ordering in lipid film. If acyl chains are ordered and upright, VSFG experiments sample r^+ (with the methyl group pointing 'up') but not d^+ (with methylene groups having their $-CH_2$ planes aligned parallel to the surface). As a result, a large r^+/d^+ ratio indicates well-ordered chains having few gauche defects. A small ratio indicates a disordered monolayer where gauche defects break inversion symmetry about the C-C bonds and lead to some methylene groups having their local C_2 axes directed along the surface normal.

To deduce how the average orientations of adsorbed SDS molecules change in time, areas of the fitted peaks were compared. Results from the fitting analysis of '5 minute' spectrum are also included in Figure 5.4, although orientation information cannot be deduced from this spectrum due to several limitations. First, the feature itself is reasonably symmetric and the 2860 cm^{-1} band center lies right in between d^+ and r^+. As a result, the fitting parameters are not as robust or unique as one would like to make a quantitative comparison. Second, the feature's low

intensity adds higher uncertainty to the fitting parameters. These disclaimers notwithstanding, the r^+/d^+ ratio from the '5 minute' spectrum is 0.7, a result consistent with disordered, loosely packed lipid monolayers having average areas of ~30 $Å^2$ per alkyl chain. For context, an all-trans alkyl chain directed along the surface normal has an ~18 $Å^2$ cross sectional area.

The '15 minute' spectrum has significantly more intensity than the '5 minute' spectrum and the d^+/r^+ feature shows strong asymmetry towards higher frequency (implying that r^+ is contributing more to this SSP spectrum). Furthermore, an additional feature in the spectrum at 2920 cm^{-1}, which is assigned to CH_2 antisymmetric stretching, indicates that there is some degree of tilt with the chains (Figure 5.5).

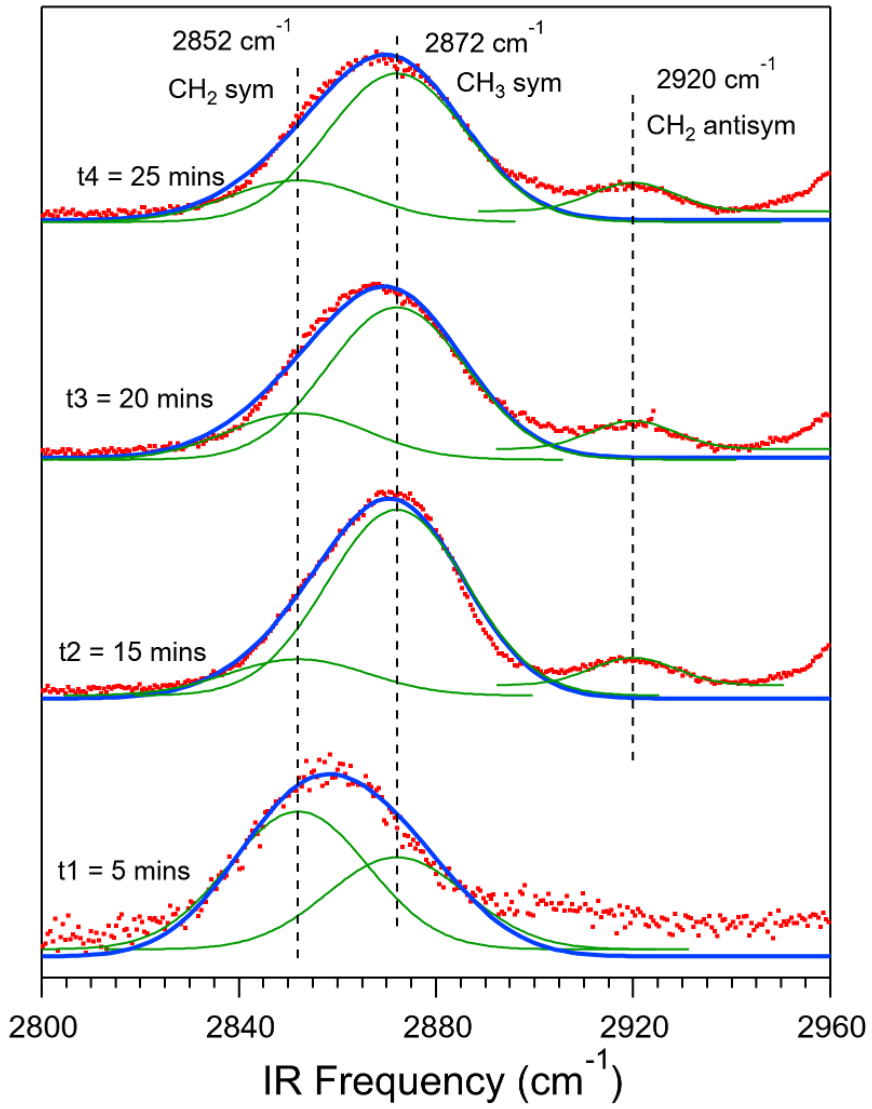

Figure 5.4. VSFG spectra collected at different times after the sample removal from the chamber and fittings of the Gaussians to the specific frequencies

Proceeding from 15 mins to 20 mins VSF measurements, the spectra change in subtler ways. First, the dominant peak shows a slight shift in its band center back to lower frequencies. More noticeable is that the peak's overall intensity decreases. The shift to lower frequency implies that d^+ is starting to contribute more to the band's overall intensity. The diminished intensity in the SSP spectrum is consistent with the chains adopting a new orientation with

chains aligned further away from the surface normal or, equivalently, more parallel to the surface. The relative contributions of d^+ and r^+ to the main feature are shown in Figure 5.4 and reported in Table 5.1. Using the r^+/d^+ ratio as a measure of relative conformational order, results show the ratio to diminish from 5.1 (15 minutes) to 3.3 (20 minutes). These results suggest that the chains are most ordered with the fewest gauche defects at 15 minutes. At longer times as the chains begin to lie along the surface, r^+ begins contributing less to the spectral intensity leading to a reduced ratio *and* a lower intensity overall under the SSP polarization condition. These two changes agree with each other and conclude to just one type of orientation change, which is shown in Figure 5.5.

Spectra acquired at 25 minutes is almost superimposable with the ’20 minute’ spectrum (including an r^-/d^+ ratio of 3.6, equivalent within experimental uncertainty with the 3.3 ratio measured at 20 minutes.) We take this convergence to indicate that surfactant reorganization has finished.

Table 5.1. Peak areas obtained from the fitting process and the ratios of these areas that are used to determine the molecule orientations

Time	Peak areas			Ratios of the areas	
	CH_2 symmetric stretching (2852 cm^{-1})	CH_3 symmetric stretching (2872 cm^{-1})	CH_2 antisymmetric stretching (2920 cm^{-1})	2872 cm^{-1} / 2852 cm^{-1}	2920 cm^{-1} / 2872 cm^{-1}
5 mins	3.42	2.28	-	0.67	-
15 mins	4.34	22.19	1.96	5.11	0.088
20 mins	4.71	15.41	1.72	3.27	0.112
25 mins	4.11	14.69	1.68	3.57	0.114

The changes in structure and orientation observed in Figure 5.5 are consistent with the equilibrium structure of SDS films adsorbed to gypsum reported in Chapter 2. In Chapter 2, three drops (~0.150 mL) of SDS solution were placed onto the gypsum surface and the surface was then air dried for 2 hours. VSFG measurements showed the existence of ordered SDS molecules after all the physisorbed water had evaporated. The orientations of SDS molecules at the surface as deduced from VSF spectra are shown in Figure 2.1 in Chapter 2 and reproduced here for clarity. Therefore, combined with the results presented in this chapter, we conclude that SDS spontaneously adsorbs to the gypsum/aqueous interface and self-assembles into an organized film upon solvent evaporation. Two representative structures illustrating schematically how SDS orientation changes upon solvent evaporation are shown in Figure 5.5.

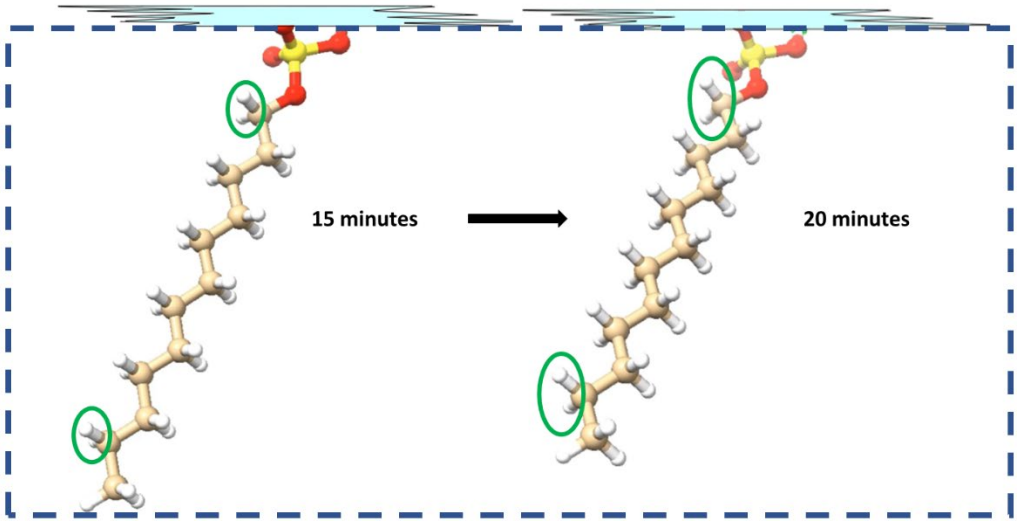

Figure 5.5. Representation of SDS orientations on gypsum surface changing from 15 minutes mark to 20 minutes. Rectangle with dashed lines represents the surface normal.

The structures shown in Figure 5.5 assume an all-*trans* chain conformation and, for reference, a rectangle with dashed lines is included to illustrate the surface normal. To evaluate how such a structure would lead to a VSF spectrum, the selection rule requirements for a VSF response deserve revisiting. In order for a vibration to be VSF active, it must first be in an anisotropic environment (because of the symmetry properties of the $\chi^{(2)}$ tensor) and the vibrational transition must be both IR and Raman active. For the alkyl chain of an SDS monomer, the -CH_3 group will always be IR and Raman active. The -CH_2 groups adjacent the terminal -CH_3 group and the sulfate headgroups will also have normal modes that are IR and Raman active. For the interior -CH_2 groups (from C_2 to C_6), however, selection rules for normal mode IR absorption and Raman scattering will depend upon chain conformation. Chains in an *all*-trans conformation will have local inversion symmetry about the center of each carbon-carbon bond, coupling the normal modes and constraining the symmetric and antisymmetric stretches to in-phase and out-of-phase combinations. A consequence of this coupling is that -CH_2

symmetric stretches along the chain will be out-of-phase (and IR active) or in-phase (and Raman active) and due to the rule of mutual exclusion, these transitions will be VSF *forbidden*. In Figure 5.5, the 15-minute structure has the SDS methyl group directed with its C_3 axis directed along the surface normal. Geometric requirements lead to the C_7 methylene group having a component of its C_2 symmetry axis also along the surface normal allowing a way for d^+ to also acquire VSF intensity. The $C_6 - C_2$ normal mode vibrations will all be VSF forbidden and the contribution of the C_1 methylene group to the overall VSF spectrum will depend on how the sulfate group is associating with the gypsum substrate. The 20-minute spectrum is characterized by a smaller r^+ contribution to the broad feature centered at 2864 cm^{-1} and a growing d^+ band. Again, assuming an all-*trans* conformation, these changes in intensity would indicate a tilting of the chain away from the surface normal as the SDS surfactant begins to lie down on the gypsum substrate.

Discussion and Conclusions

VSFG spectra collected from gypsum/air and gypsum/aqueous SDS interfaces were presented in this study. Spectra collected from gypsum/aqueous SDS interface showed no features suggesting one of three possible causes: subsequent spectra eliminated one of these causes, namely that SDS may not have adsorbed to the gypsum/aqueous interface at all. Of the other two possibilities – adsorption but with no net polar ordering or too little SDS at the surface to be detected due to signal loss from VSF signal transmission across the interface – we believe that the former explanation is more likely. We base this conclusion on the time dependent changes we observe from the gypsum-air interface *after* the SDS solution has been removed. Temporal evolution of the SDS VSF spectra as water evaporates shows that the adsorbed surfactants are becoming more ordered and changing their orientation as time goes on. Given

that the number of SDS at the surface aren't changing after the solution has been removed, the data indicate that an adequate number of SDS did – in fact – adsorb to the surface to be observed even allowing for transmission loss of the VSF signal. The fact that no signal was observed from the solid/liquid interface implies that the adsorbed SDS were disordered and incapable of creating a second order polarization. Results presented in this study may become a basis for studies investigating rate of surfactant -with sulfate headgroup- adsorption on mineral surfaces.

CHAPTER SIX

CONCLUSIONS AND FUTURE DIRECTIONS

Summary

This dissertation describes studies designed to investigate principles underlying an environmental problem using a molecular approach. Experiments analyzed surfactant adsorption on gypsum and the effects of this adsorption on gypsum dissolution properties. Motivating these studies was the need for knowledge about gypsum surface chemistry, the fact that gypsum can be the primary source for dissolved sulfate in ground water[24-27] and responsible for increased groundwater salinity in western landscapes disturbed by energy extraction activities. In addition to the spectroscopic and imaging studies performed during this work, a method was adapted to rapidly and accurately determine sulfate concentrations in ground and surface water samples. Experiments were performed to answer the following questions;

1) Do the surfactants adsorb on gypsum surface?
2) Are there differences between anionic and cationic surfactant adsorption tendencies?
3) How do adsorbed surfactants organize on gypsum surface?
4) Do the adsorbed surfactants suppress/enhance gypsum dissolution?
5) Can a field applicable sulfate analysis technique be developed?

Research presented in Chapter 2 investigated the possibility of surfactant adsorption on gypsum surface. To compare any differences between adsorption behaviors of the anionic and cationic surfactants, two commonly studied surfactants, SDS and DTAC were chosen. VSFG measurements showed that the SDS molecules organized themselves on gypsum surface and

yielded to strong CH_2 and CH_3 signals. DTAC molecules, on the other hand, did not give rise to VSF signals. EDX measurements confirmed the presence of SDS molecules and the SEM image showed presence of thin film structure created by SDS covering the gypsum surface. DTAC molecules, on the other hand, aggregated into disordered islands on the relatively rougher regions on gypsum surface. Conductometric titration analyses with gypsum containing SDS and DTAC solutions showed that significantly less gypsum dissolved in the SDS solution, while sulfate concentrations in DTAC solutions and the reference analyses done with Millipore water showed equivalent amounts of sulfate dissolved in solution.

In Chapter 3, the applicability of conductometric titration for sulfate analysis in the environmental water samples was demonstrated. Samples collected from multiple ground and surface water field sites in southeast Montana at different times of the year were titrated to precipitate the sulfate, while conductivity was continuously recorded. Sulfate concentrations found by titrations were benchmarked against the results reported from MBMG, where an EPA approved sulfate analysis technique was employed. Results from the two measurement types typically agreed to within 10%. To test the applicability of this technique to environmental waters for different types of anions, chloride analyses were conducted using surface water samples collected in south-central and southwest Montana. Titration results were benchmarked against ion chromatography (IC) results and the reported concentrations from IC analyses also agreed closely. Additional analyses of the conductometric data highlighted strong correlations between conductivity and sulfate concentration in the southeast Montana samples.

In Chapter 4, VSFG was used to examine water structure at the gypsum surface. Spectra showed that the two structural water molecules per unit cell in gypsum engage into two different

intermolecular bonding structures. Vibrations of two -OH bonds in one population of water molecules are decoupled. One of them is parallel to the surface and the other one is likely pointing outwards from the surface. The in-plane -OH bond has a very low vibrational frequency (~3020 cm^{-1}) while the free -OH has a vibrational frequency outside the range of what these experiments can measure. The second population of water molecules show a clear vibrational feature assigned to the symmetric stretching motion with both of hydrogen atoms directed away from the surface. While these signals show significantly diminished intensity when the gypsum surface comes into contact with liquid water, the near total intensity recovery of VSFG features after the bulk water has been removed suggests that these structural water molecules are tightly bound to the surface and do not freely exchange with an adjacent aqueous phase.

In Chapter 5, SDS adsorption on gypsum surface from an aqueous phase was investigated. No VSFG signal was observed from gypsum/aqueous SDS interface. However, SDS adsorption becomes evident as the solution is removed and residual physisorbed water begins to evaporate. Time dependent changes in SDS orientation were deduced through comparison of peak areas that belong to specific vibrations. Results showed that SDS molecules were tilting further towards the surface following the evaporation of water, with carbon chains becoming more parallel to the surface plane.

Future Directions

Effect of Surfactant Chain Length

The studies described in Chapter 2 and 4 include experiments with surfactants having 12 carbon chains and only the anionic SDS showed strong affinity for the gypsum substrate. During the early days of those studies, a set of VSFG measurements were also made with 2 and 8 carbon

chain sulfate surfactants: sodium ethyl sulfate (SES) and sodium octyl sulfate (SOS), respectively. These spectra are shown in Figure 6.1. Spectra show weak but detectable features in CH_x region, indicating net polar ordering by both SOS and SES molecules. Signal to noise ratios in the spectra shown in Figure 6.1 are poor making it difficult to assign specific features based on complementary IR and Raman spectra. Improving the signal to noise ratio with the gypsum samples, rather than reference samples -such as gold and DMSO-, would lead to better resolved, higher intensity peaks. Fitting results would then be reliable, and orientations of the adsorbed SES and SOS molecules could be deduced. In addition to the VSFG measurements, conductometric titration can be used to determine any suppression effect of SES and SOS adsorption on gypsum dissolution. These results will be useful to see what role intermolecular van der Waals interactions between chains have on surfactant organization at the gypsum surface.

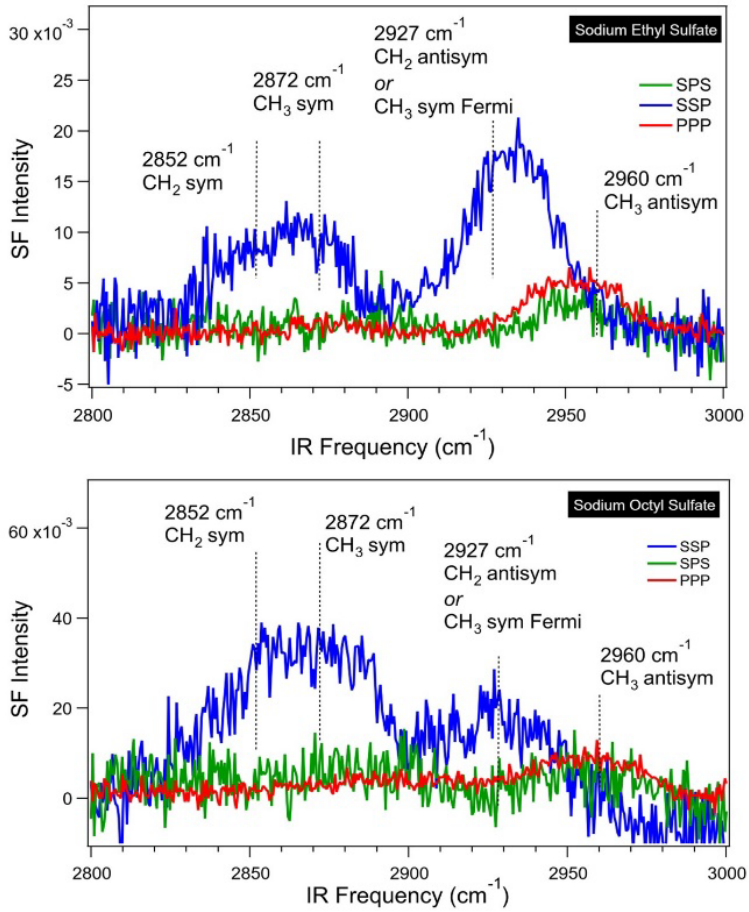

Figure 6.1. VSFG spectra acquired with three different polarization conditions showing SES (top) and SOS (bottom) vibrational structure on gypsum surface

Investigation of PFOS Adsorption on Gypsum Surface

Perfluorooctanesulfonic acid (PFOS) is a member of the PFAS family, a collection of more than 10,000 per- or polyfluorinated contaminants that endanger ecosystem and community health. PFOS is a man-made compound that has heavily been used in various products including fire-fighting foams, food packaging, in nonstick cookware and a host of other applications. In humans, PFOS accumulation has been linked to liver damage and negative impact on the immune system[163]. PFOS (and other PFAS species) do not readily break down in the environment and, as a result, pose a persistent, long-lived threat. PFOS and a related C_8

surfactant, perfluorooctanoic acid (PFOA) are two of the most common and highly regulated PFAS molecules. PFCs' high durability raised environmental concerns.

An interesting question to test is whether or not sulfonate surfactants – and PFOS in particular – show the same strong affinity for gypsum as do sulfate surfactants. If so, then gypsum and other sulfate based minerals such as $MgSO_4 \cdot 7H_2O$, $MgSO_4 \cdot H_2O$, Na_2SO_4, and others can serve as a material for PFOS remediation. Answering this question will require careful, quantitative measurements similar to the ones described in Chapter 2. Adding to this challenge is that VSFG measurements will need to use IR light having frequencies of ~1300 – 1400 cm^{-1}, the frequency range relevant for most $-CF_x$ normal mode stretching motion. PFOS adsorption can also be investigated using EDX and/or XPS. Additionally, by using a home built liquid flow system, PFOS containing water can be filtered through a porous material made from gypsum and the filtered water can be analyzed. Comparison of PFOS concentrations before and after water filtration would also provide further proofs for a possible PFOS adsorption on gypsum.

REFERENCES CITED

(1) Godfrey, S.; Labhasetwar, P.; Wate, S.; Pimpalkar, S. How safe are the global water coverage figures? Case study from Madhya Pradesh, India. *Environ Monit Assess* **2011**, *176* (1-4), 561-574. DOI: 10.1007/s10661-010-1604-3.

(2) Organization, U. N. s. C. s. F. U. a. W. H. *Progress on household drinking water, sanitation and hygiene 2000-2017. Special focus on inequalities*; New York, 2019.

(3) (UNICEF), U. N. C. s. F. *Triple Threat How disease, climate risks, and unsafe water, sanitation and hygiene create a deadly combination for children.*; New York, 2023.

(4) Naser, A.; Wang, Q.; Shamsudduha, M.; Chellaraj, G.; Joseph, G. Modeling the Relationship of Groundwater Salinity to Neonatal and Infant Mortality From the Bangladesh Demographic Health Survey 2000 to 2014. *Geohealth* **2020**, *4* (2). DOI: UNSP e2019GH000229 10.1029/2019GH000229.

(5) Oren, A. Bioenergetic aspects of halophilism. *Microbiol Mol Biol R* **1999**, *63* (2), 334-+. DOI: Doi 10.1128/Mmbr.63.2.334-348.1999.

(6) Yan, N.; Marschner, P.; Cao, W. H.; Zuo, C. Q.; Qin, W. Influence of salinity and water content on soil microorganisms. *Int Soil Water Conse* **2015**, *3* (4), 316-323. DOI: 10.1016/j.iswer.2015.11.003.

(7) Welles, L.; Lopez-Vazquez, C. M.; Hooijmans, C. M.; van Loosdrecht, M. C. M.; Brdjanovic, D. Impact of salinity on the anaerobic metabolism of phosphate-accumulating organisms (PAO) and glycogen-accumulating organisms (GAO). *Appl Microbiol Biot* **2014**, *98* (17), 7609-7622. DOI: 10.1007/s00253-014-5778-4.

(8) Katende, A.; Sagala, F. A critical review of low salinity water flooding: Mechanism, laboratory and field application. *J Mol Liq* **2019**, *278*, 627-649. DOI: 10.1016/j.molliq.2019.01.037.

(9) Vineis, P.; Chan, Q.; Khan, A. Climate change impacts on water salinity and health. *J Epidemiol Glob Hea* **2011**, *1* (1), 5-10. DOI: 10.1016/j.jegh.2011.09.001.

(10) McCallum, L.; Lip, S.; Padmanabhan, S. The hidden hand of chloride in hypertension. *Pflug Arch Eur J Phy* **2015**, *467* (3), 595-603. DOI: 10.1007/s00424-015-1690-8.

(11) Jabed, M. A.; Paul, A.; Nath, T. K. Peoples' Perception of the Water Salinity Impacts on Human Health: A Case Study in South-Eastern Coastal Region of Bangladesh. *Expos Health* **2020**, *12* (1), 41-50. DOI: 10.1007/s12403-018-0283-0.

(12) Ward, M. H.; deKok, T. M.; Levallois, P.; Brender, J.; Gulis, G.; Nolan, B. T.; VanDerslice, J. Workgroup report: Drinking-water nitrate and health-recent findings and research needs. *Environ Health Persp* **2005**, *113* (11), 1607-1614. DOI: 10.1289/ehp.8043.

(13) Chhabra, R. *Soil Salinity and Water Quality*; A.A. Balkema Publishers 1996.

(14) Martin, J. T.; Pederson, G. T.; Woodhouse, C. A.; Cook, E. R.; McCabe, G. J.; Anchukaitis, K. J.; Wise, E. K.; Erger, P. J.; Dolan, L.; McGuire, M.; et al. Increased drought severity tracks warming in the United States' largest river basin. *P Natl Acad Sci USA* **2020**, *117* (21), 11328-11336. DOI: 10.1073/pnas.1916208117.

(15) Lupton, C. T.; Condit, D. D. *Gypsum in the southern part of the Bighorn Mountains, Wyoming*; 1917.

(16) Management, B. o. L. *Soil Survey Pilot Study: Powder River Area Montana*; 1963.

(17) *Ground Water Information Center*. Montana Technological University, https://mbmggwic.mtech.edu/ (accessed 2023 February 23).

(18) USEPA. *Secondary Drinking Water Standards: Guidance for Nuisance Chemicals*. 2023. https://www.epa.gov/sdwa/secondary-drinking-water-standards-guidance-nuisance-chemicals (accessed 2023 March 7).

(19) Pokrovsky, O. S.; Golubev, S. V.; Schott, J. Dissolution kinetics of calcite, dolomite and magnesite at 25 degrees C and 0 to 50 atm pCO(2). *Chem Geol* **2005**, *217* (3-4), 239-255. DOI: 10.1016/j.chemgeo.2004.12.012.

(20) Klimchouk, A. The dissolution and conversion of gypsum and anhydrite. *International Journal of Speleology* **1996**, *25* (3), 2.

(21) Lee, R. W. *Geochemistry of Water in the Fort Union Formation of the Northern Powder River Basin, Southeastern Montana*; Washington, 1981.

(22) *U.S. Annual Coal Production by Basin (2000-2018)*. U.S. Energy Information Administration, 2019. https://www.eia.gov/todayinenergy/detail.php?id=41053# (accessed 2023 February 24, 2023).

(23) *U.S. Geological Survey*; Mineral commodity summaries 2020: U.S. Geological Survey, 2020. DOI: https://doi.org/10.3133/mcs2020.

(24) Al-Charideh, A. Isotopic evidence to characterize the sources of sulfate ions in the carbonate aquifer system in Aleppo basin (North Syria). *Environ Earth Sci* **2015**, *73* (1), 127-137. DOI: 10.1007/s12665-014-3400-9.

(25) Xiao, Q.; Jiang, Y. J.; Shen, L. C.; Yuan, D. X. Origin of calcium sulfate-type water in the Triassic carbonate thermal water system in Chongqing, China: A chemical and isotopic reconnaissance. *Appl Geochem* **2018**, *89*, 49-58. DOI: 10.1016/j.apgeochem.2017.11.011.

(26) Marques, J. M.; Graca, H.; Eggenkamp, H. G. M.; Neves, O.; Carreira, P. M.; Matias, M. J.; Mayer, B.; Nunes, D.; Trancoso, V. N. Isotopic and hydrochemical data as indicators of recharge areas, flow paths and water-rock interaction in the Caldas da Rainha-Quinta das Janelas thermomineral carbonate rock aquifer (Central Portugal). *J Hydrol* **2013**, *476*, 302-313. DOI: 10.1016/j.jhydrol.2012.10.047.

(27) Wang, H. W.; Zhang, Q. Q. Research Advances in Identifying Sulfate Contamination Sources of Water Environment by Using Stable Isotopes. *Int J Env Res Pub He* **2019**, *16* (11). DOI: ARTN 1914
10.3390/ijerph16111914.

(28) Steinmetz, A. *Translation and Guidance on Application of the Montana Narrative Water Quality Criterion for Sulfate*; Montana Dept. of Environmental Quality, Helena, MT, 2014.

(29) Nthunya, L. N.; Maifadi, S.; Mamba, B. B.; Verliefde, A. R.; Mhlanga, S. D. Spectroscopic determination of water salinity in brackish surface water in Nandoni Dam, at Vhembe District, Limpopo Province, South Africa. *Water* **2018**, *10* (8), 990.

(30) Hong, D. D.; Fan, M.; Yu, L. J.; Cao, J. An experimental study simulating the dissolution of gypsum rock. *Energ Explor Exploit* **2018**, *36* (4), 942-954. DOI: 10.1177/0144598717751927.

(31) Knittle, E.; Phillips, W.; Williams, Q. An infrared and Raman spectroscopic study of gypsum at high pressures. *Phys Chem Miner* **2001**, *28* (9), 630-640. DOI: DOI 10.1007/s002690100187.

(32) Link, K. A. Organic enrichment at aqueous interfaces studied with non-linear spectroscopy: cooperative adsorption of soluble saccharides to lipid monolayers. Montana State University, 2019.

(33) Esentürk, O. Molecular Structure and Surface Organization: A Study of Liquid/Vapor Interfaces Using Newly Developed Sum Frequency Methods. University of Maryland, 2004.

(34) Velarde, L.; Zhang, X. Y.; Lu, Z.; Joly, A. G.; Wang, Z. M.; Wang, H. F. Communication: Spectroscopic phase and lineshapes in high-resolution broadband sum frequency vibrational spectroscopy: Resolving interfacial inhomogeneities of "identical" molecular groups. *J Chem Phys* **2011**, *135* (24). DOI: Artn 241102
10.1063/1.3675629.

(35) Yiyen, G.; Duck, K. V.; Walker, R. A. Surfactant Adsorption to Gypsum Surfaces and the Effects on Solubility in Aqueous Solutions. *Langmuir* **2022**, *38* (9), 2804-2810. DOI: 10.1021/acs.langmuir.1c02890.

(36) Su, Y.; Li, H. F.; Ma, H. B.; Robertson, J.; Nathan, A. Controlling Surface Termination and Facet Orientation in Cu2O Nanoparticles for High Photocatalytic Activity: A Combined Experimental and Density Functional Theory Study. *Acs Applied Materials & Interfaces* **2017**, *9* (9), 8100-8106. DOI: 10.1021/acsami.6b15648.

(37) Shen, Q.; Wang, L. C.; Huang, Y. P.; Sun, J. L.; Wang, H. H.; Zhou, Y.; Wang, D. J. Oriented aggregation and novel phase transformation of vaterite controlled by the synergistic effect of calcium dodecyl sulfate and n-pentanol. *Journal of Physical Chemistry B* **2006**, *110* (46), 23148-23153. DOI: 10.1021/jp064039n.

(38) Shen, Q.; Wei, H.; Wang, L. C.; Zhou, Y.; Zhao, Y.; Zhang, Z. Q.; Wang, D. J.; Xu, G. Y.; Xu, D. F. Crystallization and aggregation behaviors of calcium carbonate in the presence of poly(vinylpyrrolidone) and sodium dodecyl sulfate. *Journal of Physical Chemistry B* **2005**, *109* (39), 18342-18347. DOI: 10.1021/jp052094a.

(39) Karimi, M.; Al-Maamari, R. S.; Ayatollahi, S.; Mehranbod, N. Wettability alteration and oil recovery by spontaneous imbibition of low salinity brine into carbonates: Impact of Mg2+, SO42- and cationic surfactant. *Journal of Petroleum Science and Engineering* **2016**, *147*, 560-569. DOI: 10.1016/j.petrol.2016.09.015.

(40) Li, G.; Guo, S. H.; Hu, J. X. The influence of clay minerals and surfactants on hydrocarbon removal during the washing of petroleum-contaminated soil. *Chemical Engineering Journal* **2016**, *286*, 191-197. DOI: 10.1016/j.cej.2015.10.006.

(41) Zhao, S. F.; Li, Y. P.; Cao, Z. L.; Wang, J. L. Sorption-desorption mechanisms and environmental friendliness of different surfactants in enhancing remediation of soil contaminated with polycyclic aromatic hydrocarbons. *Journal of Soils and Sediments* **2020**, *20* (7), 2817-2828. DOI: 10.1007/s11368-020-02640-0.

(42) Sis, H.; Chander, S. Reagents used in the flotation of phosphate ores: a critical review. *Minerals Engineering* **2003**, *16* (7), 577-585. DOI: 10.1016/s0892-6875(03)00131-6.

(43) Nicol, S. K.; Galvin, K. P.; Engel, M. D. ION FLOTATION - POTENTIAL APPLICATIONS TO MINERAL PROCESSING. *Minerals Engineering* **1992**, *5* (10-12), 1259-1275. DOI: 10.1016/0892-6875(92)90163-4.

(44) Zhang, N. N.; Nguyen, A. V.; Zhou, C. C. A review of the surface features and properties, surfactant adsorption and floatability of four key minerals of diasporic bauxite resources. *Advances in Colloid and Interface Science* **2018**, *254*, 56-75. DOI: 10.1016/j.cis.2018.03.005.

(45) Chang, Z. Y.; Chen, X. M.; Peng, Y. J. The adsorption behavior of surfactants on mineral surfaces in the presence of electrolytes - A critical review. *Minerals Engineering* **2018**, *121*, 66-76. DOI: 10.1016/j.mineng.2018.03.002.

(46) Xu, L. H.; Tian, J.; Wu, H. Q.; Lu, Z. Y.; Sun, W.; Hu, Y. H. The flotation and adsorption of mixed collectors on oxide and silicate minerals. *Advances in Colloid and Interface Science* **2017**, *250*, 1-14. DOI: 10.1016/j.cis.2017.11.003.

(47) Li, Y.; Wei, M. L.; Liu, L.; Xue, Q.; Yu, B. W. Adsorption of toluene on various natural soils: Influences of soil properties, mechanisms, and model. *Science of the Total Environment* **2020**, *740*. DOI: 10.1016/j.scitotenv.2020.140104.

(48) Silva, L. A.; Garrot, T. G.; Pereira, A. M.; Correia, J. C. G. Historical perspective and bibliometric analysis of molecular modeling applied in mineral flotation systems. *Minerals Engineering* **2021**, *170*. DOI: 10.1016/j.mineng.2021.107062.

(49) Sun, W. H.; Liu, W. G.; Dai, S. J.; Duan, H.; Liu, W. B. Inserting EO groups to improve the performance of fatty acid collectors: Flotation and adsorption study performed with calcite, dolomite, and quartz. *Separation and Purification Technology* **2021**, *272*. DOI: 10.1016/j.seppur.2021.118952.

(50) Wu, H. Q.; Tian, J.; Xu, L. H.; Wang, Z. J.; Xu, Y. B.; Gao, Z. Y.; Sun, W.; Hu, Y. H. Anisotropic surface chemistry properties of salt-type and oxide mineral crystals. *Minerals Engineering* **2020**, *154*. DOI: 10.1016/j.mineng.2020.106411.

(51) Liu, W. P.; Wang, Z. X.; Wang, X. M.; Miller, J. D. Smithsonite flotation with lauryl phosphate. *Minerals Engineering* **2020**, *147*. DOI: 10.1016/j.mineng.2019.106155.

(52) Shrimali, K.; Yin, X. H.; Wang, X. M.; Miller, J. D. Fundamental issues on the influence of starch in amine adsorption by quartz. *Colloids and Surfaces a-Physicochemical and Engineering Aspects* **2017**, *522*, 642-651. DOI: 10.1016/j.colsurfa.2017.03.031.

(53) Zhu, G. L.; Wang, X. M.; Li, E. Z.; Wang, Y. H.; Miller, J. D. Wetting characteristics of spodumene surfaces as influenced by collector adsorption. *Minerals Engineering* **2019**, *130*, 117-128. DOI: 10.1016/j.mineng.2018.10.010.

(54) Wanhala, A. K.; Doughty, B.; Bryantsev, V. S.; Wu, L.; Mahurin, S. M.; Jansone-Popova, S.; Cheshire, M. C.; Navrotsky, A.; Stack, A. G. Adsorption mechanism of alkyl hydroxamic acid onto bastnasite: Fundamental steps toward rational collector design for rare earth elements. *Journal of Colloid and Interface Science* **2019**, *553*, 210-219. DOI: 10.1016/j.jcis.2019.06.025.

(55) Sutton, J. E.; Roy, S.; Chowdhury, A. U.; Wu, L.; Wanhala, A. K.; De Silva, N.; Jansone-Popova, S.; Hay, B. P.; Cheshire, M. C.; Windus, T. L.; et al. Molecular Recognition at Mineral

Interfaces: Implications for the Beneficiation of Rare Earth Ores. *Acs Applied Materials & Interfaces* **2020**, *12* (14), 16327-16341. DOI: 10.1021/acsami.9b22902.

(56) Kijjanapanich, P.; Annachatre, A. P.; Esposito, G.; Lens, P. N. L. Use of organic substrates as electron donors for biological sulfate reduction in gypsferous mine soils from Nakhon Si Thammarat (Thailand). *Chemosphere* **2014**, *101*, 1-7.

(57) Perry, E.; Velazquez-Oliman, G.; Marin, L. The hydrogeochemistry of the karst aquifer system of the northern Yucatan Peninsula, Mexico. *International Geology Review* **2002**, *44* (3), 191-221.

(58) Zhang, D.; Li, X. D.; Zhao, Z. Q.; Liu, C. Q. Using dual isotopic data to track the sources and behaviors of dissolved sulfate in the western North China Plain. *Applied Geochemistry* **2015**, *52*, 43-56.

(59) Matin, A.; Rahman, F.; Shafi, H. Z.; Zubair, S. M. Scaling of reverse osmosis membranes used in water desalination: Phenomena, impact and control; future direcctions. *Desalinaton* **2019**, *455*, 135-157.

(60) Fipps, G. *Irrigation Water Quality Standards and Salinity Management Strategies*; B-1667 4-03; Taxas A&M, College Station, Texas, 2003. https://cdn-ext.agnet.tamu.edu/wp-content/uploads/2019/03/EB-1667-irrigation-water-quality-standards-and-salinity-management-strategies-1.pdf (accessed 12 September, 2021).

(61) Sharma, M. K.; Kumar, M. Sulphate contamination in groundwater and its remediation: an overview. *Environmental Monitoring and Assessment* **2020**, *192* (2). DOI: 10.1007/s10661-019-8051-6.

(62) Anderson, G. C.; Pathan, S.; Easton, J.; Hall, D. J. M.; Sharma, R. Short- and Long-Term Effects of Lime and Gypsum Applications on Acid Soils in a Water-Limited Environment: 2. Soil Chemical Properties. *Agronomy-Basel* **2020**, *10* (12). DOI: 10.3390/agronomy10121987.

(63) Anderson, G. C.; Pathan, S.; Hall, D. J. M.; Sharma, R.; Easton, J. Short- and Long-Term Effects of Lime and Gypsum Applications on Acid Soils in a Water-Limited Environment: 3. Soil Solution Chemistry. *Agronomy-Basel* **2021**, *11* (5). DOI: 10.3390/agronomy11050826.

(64) Sharma, H.; Dufour, S.; Arachchilage, G. W. P. P.; Weerasooriya, U.; Pope, G. A.; Mohanty, K. Alternative alakalies for ASP flooding in anhydrite containing oil reservoirs. *Fuel* **2015**, *140*, 407-420.

(65) Xu, Y.; Liao, Y.; Lin, Z.; Lin, J.; Li, Q.; Lin, J.; Jin, Z. Precipitation of calcium sulfate dihydrate in the presence of fulvic acid and magnesium ion. *Chemical Engineering Journal* **2019**, *361*, 1078-1088.

(66) Felmy, A. R.; Rai, D.; Amonette, J. E. The solubility of barite and celestite in sodium-sulfate - evaluation of thermodynamic data *Journal of Solution Chemistry* **1990**, *19* (2), 175-185. DOI: 10.1007/bf00646611.

(67) Monnin, C.; Galinier, C. The solubility of celestite and barite in electrolyte-solutions and natural waters at 25˚C - a thermodynamic study. *Chemical Geology* **1988**, *71* (4), 283-296. DOI: 10.1016/0009-2541(88)90055-1.

(68) Garcia, J.; Schultz, L. D. Determination of Sulfate by Conductometric Titration: An Undergraduate Laboratory Experiment. *JOurnal of Chemical Edcuation* **2016**, *93*, 910-914.

(69) Lambert, A. G.; Davies, P. B.; Neivandt, D. J. Implementing the theory of sum frequency generation vibrational spectroscopy: A tutorial review. *Applied Spectroscopy Reviews* **2005**, *40* (2), 103-145. DOI: 10.1081/asr-200038326.

(70) Vidal, F.; Tadjeddine, A. Sum-frequency generation spectroscopy of interfaces. *Reports on Progress in Physics* **2005**, *68* (5), 1095-1127. DOI: 10.1088/0034-4885/68/5/r03.

(71) Wang, H. F.; Gan, W.; Lu, R.; Rao, Y.; Wu, B. H. Quantitative spectral and orientational analysis in surface sum frequency generation vibrational spectroscopy (SFG-VS). *Int Rev Phys Chem* **2005**, *24* (2), 191-256. DOI: 10.1080/01442350500225894.

(72) Can, S. Z.; Mago, D. D.; Walker, R. A. Structure and organization of hexadecanol isomers adsorbed to the air/water interface. *Langmuir* **2006**, *22* (19), 8043-8049. DOI: 10.1021/la060816z.

(73) Karnes, J. J.; Gobrogge, E. A.; Walker, R. A.; Benjamin, I. Unusual Structure and Dynamics at Silica/Methanol and Silica/Ethanol Interfaces-A Molecular Dynamics and Nonlinear Optical Study. *Journal of Physical Chemistry B* **2016**, *120* (8), 1569-1578. DOI: 10.1021/acs.jpcb.5b07777.

(74) Link, K. A.; Hsieh, C. Y.; Tuladhar, A.; Chase, Z.; Wang, Z. M.; Wang, H. F.; Walker, R. A. Vibrational studies of saccharide-induced lipid film reorganization at aqueous/air interfaces. *Chemical Physics* **2018**, *512*, 104-110. DOI: 10.1016/j.chemphys.2018.02.011.

(75) Esenturk, O.; Walker, R. A. Surface vibrational structure at alkane liquid/vapor interfaces. *Journal of Chemical Physics* **2006**, *125* (17). DOI: 10.1063/1.2356858.

(76) Koroleva, M. Y.; Karakatenko, E. Y.; Yurtov, E. V. Synthesis of hydroxyapatite nanoparticles by controlled precipitation in the presence of sodium docecyl sulfate. *Colloid Journal* **2020**, *82*, 275-283.

(77) Zhang, P.; Xiang, M. X.; Li, P.; Ouyang, S. D.; He, T.; Deng, Q. The enhancement roles of sulfate on the adsorption of sodium dodecylsulfate by calcium-based layered double hydroxide:

microstructure and thermal behaviors. *Environmental Science and Pollution Research* **2019**, *26* (19).

(78) Baviere, M.; Bazin, B.; Aude, R. Calcium effect on the solubility of sodium dodecyl-sulfate in sodium-chloride solutions *Journal of Colloid and Interface Science* **1983**, *92* (2), 580-583. DOI: 10.1016/0021-9797(83)90179-0.

(79) Macphail, R. A.; Strauss, H. L.; Snyder, R. G.; Elliger, C. A. C-H Stretching modes and the sructure of normal-alkyl chains. 2. Long, all-trans chains *Journal of Physical Chemistry* **1984**, *88* (3), 334-341. DOI: 10.1021/j150647a002.

(80) Snyder, R. G.; Strauss, H. L.; Elliger, C. A. C-H Stretching modes and the sructure of normal-alkyl chains. 1. Long, disordered chains *Journal of Physical Chemistry* **1982**, *86* (26), 5145-5150. DOI: 10.1021/j100223a018.

(81) Conboy, J. C.; Messmer, M. C.; Richmond, G. L. Dependence of alkyl chain conformation of simple ionic surfactants on head group functionality as studied by vibrational sum-frequency spectroscopy. *Journal of Physical Chemistry B* **1997**, *101* (34), 6724-6733.

(82) Brindza, M. R.; Ding, F.; Fourkas, J. T.; Walker, R. A. n-alkane adsorption to polar silica surfaces. *Journal of Chemical Physics* **2010**, *132* (11).

(83) Kryachko, E. S.; Zeegers-Huyskens, T. Theoretical study of the CH center dot center dot center dot X- interaction of fluoromethanes and chloromethanes with fluoride, chloride, and hydroxide anions. *Journal of Physical Chemistry A* **2002**, *106* (29), 6832-6838.

(84) Fourkas, J. T.; Walker, R. A.; Can, S. Z.; Gershgoren, E. Effects of reorientation in vibrational sum-frequency spectroscopy. *Journal of Physical Chemistry C* **2007**, *111* (25), 8902-8915. DOI: 10.1021/jp0690401.

(85) Xiao, Y.; Hao, Q.; Zhang, Y.; Zhu, Y.; Yin, S.; Qin, L.; Li, X. Investigating sources, driving forces and potential health risks of nitrate and fluoride in groundwater of a typical alluvial fan plain. *Sci Total Environ* **2022**, *802*, 149909. DOI: 10.1016/j.scitotenv.2021.149909 From NLM Medline.

(86) Chaudhuri, S.; Ale, S. Long term (1960-2010) trends in groundwater contamination and salinization in the Ogallala aquifer in Texas. *J Hydrol* **2014**, *513*, 376-390. DOI: 10.1016/j.jhydrol.2014.03.033.

(87) Deonarine, A.; Schwartz, G. E.; Ruhl, L. S. Environmental Impacts of Coal Combustion Residuals: Current Understanding and Future Perspectives. *Environ Sci Technol* **2023**, *57* (5), 1855-1869. DOI: 10.1021/acs.est.2c06094 From NLM Medline.

(88) Dugan, H. A.; Bartlett, S. L.; Burke, S. M.; Doubek, J. P.; Krivak-Tetley, F. E.; Skaff, N. K.; Summers, J. C.; Farrell, K. J.; McCullough, I. M.; Morales-Williams, A. M.; et al. Salting our freshwater lakes. *P Natl Acad Sci USA* **2017**, *114* (17), 4453-4458. DOI: 10.1073/pnas.1620211114.

(89) Ben Ahmed, C.; Ben Rouina, B.; Sensoy, S.; Boukhriss, M. Saline Water Irrigation Effects on Fruit Development, Quality, and Phenolic Composition of Virgin Olive Oils, Cv. Chemlali. *J Agr Food Chem* **2009**, *57* (7), 2803-2811. DOI: 10.1021/jf8034379.

(90) Abdul, R. M.; Mutnuri, L.; Dattatreya, P. J.; Mohan, D. A. Assessment of drinking water quality using ICP-MS and microbiological methods in the Bholakpur area, Hyderabad, India. *Environ Monit Assess* **2012**, *184* (3), 1581-1592. DOI: 10.1007/s10661-011-2062-2.

(91) Raue, B.; Brauch, H. J.; Frimmel, F. H. Determination of Sulfate in Natural-Waters by Icp/Oes - Comparative-Studies with Ion Chromatography. *Fresen J Anal Chem* **1991**, *340* (6), 395-398. DOI: Doi 10.1007/Bf00321590.

(92) USEPA. *Methods for the Determination of Inorganic Substances in Environmental Samples*; 1993.

(93) Markovarga, G.; Csiky, I.; Jonsson, J. A. Ion Chromatographic Determination of Nitrate and Sulfate in Natural-Waters Containing Humic Substances. *Anal Chem* **1984**, *56* (12), 2066-2069. DOI: DOI 10.1021/ac00276a020.

(94) Johnson, K. S. Evaporite karst in the United States. *Carbonate Evaporite* **1997**, *12* (1), 2-14. DOI: Doi 10.1007/Bf03175797.

(95) Fipps, G. Irrigation Water Quality Standards and Salinity Management Strategies. 2003.

(96) McMahon, A. *Montana Pollutant Discharge Elimination System Permint Fact Sheet*; 2014.

(97) Tozsin, G.; Arol, A. I.; Duzgun, S.; Soydan, H.; Torun, A. Effects of abandoned coal mine on the water quality. *Int J Coal Prep Util* **2022**, *42* (11), 3202-3212. DOI: 10.1080/19392699.2022.2044320.

(98) Mao, H. R.; Wang, C. Y.; Qu, S.; Liao, F.; Wang, G. C.; Shi, Z. M. Source and evolution of sulfate in the multi-layer groundwater system in an abandoned mine-Insight from stable isotopes and Bayesian isotope mixing model. *Sci Total Environ* **2023**, *859*. DOI: ARTN 160368 10.1016/j.scitotenv.2022.160368.

(99) Issa, Y. M.; Amin, A. S. Conductometric Titration of Pindolol and Propranolol Using Ammonium Reineckate and Potassium Tetracyanonickelate. *Mikrochim Acta* **1995**, *118* (1-2), 85-91. DOI: Doi 10.1007/Bf01242231.

(100) Beck, S.; Methot, M.; Bouchard, J. General procedure for determining cellulose nanocrystal sulfate half-ester content by conductometric titration (vol 22, pg 101, 2015). *Cellulose* **2015**, *22* (1), 117-117. DOI: 10.1007/s10570-014-0539-1.

(101) Garcia, J.; Schultz, L. D. Determination of Sulfate by Conductometric Titration: An Undergraduate Laboratory Experiment. *J Chem Educ* **2016**, *93* (5), 910-914. DOI: 10.1021/acs.jchemed.5b00941.

(102) Seidell, A. *Solubilities of inorganic and organic compounds, a compilation of quantitative solubility data from the periodical literature*; Van Nostrand, 1919.

(103) Felmy, A. R.; Rai, D.; Amonette, J. E. The Solubility of Barite and Celestite in Sodium-Sulfate - Evaluation of Thermodynamic Data. *J Solution Chem* **1990**, *19* (2), 175-185. DOI: Doi 10.1007/Bf00646611.

(104) Rumble, J. R.; Lide, D. R.; Bruno, T. J. *CRC handbook of chemistry and physics : a ready-reference book of chemical and physical data*; CRC Press, 2018.

(105) Kirchner, J. W.; Feng, X. H.; Neal, C. Fractal stream chemistry and its implications for contaminant transport in catchments. *Nature* **2000**, *403* (6769), 524-527. DOI: Doi 10.1038/35000537.

(106) Harman, C. J. Time-variable transit time distributions and transport: Theory and application to storage-dependent transport of chloride in a watershed. *Water Resour Res* **2015**, *51* (1), 1-30. DOI: 10.1002/2014wr015707.

(107) Timmer, J. *MBMG Analytical Laboratory: Quality Assurance Manual: Montana Bureau of Mines and Geology Open-File Report 729, 8 p.*; 2020.

(108) Sigler, W. A.; Ewing, S. A.; Jones, C. A.; Payn, R. A.; Brookshire, E. N. J.; Klassen, J. K.; Jackson-Smith, D.; Weissmann, G. S. Connections among soil, ground, and surface water chemistries characterize nitrogen loss from an agricultural landscape in the upper Missouri River Basin. *J Hydrol* **2018**, *556*, 247-261. DOI: 10.1016/j.jhydrol.2017.10.018.

(109) Sigler, W. A.; Ewing, S. A.; Jones, C. A.; Payn, R. A.; Miller, P.; Maneta, M. Water and nitrate loss from dryland agricultural soils is controlled by management, soils, and weather. *Agr Ecosyst Environ* **2020**, *304*. DOI: ARTN 107158 10.1016/j.agee.2020.107158.

(110) DeGrandpre, E. L.; DeGrandpre, M. D.; Colman, B. P.; Valett, H. M. Observations of River Solute Concentrations during Ice Formation. *Acs Est Water* **2021**, *1* (8), 1695-1701. DOI: 10.1021/acsestwater.1c00064.

(111) Peipoch, M.; Davis, P. B.; Valett, H. M. Biophysical Heterogeneity, Hydrologic Connectivity, and Productivity of a Montane Floodplain Forest. *Ecosystems* **2022**. DOI: 10.1007/s10021-022-00769-2.

(112) Voast, W. A. V.; Reiten, J. C. *Hydrogeologic responses: Twenty years of surface coal mining in southeastern Montana: Montana Bureau of Mines and Geology Memoir 62, 30 p., 2 sheets*; 1988.

(113) Bonadio, A.; Souza, J. A. Hybrid MAPbI3 Perovskite Growth Mechanism from Irregular Particles to Cuboid and Hopper-Type Morphologies. *Journal of the Brazilian Chemical Society* **2022**, *33* (11), 1273-1280. DOI: 10.21577/0103-5053.20220057.

(114) Cao, H.; Jia, X. D.; Li, Y. L.; Amador, C.; Ding, Y. L. CFD-DNS simulation of irregular-shaped particle dissolution. *Particuology* **2020**, *50*, 144-155. DOI: 10.1016/j.partic.2019.08.003.

(115) Lasaga, A. C.; Luttge, A. Variation of crystal dissolution rate based on a dissolution stepwave model. *Science* **2001**, *291* (5512), 2400-2404. DOI: 10.1126/science.1058173.

(116) Li, Y. J.; Pan, H.; Li, Z. J. Unravelling the dissolution dynamics of silicate minerals by deep learning molecular dynamics simulation: A case of dicalcium silicate. *Cement and Concrete Research* **2023**, *165*. DOI: 10.1016/j.cemconres.2023.107092.

(117) Sutheimer, S. H.; Maurice, P. A.; Zhou, Q. H. Dissolution of well and poorly crystallized kaolinites: Al speciation and effects of surface characteristics. *American Mineralogist* **1999**, *84* (4), 620-628.

(118) Truesdale, V. W. Rate Equations and an Ion-pair Mechanism for Batch Dissolution of Gypsum: Repositioning the Shrinking Object Model at the Core of Hydrodynamic Modelling. *Aquatic Geochemistry* **2011**, *17* (2), 141-164. DOI: 10.1007/s10498-010-9112-1.

(119) Wu, Y. J.; Deng, D. D.; Jiang, J.; Li, F.; Zeng, J. Q.; Guo, X. Y.; Zhu, F.; Jiang, Y. F.; Xue, S. G. Ca-driven stable regulatory of alkalinity within desilication products: Experimental, modeling, transformation mechanism and DFT study. *Science of the Total Environment* **2023**, *868*. DOI: 10.1016/j.scitotenv.2023.161708.

(120) Yin, X. H.; Gupta, V.; Du, H.; Wang, X. M.; Miller, J. D. Surface charge and wetting characteristics of layered silicate minerals. *Advances in Colloid and Interface Science* **2012**, *179*, 43-50. DOI: 10.1016/j.cis.2012.06.004.

(121) Stack, A. G.; Borreguero, J. M.; Prisk, T. R.; Mamontov, E.; Wang, H. W.; Vlcek, L.; Wesolowski, D. J. Precise determination of water exchanges on a mineral surface. *Physical Chemistry Chemical Physics* **2016**, *18* (41), 28819-28828. DOI: 10.1039/c6cp05836a.

(122) Martin, P.; Manzano, H.; Dolado, J. S. Mechanisms and Dynamics of Mineral Dissolution: A New Kinetic Monte Carlo Model. *Adv Theor Simul* **2019**, *2* (10). DOI: ARTN 1900114 10.1002/adts.201900114.

(123) Dove, P. M.; Czank, C. A. Crystal-Chemical Controls on the Dissolution Kinetics of the Isostructural Sulfates - Celestite, Anglesite and Barite. *Geochimica Et Cosmochimica Acta* **1995**, *59* (10), 1907-1915. DOI: 10.1016/0016-7037(95)00116-6.

(124) Stack, A. G.; Raiteri, P.; Gale, J. D. Accurate Rates of the Complex Mechanisms for Growth and Dissolution of Minerals Using a Combination of Rare-Event Theories. *Journal of the American Chemical Society* **2012**, *134* (1), 11-14. DOI: 10.1021/ja204714k.

(125) Stack, A. G. Molecular Dynamics Simulations of Solvation and Kink Site Formation at the {001} Barite-Water Interface. *Journal of Physical Chemistry C* **2009**, *113* (6), 2104-2110. DOI: 10.1021/jp8062993.

(126) Brittanica. *'plaster'*. 2022. https://www.britannica.com/technology/plaster (accessed 2023.

(127) Chen, L.; Dick, W. A. *Gypsum as an Agricultural Amendment*; Ohio State University, 2011.

(128) Huang, W.; Ertekin, E.; Wang, T. F.; Cruz, L.; Dailey, M.; DiRuggiero, J.; Kisailus, D. Mechanism of water extraction from gypsum rock by desert colonizing microorganisms. *Proceedings of the National Academy of Sciences of the United States of America* **2020**, *117* (20), 10681-10687. DOI: 10.1073/pnas.2001613117.

(129) Jin, Q. X.; Perry, L. N.; Bullard, J. W. Temperature dependence of gypsum dissolution rates. *Cement and Concrete Research* **2020**, *129*. DOI: ARTN 105969 10.1016/j.cemconres.2019.105969.

(130) Lebedev, A. L. Kinetics of gypsum dissolution in water. *Geochem Int+* **2015**, *53* (9), 811-824. DOI: 10.1134/S0016702915070058.

(131) Kijjanapanich, P.; Annachhatre, A. P.; Lens, P. N. L. Biological Sulfate Reduction for Treatment of Gypsum Contaminated Soils, Sediments, and Solid Wastes. *Crit Rev Env Sci Tec* **2014**, *44* (10), 1037-1070. DOI: 10.1080/10643389.2012.743270.

(132) Xu, Q. Y.; Townsend, T.; Bitton, G. Inhibition of hydrogen sulfide generation from disposed gypsum drywall using chemical inhibitors. *J Hazard Mater* **2011**, *191* (1-3), 204-211. DOI: 10.1016/j.jhazmat.2011.04.063.

(133) Rahimi, M. R.; Mohammadi, S. D.; Eydokhti, A. T. Laboratory simulation of gypsum rock dissolution at different pressure, water flow velocities and pH ranges Abbreviated title: Gypsum rock dissolution simulation. *Q J Eng Geol Hydroge* **2022**. DOI: 10.1144/qjegh2021-120.

(134) Hou, S. C.; Wang, J.; Wang, X. X.; Chen, H. Y.; Xiang, L. Effect of Mg2+ on Hydrothermal Formation of alpha-CaSO4 center dot 0.5H(2)O Whiskers with High Aspect Ratios. *Langmuir* **2014**, *30* (32), 9804-9810. DOI: 10.1021/la502451f.

(135) Ke, B. L.; Zhang, Q.; Li, X. H.; Shen, Z. H. Adsorption and solidification of cadmium by calcium sulfate dihydrate (gypsum) in an aqueous environment: a dispersion-corrected DFT and ab initio molecular dynamics study. *Phys Chem Chem Phys* **2022**, *24* (16), 9521-9533. DOI: 10.1039/d1cp03964d.

(136) Finot, E.; Lesniewska, E.; Goudonnet, J. P.; Mutin, J. C. Correlation between surface forces and surface reactivity in the setting of plaster by atomic force microscopy. *Applied Surface Science* **2000**, *161* (3-4), 316-322. DOI: 10.1016/s0169-4332(00)00030-1.

(137) Finot, E.; Lesniewska, E.; Goudonnet, J. P.; Mutin, J. C.; Domenech, M.; Kadi, A. A. Correlating surface forces with surface reactivity of gypsum crystals by atomic force microscopy. Comparison with theological properties of plaster. *Solid State Ionics* **2001**, *141*, 39-46. DOI: 10.1016/s0167-2738(01)00718-4.

(138) Songen, H.; Silvestri, A.; Roshni, T.; Klassen, S.; Bechstein, R.; Raiteri, P.; Gale, J. D.; Kuhnle, A. Does the Structural Water within Gypsum Remain Crystalline at the Aqueous Interface? *J Phys Chem C* **2021**, *125* (39), 21670-21677. DOI: 10.1021/acs.jpcc.1c06213.

(139) Krause, F.; Renner, B.; Coppens, F.; Dewanckele, J.; Schwotzer, M. Reactivity of Gypsum-Based Materials Subjected to Thermal Load: Investigation of Reaction Mechanisms. *Materials* **2020**, *13* (6). DOI: ARTN 1427 10.3390/ma13061427.

(140) Santos, J. C. C.; Negreiros, F. R.; Pedroza, L. S.; Dalpian, G. M.; Miranda, P. B. Interaction of Water with the Gypsum (010) Surface: Structure and Dynamics from Nonlinear Vibrational Spectroscopy and Ab Initio Molecular Dynamics. *Journal of the American Chemical Society* **2018**, *140* (49), 17141-17152. DOI: 10.1021/jacs.8b09907.

(141) Geiger, F. M. Second Harmonic Generation, Sum Frequency Generation, and chi((3)): Dissecting Environmental Interfaces with a Nonlinear Optical Swiss Army Knife. *Annu Rev Phys Chem* **2009**, *60*, 61-83. DOI: 10.1146/annurev.physchem.59.032607.093651.

(142) Jubb, A. M.; Hua, W.; Allen, H. C. Environmental Chemistry at Vapor/Water Interfaces: Insights from Vibrational Sum Frequency Generation Spectroscopy. *Annual Review of Physical Chemistry, Vol 63* **2012**, *63*, 107-130. DOI: 10.1146/annurev-physchem-032511-143811.

(143) Du, Q.; Superfine, R.; Freysz, E.; Shen, Y. R. Vibrational Spectroscopy of Water at the Vapor Water Interface. *Phys Rev Lett* **1993**, *70* (15), 2313-2316. DOI: DOI 10.1103/PhysRevLett.70.2313.

(144) Gobrogge, E. A.; Walker, R. A. Binary Solvent Organization at Silica/Liquid Interfaces: Preferential Ordering in Acetonitrile-Methanol Mixtures. *J Phys Chem Lett* **2014**, *5* (15), 2688-2693. DOI: 10.1021/jz500906d.

(145) R., K.; J., S. Intramolecular and intermolecular interactions in and between water molecules in calcium sulfate dihydrate. *Journal of Chemical Physics* **1971**, *54* (12), 5331-5336.

(146) Takahasi, H.; Maehara, I.; Kaneko, N. Infrared reflection spectra of gypsum. *Spectrochimica Acta Part a-Molecular and Biomolecular Spectroscopy* **1983**, *39* (5), 449-455.

(147) Berenblut, B. J.; Dawson, P.; Wilkinson, G. R. Raman Spectrum of Gypsum *Spectrochimica Acta Part a-Molecular Spectroscopy* **1971**, *A 27* (9), 1849-+. DOI: 10.1016/0584-8539(71)80238-6.

(148) Schmid, T.; Jungnickel, R.; Dariz, P. Insights into the CaSO4-H2O System: A Raman-Spectroscopic Study. *Minerals* **2020**, *10* (2). DOI: 10.3390/min10020115.

(149) Gragson, D. E.; McCarty, B. M.; Richmond, G. L. Ordering of interfacial water molecules at the charged air/water interface observed by vibrational sum frequency generation. *Journal of the American Chemical Society* **1997**, *119* (26), 6144-6152. DOI: DOI 10.1021/ja962277y.

(150) Buck, U.; Huisken, F. Infrared spectroscopy of size-selected water and methanol clusters. *Chemical Reviews* **2000**, *100* (11), 3863-3890.

(151) Sun, Q.; Guo, Y. Vibrational sum frequency generation spectroscopy of the air/water interface. *J Mol Liq* **2016**, *213*, 28-32. DOI: 10.1016/j.molliq.2015.11.004.

(152) Delattre, S.; Balan, E.; Lazzeri, M.; Blanchard, M.; Guillaumet, M.; Beyssac, O.; Hl, E. H.; Winkler, B.; Salje, E. K. H.; Calas, G. Experimental and theoretical study of the vibrational properties of diaspore (alpha-AlOOH). *Phys Chem Miner* **2012**, *39* (2), 93-102. DOI: 10.1007/s00269-011-0464-x.

(153) Friedrich, A.; Wilson, D. J.; Haussuhl, E.; Winkler, B.; Morgenroth, W.; Refson, K.; Milman, V. High-pressure properties of diaspore, AlO(OH). *Phys Chem Miner* **2007**, *34* (3), 145-157. DOI: 10.1007/s00269-006-0135-5.

(154) Nakamoto, K.; Margoshes, M.; Rundle, R. E. Stretching Frequencies as a Function of Distances in Hydrogen Bonds. *Journal of the American Chemical Society* **1955**, *77* (24), 6480-6486. DOI: DOI 10.1021/ja01629a013.

(155) Ruan, H. D.; Frost, R. L.; Kloprogge, J. T. Comparison of Raman spectra in characterizing gibbsite, bayerite, diaspore and boehmite. *J Raman Spectrosc* **2001**, *32* (9), 745-750. DOI: DOI 10.1002/jrs.736.

(156) Winkler, B.; Milman, V.; Hennion, B.; Payne, M. C.; Lee, M. H.; Lin, J. S. Ab-Initio Total-Energy Study of Brucite, Diaspore and Hypothetical Hydrous Wadsleyite. *Phys Chem Miner* **1995**, *22* (7), 461-467.

(157) Sassi, M.; Wang, Z. M.; Walter, E. D.; Zhang, X.; Zhang, H. L.; Li, X. H. S.; Tuladhar, A.; Bowden, M.; Wang, H. F.; Clark, S. B.; et al. Surface Hydration and Hydroxyl Configurations of Gibbsite - and Boehmite Nanoplates. *J Phys Chem C* **2020**, *124* (9), 5275-5285. DOI: 10.1021/acs.jpcc.0c00659.

(158) *Crystallography Open Database*. http://www.crystallography.net/cod/ (accessed 2023 10 February).

(159) Comodi, P.; Nazzareni, S.; Zanazzi, P. F.; Speziale, S. High-pressure behavior of gypsum: A single-crystal X-ray study. *American Mineralogist* **2008**, *93* (10), 1530-1537. DOI: 10.2138/am.2008.2917.

(160) Roush, T. L.; Esposito, F.; Rossman, G. R.; Colangeli, L. Estimated optical constants of gypsum in the regions of weak absorptions: Application of scattering theories and comparisons to independent measurements. *J Geophys Res-Planet* **2007**, *112* (E10). DOI: Artn E10003 10.1029/2007je002920.

(161) Haynes, W. M. *CRC handbook of chemistry and physics : a ready-reference book of chemical and physical data*; CRC Press, 2015.

(162) Bergfreund, J.; Siegenthaler, S.; Lutz-Bueno, V.; Bertsch, P.; Fischer, P. Surfactant Adsorption to Different Fluid Interfaces. *Langmuir* **2021**, *37* (22), 6722-6727. DOI: 10.1021/acs.langmuir.1c00668.

(163) Wang, G.; Sun, S. S.; Wu, X. B.; Yang, S. R.; Wu, Y. M.; Zhao, J. X.; Zhang, H.; Chen, W. Intestinal environmental disorders associate with the tissue damages induced by perfluorooctane sulfonate exposure. *Ecotox Environ Safe* **2020**, *197*. DOI: ARTN 110590 10.1016/j.ecoenv.2020.110590.